



# **PHASE BEHAVIOR OF POLYMER–GRAFTED NANOPARTICLES**

A Dissertation

Presented to

The Faculty of the Materials Science and Engineering Program

University of Houston

In Partial Fulfillment

of the Requirements for the Degree

Doctor of Philosophy

in Materials Science and Engineering

by

Katrina Irene Mongcopa

August 2015

# PHASE BEHAVIOR OF POLYMER-GRAFTED NANOPARTICLES

---

Katrina Irene Mongcopa

Approved:

---

Chair of the Committee  
Dr. Ramanan Krishnamoorti,  
Professor, Department of Chemical and  
Biomolecular Engineering

Committee Members:

---

Dr. Megan Robertson,  
Assistant Professor, Department of  
Chemical and Biomolecular Engineering

---

Dr. Jacinta Conrad,  
Assistant Professor, Department of  
Chemical and Biomolecular Engineering

---

Dr. Haleh Ardebili,  
Assistant Professor, Department of  
Mechanical Engineering

---

Dr. Yandi Hu,  
Assistant Professor, Department of Civil  
and Environmental Engineering

---

Dr. Suresh K. Khator,  
Associate Dean,  
Cullen College of Engineering

---

Dr. Dmitri Litvinov,  
Professor and Director, Materials  
Science and Engineering Program

## **Acknowledgements**

I am thankful to my advisor, Dr. Ramanan Krishnamoorti, for helping me grow as a scientist. His support and guidance are very much appreciated. The fulfillment of this work would not be possible without the help of our collaborators, Dr. Rana Ashkar and Dr. Paul Butler who generously shared their expertise in the field. A significant part of this study was also a result of a joint effort with Tyler Martin and Dr. Arthi Jayaraman whose skills certainly added value to our work.

I am indebted to my colleagues, Ryan Poling-Skutvik, Chinedu Umeasiegbu, Daehak Kim and Brian Rohde who tirelessly welcomed scientific discussions and gave valuable advice. I also appreciate the support of Ammar Aboalsaud and our postdocs, Dr. Kun Liang and Dr. Jack Jacob.

I am grateful to Andrew Paterson and his family for all their love and encouragement throughout this journey. I am appreciative of the care and support of my friends in graduate school as well.

Lastly, I dedicate my success to my parents, Fenny and Iñigo, who gave me the greatest gift of a quality education. Their love and support are truly unparalleled.

# **PHASE BEHAVIOR OF POLYMER–GRAFTED NANOPARTICLES**

An Abstract

of a

Dissertation

Presented to

The Faculty of the Materials Science and Engineering Program

University of Houston

In Partial Fulfillment

of the Requirements for the Degree

Doctor of Philosophy

in Materials Science and Engineering

by

Katrina Irene Mongcopa

August 2015

## Abstract

The fundamental thermodynamic interactions between polymer-grafted nanoparticles and their surroundings—whether in a polymer matrix or a solvent—are crucial to the properties and performance of the resulting material. The phase behavior and conformations of the grafted polymer are governed by both entropic and enthalpic effects that in turn, drive dispersion and aggregation in the system. Although the dispersion-aggregation transition in the athermal case is largely entropic in nature, significant enthalpic interactions exist in many chemically dissimilar graft-matrix and graft-solvent systems that influence their phase transition.

In this work, the phase behavior and conformational transitions of polystyrene (PS)-grafted silica nanoparticles in a poly(vinyl methyl ether) (PVME) matrix and cyclohexane are investigated—both systems exhibit conformational changes in the brush as a function of temperature. Through a combination of transmission electron microscopy imaging, small angle x-ray and neutron scattering techniques, a gradual wetting-dewetting transition in the silica-PS/PVME composite is elucidated and found to be distinct from the dispersion-aggregation transition. This is in stark contrast to athermal systems of chemically similar brush and matrix chains where the two transition events are analogous. Moreover, using light and neutron scattering, a coil-to-globule transition of the grafted PS chains in cyclohexane is probed as the solvent quality changes from good to poor. Measurements of the hydrodynamic size reveal a continuous

change from a highly-swollen brush to a globule-like configuration before particle aggregation occurs. These observations are consistent with changes in the brush thickness and radius of gyration measured from neutron scattering experiments.

This work presents key insights into the thermodynamic behavior of polymer-grafted nanoparticles unique to dissimilar graft-matrix and graft-solvent systems. Furthermore, it highlights fundamentally important concepts crucial to the design and functionality of advanced materials.

# Table of Contents

Acknowledgements.....	iv
Abstract.....	vi
Table of Contents.....	viii
List of Figures.....	xi
List of Schemes.....	xiv
List of Tables.....	xv
Chapter 1 Introduction .....	1
Chapter 2 Background.....	6
2.1 The challenge of controlled dispersion: surface modification with polymers .....	6
2.1.1 “Grafting to” strategy .....	6
2.1.2 “Grafting from” strategy .....	9
2.2 Dispersion of grafted nanoparticles in a chemically similar matrix .....	16
2.3 Brush behavior on flat surfaces.....	20
2.4 Brush behavior on curved surfaces.....	23
2.5 Homopolymer blends of polystyrene and poly(vinyl methyl ether) .....	28
Chapter 3 General Experimental Methods.....	31
3.1 Materials .....	31
3.2 Preparation of polymer-grafted SiO <sub>2</sub> nanoparticles .....	32
3.2.1 Synthesis of 1-(Chlorodimethylsilyl)propyl 2-bromoisobutyrate initiator.....	32
3.2.2 Synthesis of 2-bromoisobutyrate functionalized SiO <sub>2</sub> nanoparticles 32	
3.2.3 Synthesis of polymer-grafted SiO <sub>2</sub> nanoparticles by AGET ATRP	33

3.3	Preparation of nanocomposites.....	33
3.4	Fourier transform infrared spectroscopy (FTIR) .....	34
3.5	Size exclusion chromatography (SEC).....	34
3.6	Thermo-gravimetric analysis (TGA) .....	35
3.7	Calculation of polymer grafting density .....	35
3.8	Dynamic light scattering (DLS).....	36
3.9	Small angle x-ray scattering (SAXS) .....	36
3.10	Small angle neutron scattering (SANS).....	37
3.11	Transmission electron microscopy (TEM) .....	38
Chapter 4 Distinct Wetting-Dewetting and Dispersion-Aggregation Transitions in Blends of Polymer-Grafted Nanoparticles and a Chemically Dissimilar Polymer Matrix.....		
4.1	Introduction .....	39
4.2	Methodology.....	41
4.2.1	Synthesis of deuterated polystyrene (SiO <sub>2</sub> -dPS) and hydrogenated polystyrene (SiO <sub>2</sub> -PS) grafted nanoparticles by surface-initiated AGET ATRP.....	41
4.2.2	Preparation of SiO-dPS/PVME and SiO <sub>2</sub> -PS/PVME nanocomposites.....	43
4.2.3	Preparation of nanocomposites for SANS.....	44
4.3	Results and discussion .....	44
4.5	Conclusions.....	59
Chapter 5 Brush Conformations in Nanocomposites of Polymer-Grafted Nanoparticles in a Chemically Distinct Polymer Matrix.....		
5.1	Introduction .....	61

5.2	Methodology.....	64
5.2.1	Synthesis of SiO <sub>2</sub> -dPS nanoparticles by surface-initiated AGET ATRP.....	64
5.2.2	Preparation of SiO <sub>2</sub> -dPS/PVME nanocomposites .....	64
5.3.	Results and discussion .....	64
5.4	Conclusions.....	78
Chapter 6	Coil-to-Globule Transition of Polymer-Grafted Nanoparticles in a Theta Solvent .....	80
6.1	Introduction .....	80
6.2	Methodology.....	82
6.2.1	Synthesis of polystyrene-grafted silica nanoparticles by AGET ATRP.....	82
6.2.2	Preparation of polystyrene-grafted silica nanoparticle suspensions for DLS .....	82
6.2.3	Preparation of polystyrene-grafted silica nanoparticle suspensions for SANS .....	83
6.3	Results and discussion .....	83
6.4	Conclusions.....	101
Chapter 7	Summary and Future Work .....	102
7.1	Summary.....	102
7.2	Future work .....	105
References.....		108

## List of Figures

Figure 2.1	Cyclic synthesis route for polymer-grafted Janus silica nanoparticles using reversible click reaction and grafting to strategies.....	8
Figure 2.2	TEM micrographs of PMMA-AuNPs.....	15
Figure 2.3	Experimental morphology diagram of polymer-tethered particles mixed with matrix polymers.....	16
Figure 2.4	Composite morphology diagram created from all of the available data in the literature.....	17
Figure 2.5	SAXS intensity profile of PBA25k-SiO <sub>2</sub> blended with matched PBA matrix at different silica volume fractions.....	19
Figure 2.6	Illustration of brush dewetting and wetting.....	20
Figure 2.7	Strongly-stretched situation for a grafted layer in a good solvent .....	21
Figure 2.8	The Daoud and Cotton model.....	24
Figure 2.9	Crossover point for a series of nanoparticles with different grafting densities.....	27
Figure 2.10	Phase diagram a PS/PVME blend exhibiting LCST behavior.....	29
Figure 4.1	IR spectra of the hybrid nanoparticle showing signature absorption bands of the different functional groups of the tethered brush.....	45
Figure 4.2	Size exclusion chromatogram of cleaved dPS and PS brush.....	46
Figure 4.3	TGA plots of the SiO <sub>2</sub> -dPS33k hybrid and initiator-grafted nanoparticles.....	46

Figure 4.4	Correlation plots at various angles for the SiO <sub>2</sub> -dPS33k and SiO <sub>2</sub> -PS20k nanoparticles in toluene.....	48
Figure 4.5	SAXS scattering intensity profile of the pure hybrid nanoparticles at room temperature and scattering intensity profile of SiO <sub>2</sub> -dPS33k at higher temperatures.....	50
Figure 4.6	SAXS scattering intensity profiles of SiO <sub>2</sub> -dPS33k/PVME226k and SiO <sub>2</sub> -dPS33k/PVME46k composites relative to the pure hybrid nanoparticle.....	52
Figure 4.7	Temperature dependence of SAXS scattering intensity data for SiO <sub>2</sub> -dPS33k/PVME226k and SiO <sub>2</sub> -PS20k/PVME226k blends.....	53
Figure 4.8	Temperature dependence of the coherent SANS intensity data.....	55
Figure 4.9	Zero-angle scattering and correlation length as a function of temperature.....	57
Figure 4.10	Graft monomer and matrix monomer concentration versus distance from the particle surface.....	58
Figure 5.1	Small angle x-ray scattering profile of the.....	66
Figure 5.2	TEM images of SiO <sub>2</sub> -dPS33k/PVME226k.....	69
Figure 5.3	Change in SAXS inter-particle distance with temperature.....	70
Figure 5.4	SANS P(q) after division of the coherent SANS I(q) by the Percus-Yevick model.....	72
Figure 5.5	SANS P(q) fit to the onion exponential shell and polymer excluded	

volume models at representative temperatures.....	74
Figure 5.6 Resulting trends from the onion exponential shell and polymer excluded volume model fits.....	77
Figure 6.1 Correlation plots for SiO <sub>2</sub> -PS67k in toluene and cyclohexane.....	85
Figure 6.2 Correlation plot at select temperatures.....	86
Figure 6.3 Temperature dependence of the hydrodynamic radius.....	87
Figure 6.4 Temperature dependence of the SANS scattering intensity .....	90
Figure 6.5 Fits to a core shell model at select temperatures .....	91
Figure 6.6 Fits to a fuzzy sphere model at select temperatures .....	92
Figure 6.7 Fits to a core-shell Lorentz model in toluene.....	92
Figure 6.8 Fits to a core-shell Lorentz model in cyclohexane.....	93
Figure 6.9 Change in shell thickness with temperature and corresponding change in SLD.....	95
Figure 6.10 Fits to a core-shell Lorentz model for SiO <sub>2</sub> -PS67k at select temperatures.....	95
Figure 6.11 Fits to a core-shell Lorentz model for SiO <sub>2</sub> -PS43k at select temperatures.....	96
Figure 6.12 $1/I_{\text{SANS, Coh}}(q)$ vs. $q^2$ at high temperatures and low temperatures...	98
Figure 6.13 $1/I_{\text{SANS, Coh}}(0)$ as a function of temperature.....	99
Figure 6.14 Change in $R_g$ with temperature.....	101

## List of Schemes

Scheme 2.1 Reaction of H <sub>2</sub> N–PEO with the surface hydroxyl group of silica nanoparticles.....	6
Scheme 2.2 Modification of silica nanoparticle and click reaction.....	8
Scheme 2.3 Dynamic equilibrium between dormant and active species.....	9
Scheme 2.4 General mechanism for RAFT polymerization.....	11
Scheme 2.5 Synthesis of BDB–anchored silica nanoparticles.....	12
Scheme 2.6 General mechanism of ATRP.....	13
Scheme 2.7 Synthesis of polymer-coated AuNP by surface-initiated living radical polymerization.....	14
Scheme 4.1 General synthesis scheme for the preparation of initiator functionalized and deuterated/hydrogenated polystyrene-grafted SiO <sub>2</sub> nanoparticles.....	43

## List of Tables

Table 3.1	Neutron and x-ray SLD values of relevant compounds.....	37
Table 4.1	Characteristics of hybrid nanoparticles under study.....	48
Table 4.2	Characteristics of hybrid nanoparticles from SAXS measurements .....	49
Table 5.1	Best fit parameters using the onion exponential shell model.....	75
Table 5.2	Best fit parameters using the polymer excluded volume model....	75
Table 6.1	Characteristics of the synthesized hybrid nanoparticles.....	84
Table 6.2	Hydrodynamic radius of SiO <sub>2</sub> -PS67k in good solvents.....	86

# Chapter 1 Introduction

The remarkable effects of blending fillers with polymers were realized over a century ago when for instance, carbon black, zinc oxide, and/or magnesium sulfate particles were incorporated in vulcanized rubber to toughen automobile tires<sup>1</sup>. In the early 1900s, Bakelite was discovered as a result of trying to strengthen wood through impregnation with synthetic resin<sup>2,3</sup>. These innovations led to the development of a new class of materials and more importantly, inspired a surge of curiosity for what polymer composites have yet to offer.

Polymer composites consist of two main components: a polymeric matrix and additives typically in the micron or nanometer length scales. The combination of matrix polymer chemistry, filler type and matrix-filler interaction dictates the resulting properties of the material and thus, its appropriate applications. In the biomedical field, nanocomposites are used for bone repair and implantation. One example is a hydroxyapatite (HAP)-polymer nanocomposite. HAP is the major inorganic component found in hard tissue and is typically used in orthopedic surgery<sup>4</sup>. By itself, HAP is difficult to shape due to its brittleness and rigidity. Apart from migrating from implanted sites, they also tend to aggregate, making dispersion very difficult. Incorporating HAP nanoparticles in a biodegradable polymer matrix such as chitosan, for instance, is thus ideal in making flexible scaffolds that promote site-specific bone formation as shown by previous work<sup>5</sup>.

The use of nanocomposite materials is also pervasive in the area of electronics. Organic polymer-based photodiodes, for instance, typically employ a second component such as fullerene to facilitate charge separation<sup>6</sup>. It has been found, however, that a more efficient charge separation can be achieved when polymers are combined with and chemically bound to inorganic semiconductor nanocomposites (typically cadmium or lead chalcogenides). In this manner, charge transfer is greatly enhanced due to the amplified percentage of generated excitons that dissociate at the interface, characteristic of high-performing devices<sup>7,8</sup>.

In aerospace engineering, carbon fiber reinforced composites (CFRC) are the key, indispensable materials that compose about 50% of an aircraft's total structural mass<sup>9</sup>. Owing to the properties of carbon fibers such as low weight, high tensile strength, stiffness and chemical resistance, CFRC quickly gained attention and replaced regular aluminum and titanium alloys as primary structures in aircrafts<sup>9,10</sup>. Additionally, CFRC is favored over glass-reinforced polymers in manufacturing body panels for cars, for instance, making them more cost-effective to produce and contributing to the overall better performance of the vehicle.

A critical component that determines the properties of composites for their desired application is the dispersibility or controlled distribution of the fillers in the continuous matrix. Over the years, research efforts that focus on circumventing the issue of controlled dispersion have found that modifying the surface of inorganic fillers—whether rods<sup>11,12</sup>, sheets<sup>13</sup> or spheres<sup>14</sup>—with polymers

improves their compatibility with the polymer matrix, thus facilitating their distribution in the material. It has therefore become necessary to look into the underlying interactions between the polymer-grafted particles and the polymer matrix, fundamentally from a thermodynamic perspective.

The free energy of mixing  $\Delta G_m$  for binary polymer blends is largely governed by the Flory-Huggins equation<sup>15</sup> given by

$$\frac{\Delta G_m}{k_B T} = \frac{\varphi_1}{N_1} \ln \varphi_1 + \frac{\varphi_2}{N_2} \ln \varphi_2 + \chi \varphi_1 \varphi_2, \quad \text{Equation 1.1}$$

where  $k_B$  is the Boltzmann constant,  $T$  the temperature,  $\varphi_{1/2}$  the volume fraction of polymers 1 and 2,  $N_{1/2}$  is the degree of polymerization and  $\chi$  is the interaction parameter. The first two terms in equation (1) account for the entropic contributions to  $\Delta G_m$ , while the last term relates to enthalpic contributions. The larger the molecular weight of polymers used, the lower the entropic contributions become as the chains assume fewer configurational states. The mixing of the polymer blend, in such case, would then be primarily dictated by the enthalpic term or the value of  $\chi$ <sup>16</sup>. A small entropic contribution, however, is still considered for the temperature dependence of  $\chi$  written as

$$\chi = a + \frac{b}{T}, \quad \text{Equation 1.2}$$

where  $a$  and  $b$  represent the entropic and enthalpic contributions, respectively. Positive values for  $\chi$  are typically found for phase behaviors exhibiting an upper

critical solution temperature, while negative values pertain to those with a lower critical solution temperature<sup>17</sup>.

A substantial amount of literature has looked closely into the blend miscibility of athermal systems ( $\chi \approx 0$ ) of polymer-grafted nanoparticles dispersed in a chemically similar polymer matrix. These studies have thus provided a solid basis and direction for understanding systems involving polymer-grafted nanoparticles in a chemically *distinct* matrix or where  $\chi \neq 0$ , as presented in this dissertation. In particular, this work focuses on the case where spherical silica ( $\text{SiO}_2$ ) nanoparticles are grafted with polystyrene (PS) and dispersed in poly(vinyl methyl ether) (PVME). PS is an abundant, inexpensive resin and is a widely used plastic. It is solid at room temperature, but can easily flow and be molded beyond its glass transition temperature ( $\sim 90$  °C). PVME, on the other hand, is a water-soluble and viscous liquid which has found application in the rubber and adhesive industries. More importantly, PS/PVME systems are known to exhibit a lower critical solution temperature (LCST) behavior—they exhibit complete miscibility at low temperatures ( $\chi < 0$ ) and phase separate at high temperatures ( $\chi > 0$ ).

Similarly, as in polymer blends, polymer-grafted nanoparticles in a solvent can have a characteristic phase separation behavior. Depending on the solvent quality and how it changes with temperature, polymers can undergo conformational transitions in response to favorable and unfavorable interactions with the surrounding solvent molecules. Such thermoresponsive polymers<sup>18</sup> have

emerged as a new class of materials for drug and gene delivery<sup>19,20</sup>, among many others. Understanding how enthalpic and entropic driving forces affect the changes in brush behavior would thus have important implications in tuning the unique properties of such system for specific applications. Thus, in addition to polymer blends, we also investigate the phase behavior of SiO<sub>2</sub>-PS nanoparticles in a cyclohexane  $\theta$ -solvent. This system exhibits an upper critical solution temperature behavior (UCST), whereby PS-grafted nanoparticles are completely soluble at high temperatures and become insoluble at low temperatures.

Our investigation of the phase behavior and transitions undergone by SiO<sub>2</sub>-PS nanoparticles in an LCST and UCST environment is an attempt to elucidate the underlying thermodynamic interactions that govern polymer blends and solutions, particularly for the dissimilar graft-matrix and graft-solvent case. In Chapter 4, a gradual wetting-dewetting transition of the silica-PS/PVME composite is shown to be distinct from the dispersion-aggregation transition consistent with simulation results. We further support this observation with measurements of the grafted brush characteristics during the transition as discussed in Chapter 5. Lastly, in Chapter 6, we probe a coil-to-globule evolution in the brush as solvent conditions change from good to poor—a behavior analogous to brush wetting and dewetting. The implications of these findings and direction for future research are summarized in Chapter 7. Throughout this work, we heavily rely on light, small angle x-ray and neutron scattering techniques to understand the behavior and conformational changes in our systems.

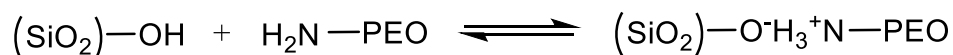
## Chapter 2 Background

### 2.1 The challenge of controlled dispersion: surface modification with polymers

Among the various types of fillers used to prepare polymer composites, spherical nanoparticles (0-D) are often the most commonly used due to their large surface area and less energy interaction per pair of nanoparticles relative to nanorods (1-D) and nanosheets (2-D) which, in turn, lessens the complexity of their dispersion in a matrix<sup>21</sup>. Because these inorganic particles are inherently incompatible with organic polymer matrices, their surfaces are functionalized with polymers that then facilitate their spatial distribution.

#### 2.1.1 “Grafting to” strategy

Some strategies for the surface modification of nanoparticles take advantage of ionic interactions. Fernandes et al.<sup>22</sup> prepared ionic hybrids consisting of amine-terminated poly(ethylene oxide) (PEO) and SiO<sub>2</sub> nanoparticles. This technique exploits the favorable interaction between the cationic amine group of PEO and anionic hydroxyl groups on the surface of SiO<sub>2</sub> as shown in the following equilibrium reaction scheme,

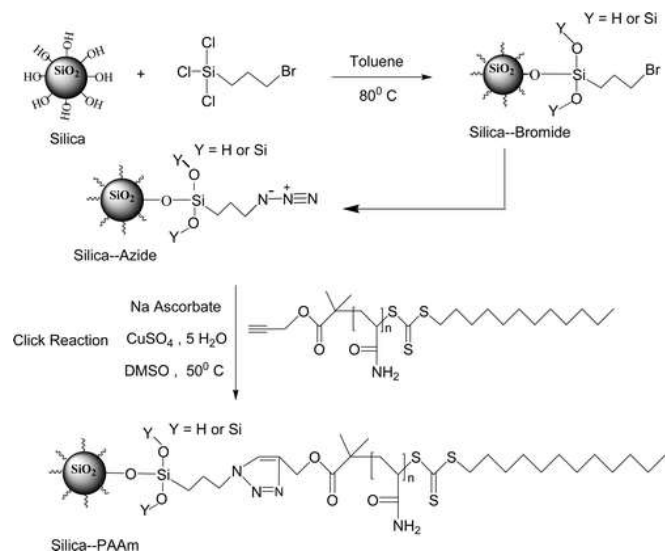


Scheme 2.1 Reaction of H<sub>2</sub>N-PEO with the surface hydroxyl group of silica nanoparticles

They showed through transmission electron microscopy (TEM) and SAXS that unlike systems with similar components but no ionic interactions, a high degree of order and good dispersion can be achieved both in thin film and bulk forms.

A more commonly used approach to modify the surface of nanoparticles is through covalent functionalization. In the case where long chain functional polymers are attached or “grafted to” the surface, techniques such as “click” chemistry can be employed. In fact, recent approaches used this technique in combination with a living radical polymerization process such as reversible addition fragmentation chain transfer (RAFT) for surface modification. Ranjan and Brittain<sup>23</sup> prepared an alkyne-terminated RAFT chain transfer agent (CTA) which was used to grow a chain of polyacrylamide, effectively producing a macro-CTA. The alkyne terminal group of this chain readily participated in a 1,3-dipolar cycloaddition (click reaction) with the azide-modified silica nanoparticles according to Scheme 2.2. This afforded particles that are well within the brush regime and have a relatively high grafting density of 0.31 chain/nm<sup>2</sup>.

Li et al.<sup>24</sup> used a similar strategy to prepare polymer-grafted Janus or asymmetric nanoparticles that can be used as multistep catalysts and drug carriers, to name a few. Using reversible “grafting to” and click reactions, alkyne-functionalized 15 nm silica nanoparticles were immobilized onto 500 nm nanoparticles bearing an azido functional group, effectively allowing the smaller nanoparticles to have both exposed and blocked phases (Figure 2.1).



Scheme 2.2 Modification of silica nanoparticle and click reaction.<sup>23</sup>

The exposed alkyne groups on one face thus became amenable to another click reaction with azido-capped polymers. By using mechanical forces such as ultrasonication, the partially masked 15 nm particles were successfully unclicked and cleaved from the surface to isolate the azido-functionalized 500 nm particles that can be used in another cycle.

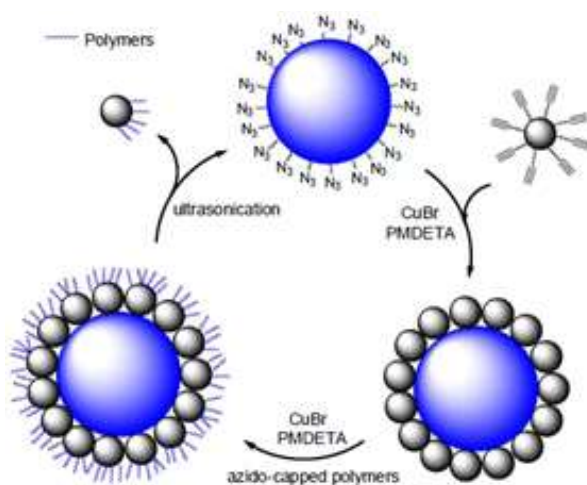


Figure 2.1 Cyclic synthesis route for polymer-grafted Janus silica nanoparticles using reversible click reaction and grafting to strategies.<sup>24</sup>

While the aforementioned “grafting to” strategies are versatile and fairly simple to carry out, they typically suffer from low grafting densities due to crowding or steric hindrance on the substrate, which in turn limit their applications. To overcome this, “grafting from” techniques demonstrated through controlled living radical polymerization (CLRP) are employed.

### 2.1.2 “Grafting from” strategy

CLRP is a robust strategy for preparing polymers of well-defined molecular weight, composition and architecture. It differs from conventional radical polymerization in that the radicals generated through the decomposition of an initiator in a conventional process undergo propagation and termination in a matter of seconds. In CLRP, on the other hand, the lifetime of a growing radical extends for hours.<sup>25</sup> This is due to the rapid exchange between dormant and active species in dynamic equilibrium as illustrated below.



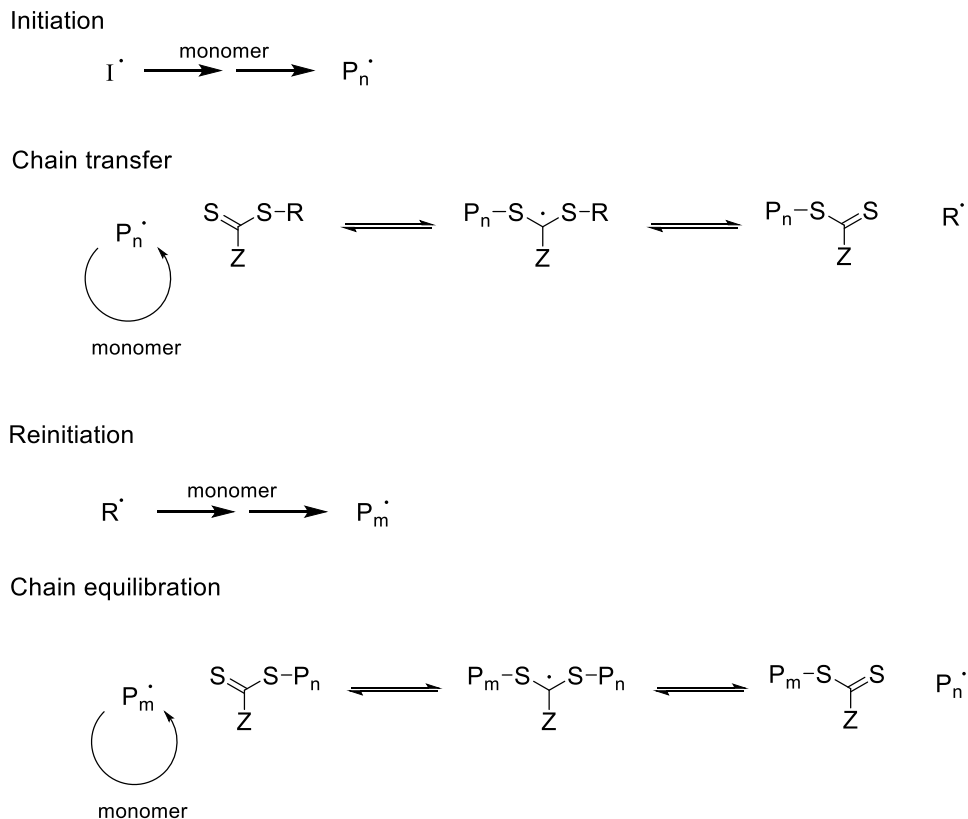
Scheme 2.3 Dynamic equilibrium between dormant and active species.

PX is the dormant species and X is a group (atom or molecular fragment) capable of leaving and reattaching to the radical rapidly. When PX spontaneously dissociates into the active radical and inert group X, it may undergo propagation steps by adding on a monomer or just recombine with X so that no net reaction takes place. In the case where the radical spends most of its time in the dormant state, termination reactions are unlikely to occur. This scenario is advantageous as over time, the radical species are equally likely to propagate, allowing for a

more controlled growth of the polymer with low polydispersities<sup>26</sup>. Various types of CLRP techniques have emerged over the years, a few of which are discussed below.

RAFT polymerization is essentially a free radical polymerization process involving a reversible chain transfer of a dithioester ( $S=C(Z)S-R$ ) moiety between active and dormant chains to sustain the livingness of the polymerization reaction. As shown in Scheme 2.4, the  $S=C(Z)S-R$  species initially reacts with a propagating radical ( $P_n\bullet$ ) and liberates a radical ( $R\bullet$ ). The free  $R\bullet$  then reacts with a monomer to generate a new propagating radical ( $P_m\bullet$ ) in a reinitiation step which then undergoes the same process of chain extension in equilibrium<sup>27,28</sup>.

The adaptability of the RAFT process to a wide range of monomer types has made it useful in preparing grafted polymers on surfaces. Baum and Brittain<sup>29</sup> grew styrene, methyl methacrylate, and *N,N*-dimethylacrylamide brushes from silicate surfaces (silicon wafers) functionalized with azo initiators. A small amount of “free” or untethered initiator (2,2'-Azobisisobutyronitrile, AIBN) in the polymerization solution yielded unattached polymer from which they estimated the molecular weight of the grafted brush as well as its polydispersity.

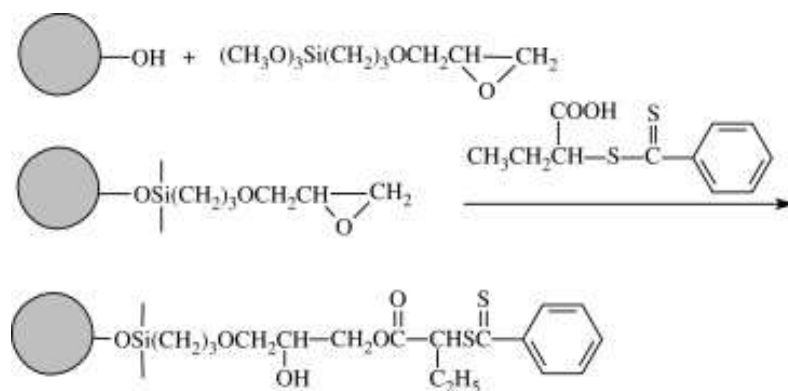


Scheme 2.4 General mechanism for RAFT polymerization.

Moreover, they note that small amounts of untethered AIBN helped eliminate impurities that can terminate initiating sites and lead to low grafting densities. They determined a direct relationship between the brush thickness (through ellipsometry) and sequential monomer addition, thus confirming the controlled behavior of the RAFT polymerization.

The same technique was applied by Liu and Pan<sup>30</sup> in preparing PS-grafted silica nanoparticles. A 2-Butyric acid dithiobenzoate (BDB) CTA was initially immobilized on the silica nanoparticle surface through a ring-opening polymerization reaction with 3-Glycidyloxypropyltrimethoxysilane as illustrated in Scheme 2.5. Fourier-transform infrared (FTIR) spectroscopy, transmission

electron microscopy (TEM) and thermogravimetric analysis (TGA) confirmed the successful attachment of polystyrene on the silica nanoparticle surface with a narrow polydispersity of 1.10.

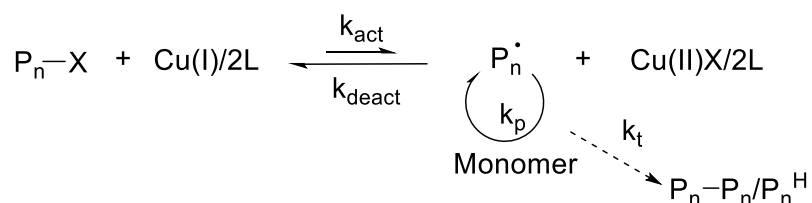


Scheme 2.5 Synthesis of BDB-anchored silica nanoparticles.<sup>30</sup>

The RAFT technique has been shown to be adaptable in a large range of solvents, monomers and reaction temperatures. As with any polymerization technique, however, it is not without its disadvantages. This method primarily entails the use of a RAFT agent or CTA, which thus necessitates a multistep synthetic procedure. Such compounds are also inherently colored (due to the dithiocarbonyl group), pungent and can be unstable overtime. These drawbacks are circumvented in another commonly used CLRP technique—the atom transfer radical polymerization (ATRP) method.

ATRP involves a halogen atom transfer between a copper (I) complex,  $\text{CuX}/2\text{L}$  (where  $\text{X} = \text{Cl}$  or  $\text{Br}$  and  $\text{L} = 2,2'$ -bipyridine or a  $4,4'$ -disubstituted- $2,2'$ -bipyridine) and added initiator or dormant propagating chain end in a dynamic equilibrium (Scheme 2.6)<sup>31</sup>. The transition metal catalyst in its lower oxidation

state is complexed with an appropriate ligand and reacts reversibly with the initiator molecule to transfer its labile atom, thus generating an oxidized transition metal halide complex,  $\text{Cu(II)X/2L}$ , and a radical  $\text{P}_n^\bullet$ . This radical propagates and adds a monomer, but is also rapidly deactivated by its reaction with the oxidized transition metal halide complex. This step regenerates the lower oxidation state transition metal catalyst and an oligomeric X-terminated dormant chain,  $\text{P}_n\text{-X}$ .

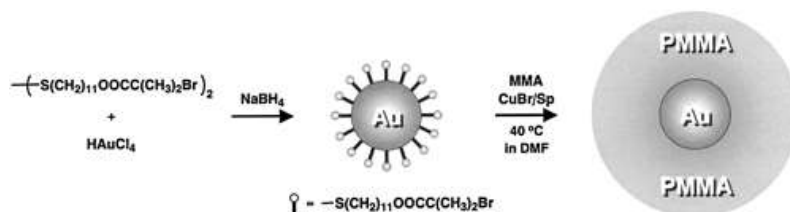


Scheme 2.6 General mechanism of ATRP.

Termination reactions ( $k_t$ ) are unavoidable in living polymerization reactions. At the beginning of the reaction, the concentration of radicals in solution is large such that the rate at which dormant species are formed is much slower than the rate at which termination reactions occur. As termination proceeds, however, the concentration of  $\text{Cu(II)X}$  increases, and since the product  $[\text{Cu(II)X}][\text{P}_n^\bullet]$  is constant, the concentration of radicals decreases. In other words, once the concentration of  $\text{Cu(II)X}$  is sufficiently high, radicals terminate at a much slower rate, allowing for a controlled/"living" polymerization to take place. This process is termed the "persistent radical effect"<sup>32,33</sup>.

Over the years, various architectures such as linear, star, comb/brush, network/crosslinked and dendritic/hyperbranched polymers have been generated using the ATRP technique. Not surprisingly, this method has been used to

prepare different nanostructured materials<sup>34,35</sup>, of particular interest are functionalized spherical particles. Ohno et al.<sup>36</sup> prepared gold nanoparticles (AuNPs) grafted with well-defined poly(methyl methacrylate) (PMMA) of grafting density 0.3 chain/nm<sup>2</sup>. This was performed through a one-pot reduction of tetrachloroaurate (HAuCl<sub>4</sub>) with sodium borohydrate (NaBH<sub>4</sub>) in the presence of an initiator-carrying disulfide. This was then followed by the surface-initiated living radical polymerization of MMA using a copper catalyst and dimethylformamide (DMF) as solvent (Scheme 2.7).



Scheme 2.7 Synthesis of polymer-coated AuNP by surface-initiated living radical polymerization.<sup>34</sup>

Similar to the work done by Baum and Brittain mentioned above, a “free” initiator was added to allow the polymerization to proceed in a controlled fashion. TEM measurements on these highly-grafted PMMA-AuNPs revealed that the AuNPs are uniformly dispersed and that the average inter-particle distance increases with increasing molecular weight or chain length of the grafted polymer (Figure 2.2).

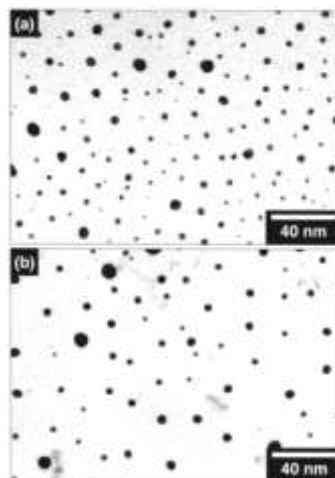


Figure 2.2 TEM micrographs of PMMA-AuNPs with molecular weight of grafted polymers (a) 15,000 g/mol and (b) 25,000 g/mol.<sup>34</sup>

In two separate accounts, von Werne and Patten<sup>37,38</sup> prepared structurally well-defined polymer-grafted silica nanoparticles using ATRP and provided an understanding of the differences in controlling the polymerization of styrene and MMA from the same particle. They found that good molecular weight control can be achieved for polymerizations of styrene on 75 nm silica nanoparticles; while the same result can be obtained for MMA only in the presence of small amounts of free initiator in solution. They argued that the difference lies in the manner in which the PRE or termination mechanism occurs in each system. More specifically, styrene undergoes self-initiation while MMA does not. Because freely diffusing chains terminate faster than bound chains, a high concentration of deactivator (Cu(II)X species) is achieved more quickly in the case of styrene polymerization, which in turn deactivates radicals faster than the rate at which termination events occur<sup>38</sup>.

## 2.2 Dispersion of grafted nanoparticles in a chemically similar matrix

It was previously mentioned that a good strategy for improving the dispersion of nanoparticles in a polymer matrix is to make the inorganic filler more compatible with the continuous phase. Thus, a natural starting point for evaluating the dispersion of polymer-grafted nanoparticles would be to have a polymer matrix that is chemically similar to the grafted brush. Such is a simple case of an athermal system where  $\chi=0$ .

The self-assembly of PS-grafted silica nanoparticles in a PS matrix was extensively investigated through a combination of simulations, theory and experiments<sup>39,40</sup>. By varying the number of grafted chains and grafted chain lengths, complementary mean-field theory and Monte Carlo simulations revealed different packing configurations adopted by the nanoparticles as they balance core-core attractions and brush elasticity (Figure 2.3a).

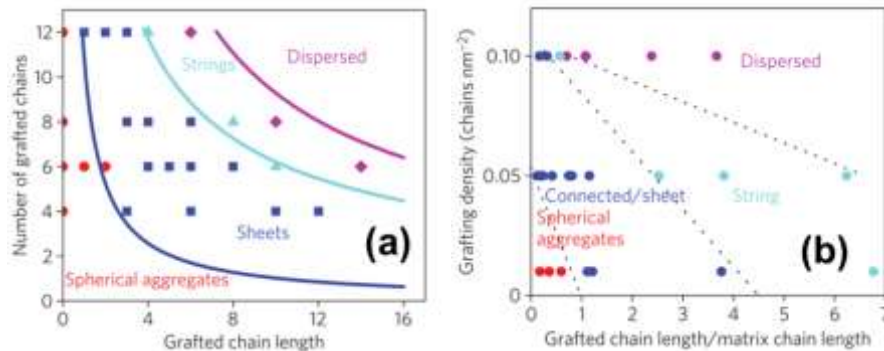


Figure 2.3 (a) Results of simulations and theory at different grafting densities. (b) Experimental 'morphology diagram' of polymer-tethered particles mixed with matrix polymers.<sup>39</sup>

The composite morphology diagram elucidated structures from spherical aggregates at low grafting densities, to sheets, strings and well–dispersed nanoparticles at high grafting densities. These structural formations were confirmed by experiments which took into account the grafted chain length to matrix chain length ratio (Figure 2.3b). Such investigations explicitly suggest that the dispersion of polymer–grafted nanoparticles in a chemically similar matrix can be controlled by tuning the grafting density ( $\sigma$ ) and grafted chain/matrix chain ratio ( $\alpha$ ).

Kumar and co–workers<sup>40</sup> generated a composite morphology diagram for all of the available data in literature on grafted nanoparticles which seems to imply a “universal” trend in the behavior of this type of system (Figure 2.4).

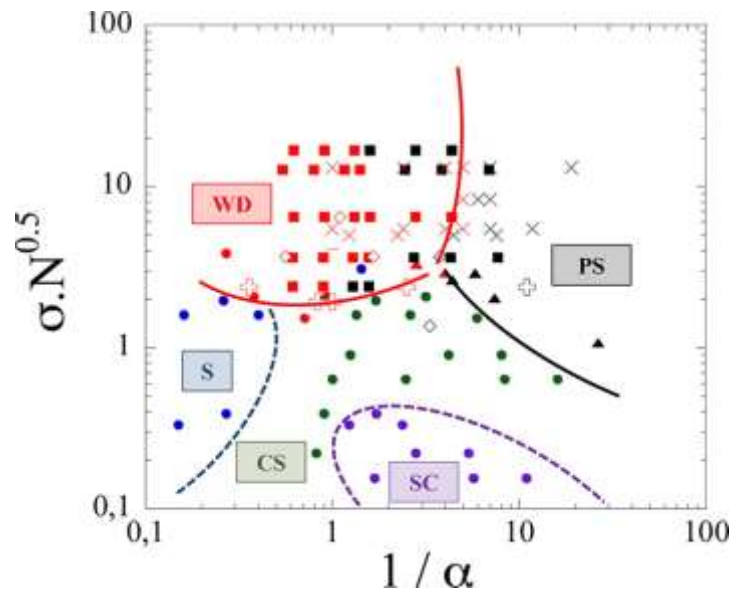


Figure 2.4 Composite morphology diagram where the points correspond to well–dispersed particles (WD); phase separated samples (PS); strings (S); connected sheets (CS); and small clusters (SC).<sup>40</sup>

Of particular interest is the region delineated by high grafting densities,  $\sigma N^{0.5} > 2$ , where  $N$  refers to the degree of polymerization of the brush, and high  $\alpha$  (i.e., grafted chain length > matrix chain length). In this regime, the nanoparticles are expected to be well-dispersed in the matrix (Figure 2.4). Within the same grafting density region, however, as  $\alpha$  becomes smaller (i.e. molecular weight of the matrix chain becomes larger), entropic demixing occurs and a phase-separated state is attained. As a specific example, previous work from our group<sup>41</sup> showed that at a high  $\sigma$  of 0.8 chain/nm<sup>2</sup>, when free chains of poly(butyl acrylate) (PBA) were mixed with tethered PBA brushes of similar molecular weight ( $\alpha=1$ ), brush swelling and dispersion of the nanoparticles occurred. This was evidenced by an increase in brush height with silica content, determined through SAXS (Figure 2.5a and b). On the other hand, when the matrix molecular weight was at least three times larger than that of the grafted brush, a decrease in brush height was observed, indicative of brush collapse and aggregation (Figure 2.5b and c). The same behavior was predicted by theory and simulations<sup>42,43</sup>. As mentioned previously, polymer-grafted nanoparticles in a chemically similar matrix is an athermal system with an interaction parameter  $\chi=0$ . Thus, dispersion/aggregation is a consequence of brush wetting/dewetting and is largely controlled by entropic forces. This means that a gain in mixing entropy favors brush wetting and leads to a thermodynamically miscible system. On the other hand, loss in conformational entropy from matrix penetration drives dewetting and immiscibility in the system<sup>42,44</sup>.

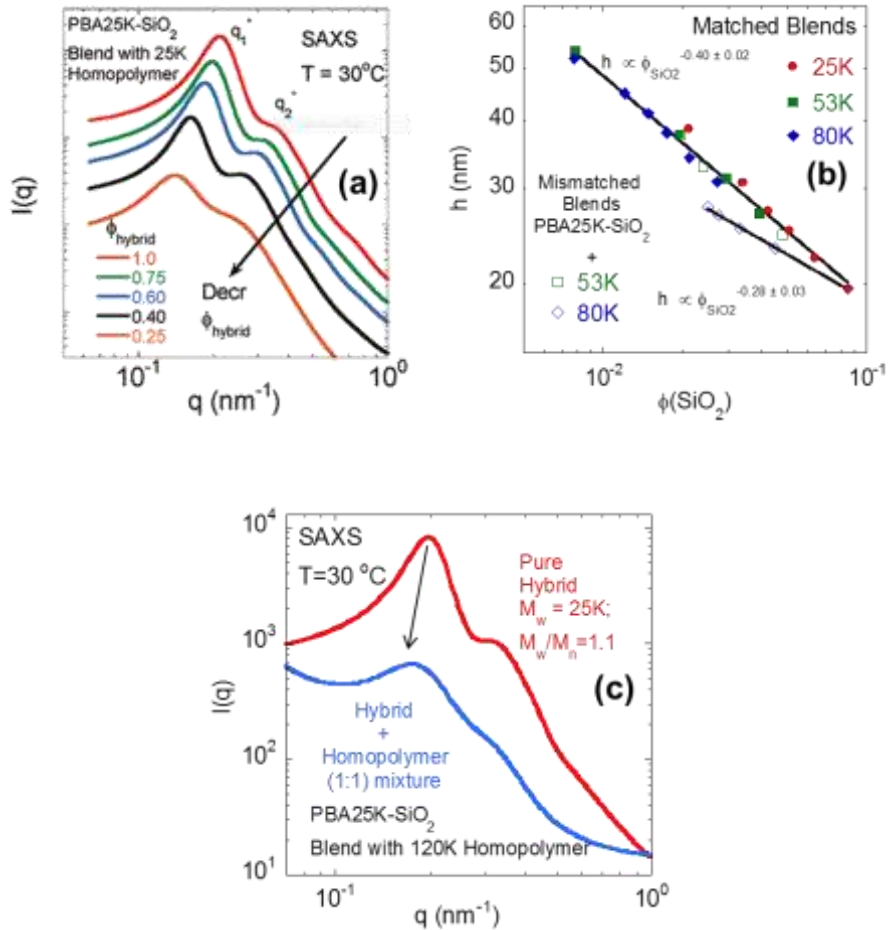


Figure 2.5 (a) SAXS intensity profile of PBA25k-SiO<sub>2</sub> blended with matched PBA matrix; (b) brush height vs. silica content; (c) SAXS intensity profile of pure hybrid and blend of hybrid with mismatched matrix.<sup>41</sup>

In other words, long enough matrix chains relative to the brush are entropically expelled from the grafted corona, causing the brushes to collapse and consequently aggregate. In contrast, short matrix chains are able to partially penetrate the brush, favoring the dispersion of the nanoparticles (Figure 2.6).

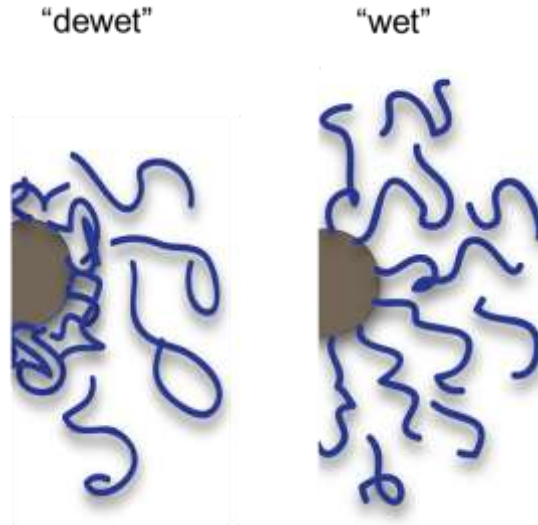


Figure 2.6 Illustration of brush dewetting and wetting.

### 2.3 Brush behavior on flat surfaces

An important aspect in controlling the dispersion of grafted nanoparticles in a polymer matrix is the brush behavior as it interacts with the free chains. Key insights to this are scaling laws provided by Alexander<sup>45</sup> and de Gennes<sup>46</sup> in looking at the structure of isolated brushes. Their analysis is restricted to the athermal case ( $\chi = 0$ ) and the situation where the free chains are comparable to (or smaller than) that of the tethered brush. At high enough grafting density  $\sigma$  and in a good solvent, the attached chains are depicted as overlapping chains that repel each other with energy of order  $kT$ , forcing them to stretch into an array of correlation blobs of linear size  $D$  (Figure 2.7).

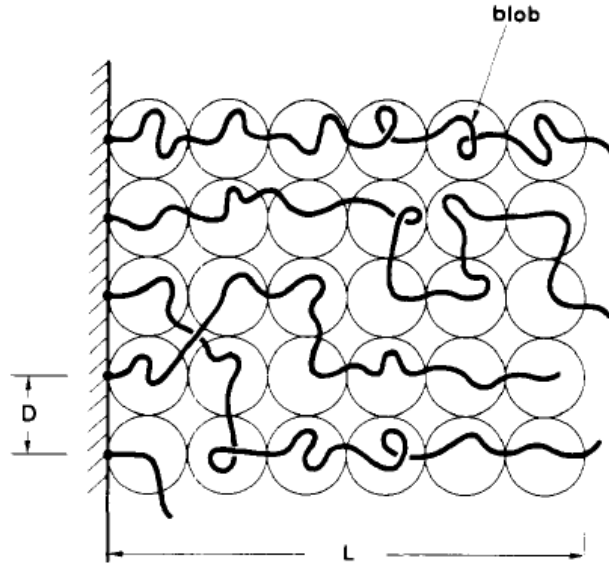


Figure 2.7 Strongly-stretched situation for a grafted layer in a good solvent. The chains are mainly stretched normal to the wall.<sup>47</sup>

The correlation length,  $\xi$ , which is the distance between chains is defined by the distance between the grafting points according to the relation,

$$\xi \approx \frac{1}{\sqrt{\sigma}}. \quad \text{Equation 2.1}$$

The height of the brush  $L$  is given by the size of a correlation blob multiplied by the number of these blobs per chain,

$$L \approx \xi \frac{N}{g} \approx N \sigma^{(1-\nu)/(2\nu)} b^{1/\nu}, \quad \text{Equation 2.2}$$

where  $N$  and  $g$  are the number of monomers per chain and number of monomers per correlation blob, respectively;  $\nu$  is a scaling exponent and  $b$  is the effective bond length or Kuhn length. At a constant grafting density, the height is directly proportional to  $N^{48,49}$ .

de Gennes also looked at the case of a polymer melt where the grafted chains (N chains) are in contact with a pure polymeric liquid (P chains) and defined two volume fractions,  $\varphi_N$  and  $\varphi_P$ . In the low  $\sigma$  limit ( $\sigma < N^{-1}$ ), the N chains do not overlap and have  $\varphi_N < N^{-1/2}$ , which is always small. In this situation, the tethered chains remain unstretched and behave like a dry brush as long as  $\varphi_P$  dominates over  $\varphi_N$ <sup>46,50</sup>. As  $\sigma$  is increased beyond  $\sigma \cong N^{-1}$ , the grafted chains start to overlap and enter the stretched wet brush regime.

The free energy of mixing per tethered chain is derived from two physical contributions. First is a contribution due to the entropy of mixing between P chains and N chains which causes the brush to swell. Second is an elastic term which restricts it. The free energy per grafted chain,  $F_{mix}$ , is thus expressed as

$$\frac{F_{Mix}}{kT} = \frac{LD^2}{a^3} \frac{1}{P} \varphi_P \ln \varphi_P, \quad \text{Equation 2.3}$$

where  $LD^2$  is the volume per grafted chain and hence the term  $LD^2/a^3$  refers to the corresponding number of lattice sites. An expression for the elastic energy is given by

$$\frac{F_{el}}{kT} = \frac{3}{2} \left( \frac{L^2}{R_0^2} + \frac{R_0^2}{L^2} \right), \quad \text{Equation 2.4}$$

where  $R_0$  is the thickness of the grafted layer. In minimizing  $F_{mix} + F_{el}$  with the constraint

$$\varphi_N = 1 - \varphi_P, \quad \text{Equation 2.5}$$

the resulting expression in terms of  $\varphi_N$  becomes

$$kP\sigma^2 \left[ 1 - \left( \frac{\varphi_N^2}{N\sigma^2} \right)^2 \right] = \varphi_N \ln(1 - \varphi_N) + \varphi_N^2, \quad \text{Equation 2.6}$$

where  $k$  is a coefficient of order unity. According to de Gennes, three regimes then become apparent given this relationship: 1.) when  $\sigma < \sigma_1$  where  $\sigma_1 = PN^{-3/2}$ , grafted chains are expected to be unstretched; 2.) when  $\sigma_1 < \sigma < \sigma_2$  where  $\sigma_2 = P^{-1/2}$ ,  $L \gg R_0$ , the brushes are stretched; 3.) when  $\sigma > \sigma_2$  and as  $\sigma \rightarrow 1$ , the concentration of  $N$  and  $P$  chains become comparable and the  $N$  chains become fully stretched, segregating themselves from the melt<sup>46,51</sup>.

## 2.4 Brush behavior on curved surfaces

Daoud and Cotton<sup>52</sup> extended the pioneering work of Alexander and de Gennes to the case where the grafted chains are tethered to a central point (Figure 2.8), aptly called “star polymers”<sup>53</sup>. Given such conformation, variations in local concentration arise—the inner region is considered to be highly concentrated but as the chain moves out from the center, the concentration decreases and individual chains are farther apart.

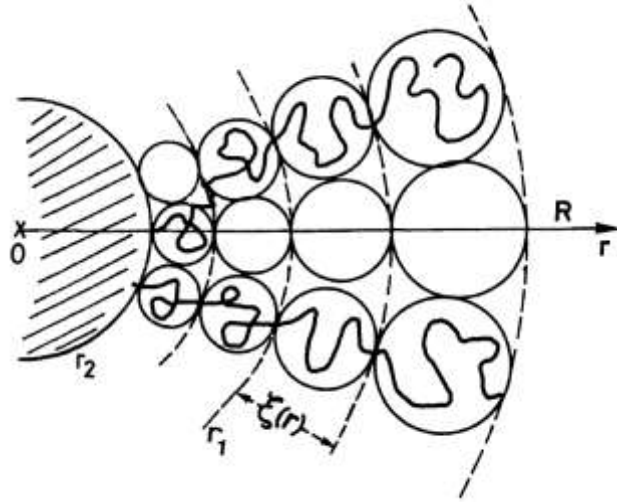


Figure 2.8 The Daoud and Cotton model which depicts each branch as a succession of blobs of size  $\xi$  surfacing from the center of the star.<sup>52</sup>

This model further considers blobs of size  $\xi$  which increases from the center to the periphery and defines a local swelling parameter  $\alpha(r)$  at a distance  $r$  as

$$\alpha(r) \equiv \frac{\xi(r)}{\xi_0(r)}, \quad \text{Equation 2.7}$$

where  $\xi_0$  is the unperturbed size for an ideal chain and is given by

$$\xi_0(r) \sim n^{\frac{1}{2}}(r)l, \quad \text{Equation 2.8}$$

where  $n(r)$  is the number of statistical units in the blob at distance  $r$ . This model defines two distinct regions: an outer region of more expanded blobs and an inner region of concentrated blobs. It supposes that in a good solvent and at large distances from the core, the chains are swollen such that

$$\alpha^5 \sim \nu n^{1/2}(r), \quad \text{Equation 2.9}$$

where  $\nu = \frac{1}{2} - \chi$  refers to the excluded volume parameter. The dimensionless concentration inside a blob is given by

$$\varphi(r) = \frac{n(r)l^3}{\xi^3(r)} \quad \text{and} \quad \text{Equation 2.10}$$

$$\sim n^{-1/2} \alpha^{-3}. \quad \text{Equation 2.11}$$

The following relationships are then derived from equations 2.8, 2.9 and 2.11

$$\xi \sim n^{3/5} \nu^{1/5} l \quad \text{and} \quad \text{Equation 2.12}$$

$$\alpha^2 \sim \nu n \varphi. \quad \text{Equation 2.13}$$

More importantly, they hypothesize that because the inner shell is more concentrated than the outer shell, the branch naturally tends to diffuse outwards and thus

$$\varphi \sim \frac{nf l^3}{r^2 \xi}, \quad \text{Equation 2.14}$$

where  $f$  refers to the number of blobs. As a direct consequence of the hypothesized behavior of the chains, the swelling parameter can then be expressed as

$$\alpha(r) \sim \left(\frac{r}{l}\right)^{\frac{1}{6}} f^{-\frac{1}{12}} v^{\frac{1}{6}}, \quad \text{Equation 2.15}$$

which confirms that  $\alpha$  increases with  $r$  and along with the size of the blob.

On the other hand, at much smaller distances from the center and thus, small values of  $\alpha$ , the unswollen region becomes apparent. A crossover distance  $r_1$  between the two defined regimes is obtained by extrapolating Equation 2.15 to  $\alpha = 1$  and found to be

$$r_1 \sim f^{1/2} v^{-1} l. \quad \text{Equation 2.16}$$

Since in this region the blobs are no longer swollen, the monomer concentration and size of the blob respectively become,

$$\varphi \sim n^{-1/2} \quad \text{and} \quad \text{Equation 2.17}$$

$$\xi \sim n^{1/2} l. \quad \text{Equation 2.18}$$

Finally, considering Equation 2.14,

$$\varphi(r) \sim \left(\frac{r}{l}\right)^{-1} f^{1/2}. \quad \text{Equation 2.19}$$

More recent investigations on polymer brush behavior have extended the Daoud-Cotton model and more quantitatively identified these two regimes, particularly in the case of highly-grafted nanoparticles with long enough chains. Ohno et al<sup>54</sup>. defined a critical radius  $r_c$  as

$$r_c = r_0 \sigma^{*1/2} v^{*-1}, \quad \text{Equation 2.20}$$

where  $r_0$  is the nanoparticle radius. A concentrated polymer brush (CPB) regime exists for all  $h + r_0 \leq r_c$ . In this regime, the brush height  $h$  scales as  $N^{4/5}$ , in contrast to the  $h \propto N$  scaling for polymers grafted on flat brushes. For larger values of  $h$  where the brushes begin to swell, the chains transition to the semidilute polymer brush (SDPB) regime and  $h \propto N^{3/5}$  as  $N \rightarrow \infty$ . Dukes and co-workers<sup>55</sup> identified this crossover point for a series of nanoparticles (14 nm in diameter) with different grafting densities and molecular weights as seen in Figure 2.9 for a plot of  $h/N^{0.7}$  as a function of degree of polymerization,  $N$ . In the case of  $\sigma = 0.39$  chain/nm<sup>2</sup>, for instance, two different trends are distinguishable. The authors identified the CPB–SDPB transition or crossover height  $h_c$  to be 33 nm, corresponding to  $N \approx 315$  nm. More importantly, they found that below and above this transition point,  $h \propto N^{4/5}$  and  $h \propto N^{3/5}$ , respectively, which is consistent with previous work and theoretical predictions<sup>54,56</sup>.

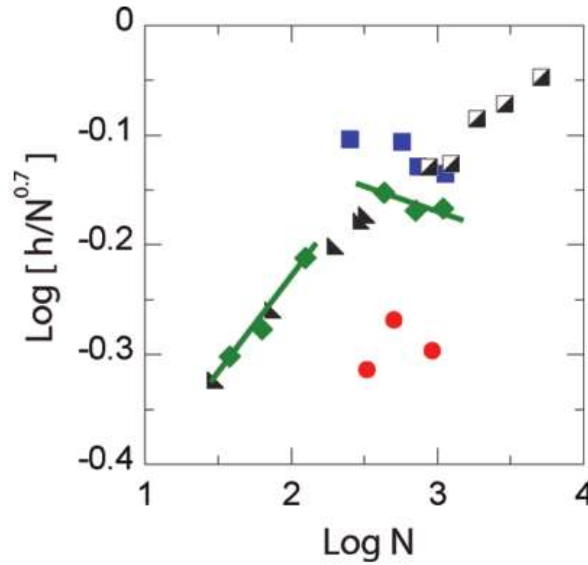


Figure 2.9 Data for 0.05 (red circles), 0.39 (green diamonds) and 0.55 (blue squares) chain/nm<sup>2</sup>.<sup>55</sup> Data from Ohno et al.<sup>54</sup> (half-filled squares) and Savin et al.<sup>57</sup> (inverted triangles) are also shown.

Their data for a higher grafting density of 0.55 chain/nm<sup>2</sup> also show that  $h \propto N^{3/5}$ . Only the SDPB regime can be probed, in this case, since most of the data points are above the determined  $h_c$  which is 41 nm according to Equation 2.20. The same situation applies to the lowest grafting density data (0.05 chain/nm<sup>2</sup>) since theory predicts  $h_c$  to be -1 nm.

## 2.5 Homopolymer blends of polystyrene and poly(vinyl methyl ether)

The above discussions so far deal with athermal systems ( $\chi \approx 0$ ) or where polymer grafted-nanoparticles are mixed with a chemically similar matrix, with the matrix chains having a lower molecular weight than the tethered brush to promote dispersion. It has been shown, however, that blend miscibility can also

be driven by a favorable mixing enthalpy ( $\chi < 0$ ) in the presence of a high molecular weight and chemically dissimilar matrix<sup>58,59</sup>. An example of such system is a homopolymer blend of PS/PVME.

It is known from literature<sup>60</sup> that the interaction parameter  $\chi$  for a blend of linear PS in PVME changes as a function of temperature. Although  $\chi$  is strongly negative over a wide range of temperatures, because the parameters  $A > 0$  and  $B < 0$  (Equation 1.2), this blend phase separates on heating—a property known as lower critical solution temperature (LCST) (Figure 2.10)<sup>48</sup>.

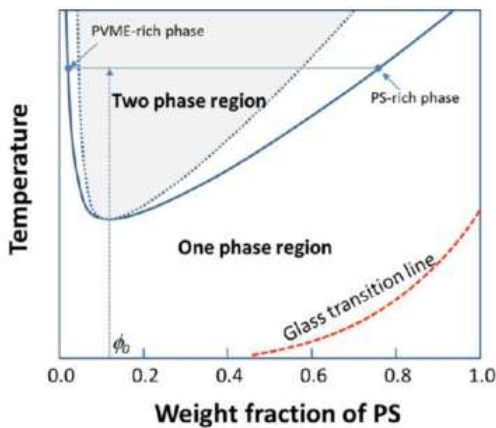


Figure 2.10 Phase diagram a PS/PVME blend exhibiting LCST behavior.<sup>61</sup>

The critical phenomenon for this system has been extensively investigated through the highly-sensitive small angle neutron scattering (SANS) technique, taking advantage of the scattering contrast from the deuterated PS component to observe large-scale concentration fluctuations in the blend.

Han et al.<sup>60</sup> performed a systematic study of the volume fraction or composition ( $\phi$ ), temperature and molecular weight dependence of  $\chi$  for a series

of dPS/PVME blends of varying molecular weights. In their investigation, they considered the scattering function for the polymer mixture in a homogenous phase to be described by the Random Phase Approximation (RPA) model<sup>62</sup>

$$\frac{1}{S(q)} = \frac{1}{N_A \phi P(q, N_A)} + \frac{1}{N_B (1-\phi) P(q, N_B)} - 2\chi, \quad \text{Equation 2.21}$$

where  $P(q, N)$  is the Debye function for Gaussian polymer coils.

The resulting coherent scattering data from SANS was fit to the Ornstein–Zernike scattering function given as

$$S(q) = \frac{S(0)}{1 + (q\xi)^2}, \quad \text{Equation 2.22}$$

where  $\xi$  is the correlation length which can thus be determined from the resulting plot. Moreover, from this equation, a Zimm plot of  $S(q)^{-1}$  vs  $q^2$  allowed the approximation of the scattering intensity at  $q=0$ . An estimate of the spinodal temperature, which designates the onset of density fluctuations that lead to phase separation, was obtained through an extrapolation to zero of both  $S^{-1}(q=0)$  and  $\xi^{-2}$  as a function of temperature. The authors found that while  $\chi$  has significant composition and temperature dependence, it does not noticeably depend on the molecular weight, as has been found later for other model polyolefin blends investigated by SANS<sup>63</sup>.

## Chapter 3      General Experimental Methods

### 3.1 Materials

Colloidal silica (MIBK-ST, effective diameter ~12 nm, ~30-31% silica in methyl isobutyl ketone) was kindly provided by Nissan Chemical Industries, Ltd. and used as received. Allyl 2-bromo-2-methylpropionate (98%, Sigma-Aldrich), chlorodimethylsilane (98%, Sigma-Aldrich), 10% platinum on activated carbon (Pt/C, Sigma-Aldrich), hexamethyldisilazane (HMDZ, 99.9%, Sigma-Aldrich), tetrahydrofuran (THF, 99.9+%, Sigma-Aldrich), copper (I) bromide (Cu(I)Br, 98%, Sigma-Aldrich), copper(II) bromide (Cu(II)Br, 99%, Sigma-Aldrich), Tin (II) 2-ethylhexanoate ( $\text{Sn}(\text{EH})_2$ , ~95%, Aldrich), *N,N,N',N'',N''*-Pentamethyldiethylenetriamine (PMDETA, 99%, Macron Chemicals), 4,4'-dinonyl-2,2'-dipyridyl (dNBpy, 97%, Sigma-Aldrich), toluene (ACS grade, 99.5%, Sigma-Aldrich), methanol (MeOH, 99.8%, Mallinckrodt), tetrahydrofuran (THF, 99.9%, Sigma-Aldrich) and hydrofluoric acid (48~51%, VWR) were used as received. Poly(vinyl methyl ether) (PVME,  $M_w = 46,000$  g/mol and  $M_w = 226,000$  g/mol) were kindly provided by Prof. Robert Briber (University of Maryland). Deuterated styrene (d-styrene,  $\geq 98\%$ , Polymer Source) was passed through a column of alternating inhibitor remover (for hydroquinone and monomethyl ether hydroquinone, Sigma-Aldrich) and aluminum oxide (activated, neutral, Brockmann I, Sigma-Aldrich) to remove the inhibitor.

## 3.2 Preparation of polymer-grafted SiO<sub>2</sub> nanoparticles

### 3.2.1 Synthesis of 1-(Chlorodimethylsilyl)propyl 2-bromoisobutyrate initiator

The initiator synthesis was performed following a modified procedure by Ponnampati et al.<sup>64</sup> In a round-bottom flask, 2.40 g of allyl 2-bromo-2-methylpropionate, 25 mL of chlorodimethylsilane and 55 mg of Pt/C catalyst (10% Pt) were combined and purged with nitrogen for 10 min. The solution was placed in an oil bath and stirred for 1 hr at 40 °C. After which, it was allowed to react for 2 days at room temperature. Once the reaction was complete, the Pt catalyst was removed by filtering through a 0.2 μm PTFE syringe filter. The excess chlorodimethylsilane solvent was removed by evaporation under nitrogen to afford a clear viscous liquid which was directly used in the next step.

### 3.2.2 Synthesis of 2-bromoisobutyrate functionalized SiO<sub>2</sub> nanoparticles

The surface functionalization of SiO<sub>2</sub> nanoparticles was conducted following a previously published protocol by Pyun et al.<sup>65</sup>. Briefly, 2.45 g of 1-(chlorodimethylsilyl)propyl 2-bromoisobutyrate initiator was added to a 24.5 g dispersion of SiO<sub>2</sub> in MIBK (30 wt%) under gentle reflux at 85 °C overnight and then cooled down to room temperature. After which, 1.77 mL of HMDZ was added as a capping agent for the remaining unfunctionalized hydroxyl groups on the silica surface. The reaction was allowed to proceed for 3 hr at room temperature and then under reflux at 60 °C for another 2 hr. The resulting mixture was centrifuged to remove the white solid precipitate. The remaining clear orange dispersion was added dropwise to a 4:1 (by vol) MeOH:H<sub>2</sub>O mixture

to precipitate colloids. The initiator-functionalized nanoparticles were recovered by centrifugation and washed several times by dissolving in THF and precipitating in hexane. This step was repeated at least ten times. Finally, the purified particles were recovered by centrifugation and dried.

### 3.2.3 Synthesis of polymer-grafted SiO<sub>2</sub> nanoparticles by AGET ATRP

A modified AGET ATRP reaction procedure was adopted from previous work by Jakubowski et al<sup>66</sup>. A Cu(II)Br catalyst and dNBpy ligand were combined with the styrene monomer in one flask and bubbled with N<sub>2</sub> for 30 minutes. In another flask, the Sn(EH)<sub>2</sub> reducing agent and initiator-functionalized silica were dissolved in toluene, purged and transferred to the first flask. The reaction mixture was then placed in an oil bath at 90°C and allowed to proceed for 20-40 hr. After polymerization, the reaction mixture was further diluted with THF, filtered through a column of neutral aluminum oxide to remove the catalyst, concentrated in vacuo and precipitated in excess amount of cold MeOH. The recovered polymer-functionalized nanoparticles were further purified through a mixed solvent precipitation method using toluene and methanol. This step ensured the removal of unfunctionalized silica nanoparticles as well as free chains from the bulk sample.

### 3.3 Preparation of nanocomposites

The preparation of the polymer nanocomposite followed a simple solution mixing procedure. Initially, poly(vinyl methyl ether) (PVME) was dried at 70°C

under vacuum overnight and cooled down to room temperature prior to use. A 20:80 (by weight) blend composition of SiO<sub>2</sub>-dPS/PVME was prepared by co-dissolving components in toluene and mixing at room temperature for at least 24 hours. The polymer blend was obtained by precipitating the solution in a large excess of hexane and collecting the solid by vacuum filtration. This was then dried in air for 2 days and annealed at 60°C under vacuum for at least 24 hours.

### 3.4 Fourier transform infrared spectroscopy (FTIR)

The presence of attached PS brushes was confirmed through FTIR measurements (Nicolet 4700 FTIR, Thermo Electron Corporation). This showed absorption bands corresponding to the different functional groups present in the sample.

### 3.5 Size exclusion chromatography (SEC)

The grafted brush molecular weight was determined using SEC (Viscotek 270 triple detection system). Prior to SEC measurements, the grafted polymers were cleaved from the surface of silica by first dissolving ~5 mg of the hybrid nanoparticles in 2 ml THF and then adding 2 ml of a 2% (v/v) solution of aqueous HF. After stirring the solution overnight, the polymer was reprecipitated in excess amount of methanol and dried under vacuum for at least 24 hr.

### 3.6 Thermo-gravimetric analysis (TGA)

Weight losses due to the tethered initiator and polymer brush were determined by TGA (TGA Q500, TA Instruments). The experiments were conducted under argon atmosphere and the samples were heated from 25 °C to 800 °C at a heating rate of 10 °C/min. The resulting effective weight losses were then used in the calculation of the polymer grafting density.

### 3.7 Calculation of polymer grafting density

The polymer grafting density,  $G_p$ , was determined according to the following equation from an earlier work by Pasetto et al<sup>67</sup>.

$$G_p = \frac{\frac{W\%_{\text{polymer+initiator+silica}}}{100-W\%_{\text{polymer+initiator+silica}}} - \frac{W\%_{\text{silica+initiator}}}{100-W\%_{\text{silica+initiator}}}}{(M_w)(S_{sp})} \times N_A , \quad \text{Equation 3.1}$$

where  $W\%_{\text{polymer+initiator+silica}}$  and  $W\%_{\text{silica+initiator}}$  are the residual weight losses from the polymer-grafted and initiator-grafted  $\text{SiO}_2$  nanoparticles from TGA measurements, respectively;  $M_w$  is the weight average molecular weight from SEC experiments,  $S_{sp}$  is the specific surface area of  $\text{SiO}_2$  ( $1.93 \times 10^{20} \text{ nm}^2/\text{g}$ ) and  $N_A$  is Avogadro's number ( $6.022 \times 10^{23} \text{ molecules/mol}$ ).

### 3.8 Dynamic light scattering (DLS)

The hydrodynamic radius ( $R_h$ ) was determined for dilute solutions (0.1 mg/ml) of the polymer-grafted nanoparticles in toluene and cyclohexane using DLS (Brookhaven Instrument, BI-200SM). The solutions were allowed to equilibrate at the desired temperature for at least 30 min prior to measurements. Scattering intensities at various angles (45°, 60°, 90° and 120°) were obtained using a He-Ne laser having a wavelength of 637 nm. The diffusion coefficient ( $D_{\text{coeff}}$ ) was determined using the method of cumulants and subsequently applied in the Stokes-Einstein equation (Equation 3.2) to calculate for  $R_h$

$$R_h = \frac{k_B T}{6\pi\eta D_{\text{coeff}}}, \quad \text{Equation 3.2}$$

where  $k$  is the Boltzmann constant ( $1.38 \times 10^{-23} \text{ m}^2\text{kg/Ks}^2$ ),  $T$  is temperature in kelvin and  $\eta$  is the viscosity of the solvent at temperature  $T$ .

### 3.9 Small angle x-ray scattering (SAXS)

The structure and inter-particle distance of the hybrid nanoparticles in bulk and in the blend were confirmed using SAXS (Rigaku SMax3000 with a MicroMax-007HF rotating anode generator). For the pure polymer-grafted  $\text{SiO}_2$  nanoparticles, a highly-ordered structure was confirmed by  $q_1^* : q_2^* :: 1 : \sqrt{3}$ , where

$q_1$  and  $q_2$  denote the first- and second-order scattering intensity peaks, respectively<sup>41</sup>. The inter-particle spacing,  $d$ , is given by

$$d = \frac{2\pi}{q_1^*}. \quad \text{Equation 3.3}$$

### 3.10 Small angle neutron scattering (SANS)

SANS experiments were performed on the NG3 30m SANS beamline at the National Institute of Standards and Technology Center for Neutron Research (NCNR) in Gaithersburg, MD. Measurements were performed at a neutron wavelength of 6 Å and three sample-to-detector distances of 13m, 4m and 1m, thus accessing a  $q$ -range of 0.003 Å<sup>-1</sup> to 0.5 Å<sup>-1</sup>. The obtained raw data were corrected for detector sensitivity, background and empty cell contributions using IGOR Pro 6.34A, allowing data normalization to an absolute scattering intensity. Data analysis was performed using fitting models available in SASView and the following scattering length density (SLD) values summarized in Table 3.1.

Table 3.1. Neutron and x-ray SLD values of relevant compounds.

Compound	Neutron SLD (Å <sup>-2</sup> )	Cu Kα SLD (Å <sup>-2</sup> )
SiO <sub>2</sub>	3.48 x10 <sup>-6</sup>	1.89 x10 <sup>-5</sup>
Deuterated polystyrene (dPS)	6.46 x10 <sup>-6</sup>	9.60 x10 <sup>-6</sup>
Polystyrene (PS)	1.41 x10 <sup>-6</sup>	9.61 x10 <sup>-6</sup>
Poly(vinyl methyl ether) (PVME)	3.53 x10 <sup>-7</sup>	9.66 x10 <sup>-6</sup>

Deuterated toluene	$5.68 \times 10^{-6}$	$8.03 \times 10^{-6}$
Deuterated cyclohexane	$6.67 \times 10^{-6}$	$7.54 \times 10^{-6}$

### 3.11 Transmission electron microscopy (TEM)

TEM measurements were performed at the National Institute of Standards and Technology in Gaithersburg, MD. The composite sample was thinned into a lamellar, electron transparent (~ 150 nm) section and mounted onto a copper half-grid by focused ion beam (FIB) milling, optimized for soft materials, as described elsewhere.<sup>68</sup> The spatial distribution of the nanoparticles in the composite material was imaged using an FEI Titan TEM in bright-field mode at 300 kV with a 40  $\mu\text{m}$  objective aperture inserted.

# **Chapter 4      Distinct      Wetting-Dewetting      and Dispersion-Aggregation      Transitions      in      Blends      of Polymer-Grafted      Nanoparticles      and      a      Chemically Dissimilar Polymer Matrix**

## **4.1 Introduction**

An increasing demand for functionally advanced materials has prompted a considerable amount of work geared towards understanding structure-property relationships in polymer blends and hybrid nanoparticle composites<sup>69,70</sup>. It has been shown, for instance, that 1-dodecanethiol-functionalized ZnO nanorods can enhance the mechanical and shape memory characteristics of polyurethane materials<sup>71</sup>. For high ZnO loadings of about 12 vol %, clusters of ZnO begin to form, thus, significantly increasing the material's tensile modulus. This hierarchical morphology was found to be primarily responsible for the observed shape memory enhancement of the nanocomposite. In the case of spherical nanoparticles embedded in a polystyrene matrix, on the other hand, it was found that at high silica volume fractions, a percolating network forms and causes a fast increase in the reinforcement factor. This behavior was attributed to strong particle-particle interactions at the interface, thereby reducing the local deformability of the resulting material<sup>72</sup>.

Critical to achieving these properties in the composite material is the controlled distribution of nanoparticles within the host polymer matrix. A common

route used to improve the compatibility between the inorganic and organic components of the blend is the surface functionalization of nanoparticles with polymers<sup>2,15,73,74</sup>. The states of dispersion and aggregation in such systems are thus fundamentally determined by entropic and enthalpic contributions that result from the interplay of tunable characteristics such as the grafted brush and matrix chemistries, grafting density, polymer molecular weight and blend composition.

In the case of nanoparticles densely grafted with polymers that are chemically similar to the surrounding matrix, dispersion and aggregation due to brush wetting and dewetting, respectively, are primarily driven by entropic forces. The gain in mixing entropy from brush penetration promotes dispersion; while the penalty from conformational entropy loss during wetting drives demixing and hence, aggregation. Stabilizing particle dispersion is thus controlled by tuning the nanoparticle grafting density and molecular weights of the polymer brush and matrix (i.e. grafted chain/matrix chain ratio), as demonstrated by previous studies<sup>40,41,75,76</sup>.

Two important points are clear in the case of athermal blends ( $\chi=0$ ): first, in the high grafting density limit, nanoparticles are well distributed in a polymer matrix as long as the matrix molecular weight is comparable to or lower than that of the brush; second, the wetting/dewetting and dispersion/aggregation events are analogous and indistinguishable.

In this chapter, we investigate the phase behavior of polystyrene (PS)-grafted SiO<sub>2</sub> nanoparticles in a chemically distinct poly(vinyl methyl ether)

(PVME) matrix. This system is known to have a  $\chi < 0$  at low temperatures and  $\chi > 0$  at high temperatures, characteristic of a LCST system. We first describe in detail the synthesis and characterization of hydrogenated and deuterated PS-grafted SiO<sub>2</sub> nanoparticles (SiO<sub>2</sub>-dPS) and preparation of the SiO<sub>2</sub>-hPS/PVME and SiO<sub>2</sub>-dPS/PVME composites. Through a combination of small angle x-ray scattering (SAXS) and small angle neutron scattering (SANS), we demonstrate the dispersion of these nanoparticles in a high molecular weight PVME at low temperatures, driven by favorable entropic and enthalpic interactions. We then elucidate the *gradual wetting-dewetting* phenomenon that is distinct from the dispersion-aggregation transition as the system approaches a phase boundary at high temperatures.

## 4.2 Methodology

### 4.2.1 Synthesis of deuterated polystyrene (SiO<sub>2</sub>-dPS) and hydrogenated polystyrene (SiO<sub>2</sub>-PS) grafted nanoparticles by surface-initiated AGET ATRP

Deuterated PS brushes were grown from the surface of SiO<sub>2</sub> following the synthesis scheme shown below (Scheme 4.1). Initially, initiator-functionalized SiO<sub>2</sub> nanoparticles were prepared as previously described in Chapters 3.2.1 and 3.2.2 (Scheme 4.1a), and subsequently used in the polymerization step (Scheme 4.1b). In a round bottom flask (flask 1), 250 mg of the initiator-grafted nanoparticles and 30.88  $\mu$ L of Sn(EH)<sub>2</sub> was dissolved in 20 mL of toluene. In another flask (flask 2), 4 mL of d-styrene was combined with 23.68 mg of Cu(II)Br and 86.68 mg of dNBpy. Both flasks were purged with N<sub>2</sub> for at least 30 minutes.

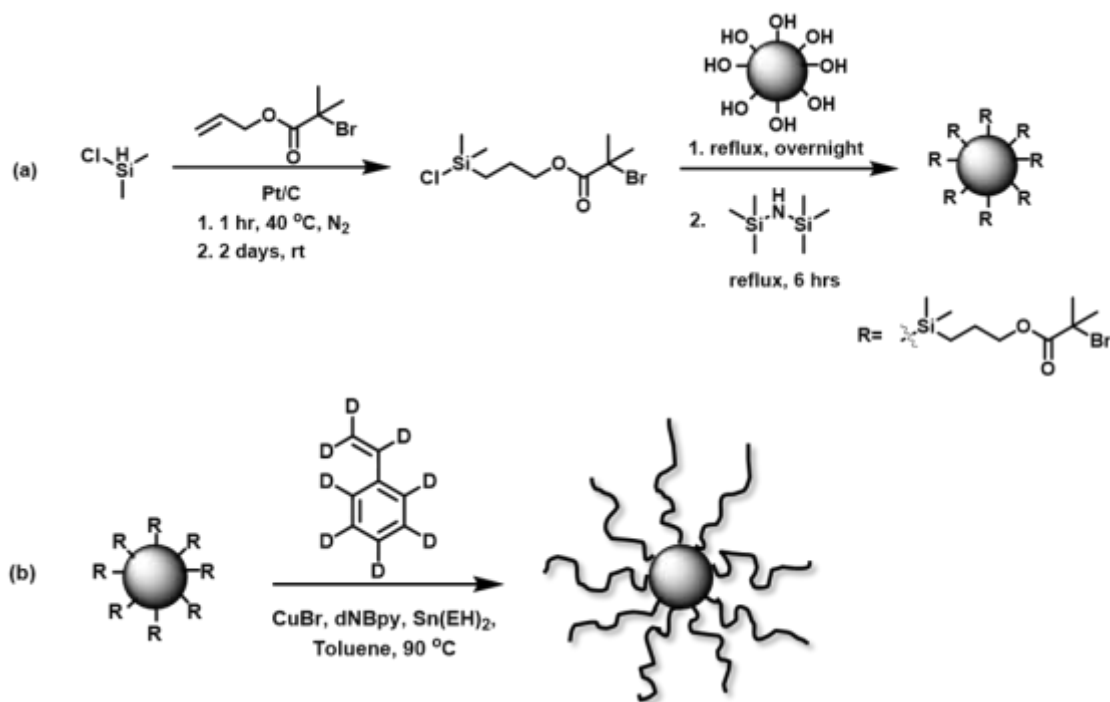
The contents of flask 1 were then transferred to flask 2 using a cannula and the resulting solution was placed in an oil bath at 90 °C. The polymerization reaction was allowed to proceed for 40 hr.

Hydrogenated PS brushes were synthesized in a similar fashion. In one flask, 500 mg of the initiator-grafted nanoparticles was combined with 30.88  $\mu\text{L}$  of  $\text{Sn}(\text{EH})_2$  and dissolved in 80 mL of toluene. In another flask, 20 mL of styrene was added to 23.68 mg of  $\text{Cu}(\text{II})\text{Br}$  and 86.68 mg of dNBpy. Both flasks were purged with  $\text{N}_2$  for at least 30 minutes and then combined using a cannula. The reaction was allowed to proceed for 30 hr at 90 °C.

After polymerization, the reaction mixture was exposed to air and diluted with THF. It was then passed through a column of neutral aluminum oxide twice to ensure the removal of catalyst. The excess THF and toluene were removed by rotavap and the remaining viscous liquid was added dropwise to a large excess of cold MeOH to yield white solid precipitates. The polymer-grafted nanoparticles were recovered by centrifugation and washed twice more by redissolving in THF and precipitating in MeOH.

In order to remove any ungrafted  $\text{SiO}_2$  nanoparticles and unattached polymer chains, the recovered material was subjected to further purification by a mixed solvent precipitation method. Briefly, the recovered material was dissolved in toluene and centrifuged for 5 min. This step ensured that any unfunctionalized  $\text{SiO}_2$  remained at the bottom of the tube. The supernatant containing the polymer-grafted nanoparticles and any unattached polymer chains was collected

and transferred to another flask. The flask was heated to 50 °C for about 10 min to homogenize the solution, after which, it was allowed to cool down. MeOH was added dropwise until a cloudy suspension formed. The flask was heated back up to 50 °C to recover the single phase state. Finally, the solution was transferred to a separatory funnel and was left undisturbed for 2 days. The bottom layer containing the polymer-grafted nanoparticles were collected, added to an excess amount of MeOH, centrifuged and dried under vacuum.



Scheme 4.1 General synthesis scheme for the preparation of (a) initiator-functionalized and (b) deuterated/hydrogenated polystyrene-grafted SiO<sub>2</sub> nanoparticles.

#### 4.2.2 Preparation of SiO-dPS/PVME and SiO<sub>2</sub>-PS/PVME nanocomposites

Polymer blends close to the critical composition (20% PS and 80% PVME by volume) were prepared following a simple solution mixing procedure. 37.7 mg

of SiO-dPS (or SiO<sub>2</sub>-PS) nanoparticles and 150.6 mg of PVME were co-dissolved in toluene and stirred for at least 24 hr. The composite was obtained by precipitating in an excess amount of hexane and collecting the solid by vacuum filtration. The resulting material was allowed to dry in air for 2 days and annealed at 60 °C under vacuum for at least 24 hr.

#### 4.2.3 Preparation of nanocomposites for SANS

The nanocomposites were first pressed into 1mm-thick pellets at 70 °C under high vacuum for at least 15 mins to ensure the expulsion of trapped air bubbles. The pellets were sandwiched between two glass windows and secured in demountable titanium sample cells available at NCNR. The sample cells were then placed in a sample holder with a temperature-controlled fluid circulation system.

### 4.3 Results and discussion

Polystyrene brushes were grown from the surface of SiO<sub>2</sub> using the AGET ATRP technique which provided good control over the architecture and molecular weight of the grafted polymer. The attachment of PS on the surface was confirmed through FTIR as shown in the resulting spectra, with the characteristic absorption bands for the different functional groups assigned (Figure 4.1).

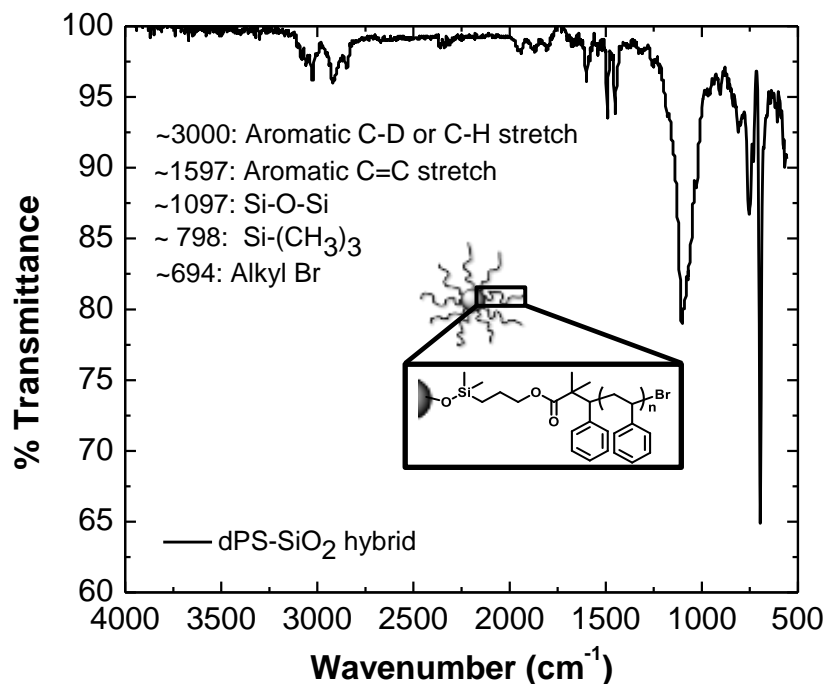


Figure 4.1 IR spectra of the hybrid nanoparticle showing signature absorption bands of the different functional groups of the tethered brush.

The molecular weight of the tethered brush was determined by SEC following the cleavage of dPS and PS from the SiO<sub>2</sub> surface using a 2% (v/v) aqueous solution of HF. The obtained chromatogram (Figure 4.2) showed a monomodal peak indicating weight average molecular weights,  $M_w$ , of 33,000 g/mol and 20,000 g/mol for dPS and PS, respectively.

Thermo-gravimetric analysis on both the initiator- and polymer-grafted (SiO<sub>2</sub>-dPS33k) nanoparticles allowed the determination of the weight percent of the tethered groups.

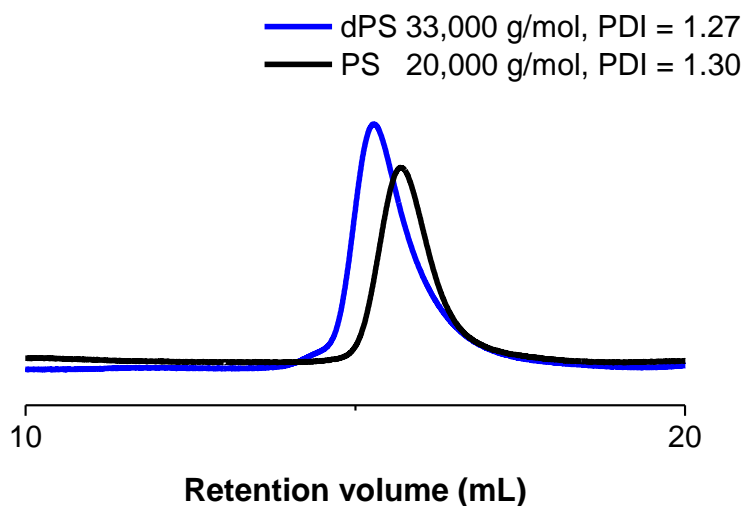


Figure 4.2 Size exclusion chromatogram of cleaved dPS and PS brush.

Shown in Figure 4.3 are the resulting TGA plots indicating a residual weight loss of 7% from the initiator, 78% from PS20k and 89% from dPS33k. The SiO<sub>2</sub>-PS20k and SiO<sub>2</sub>-dPS33k hybrid nanoparticles had polymer grafting densities of 0.6 and 0.7 chain/nm<sup>2</sup>, respectively, using Equation 3.1.

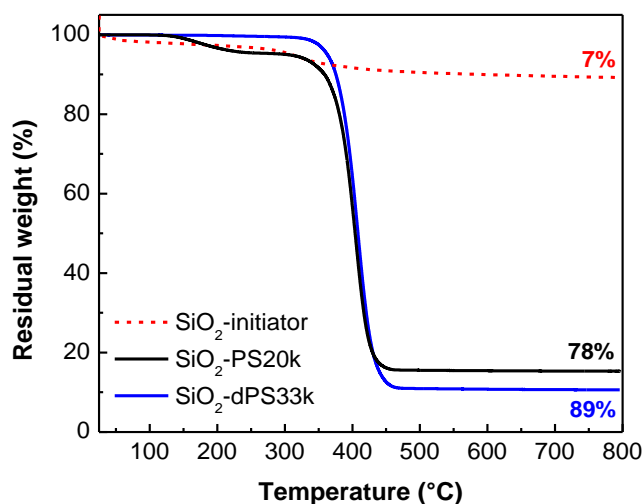
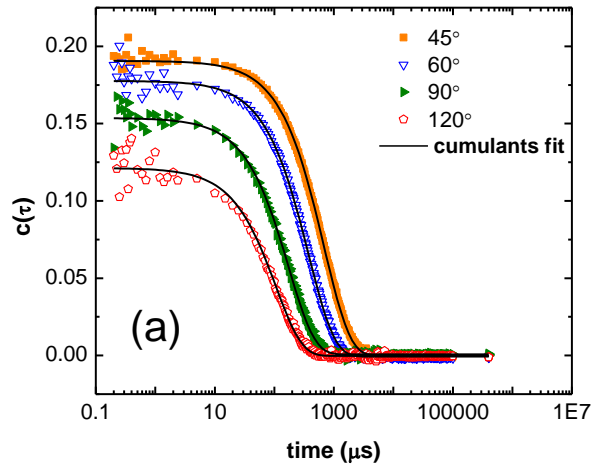


Figure 4.3 TGA plots of the SiO<sub>2</sub>-dPS33k hybrid (solid line) and initiator-grafted (dashed line) nanoparticles showing the weight losses due to the tethered brush and initiator, respectively.

The hydrodynamic radius,  $R_h$ , was also determined for dilute suspensions of the hybrid nanoparticles in toluene at room temperature. A 0.1 mg/ml concentration was prepared and subjected to DLS measurements at various angles and trials. The correlation functions at all angles (Figure 4.4) show a single exponential decay which can be fit to the method of cumulants in which the autocorrelation function of the scattered light  $g^{(2)}(\tau)$  is expressed as<sup>77</sup>

$$g^{(2)}(\tau) = B + \beta \exp(-2\Gamma\tau) \left( 1 + \frac{\mu_2}{2!} \tau^2 - \frac{\mu_3}{3!} \tau^3 \dots \right)^2. \quad \text{Equation 4.1}$$

DLS measurements in a good solvent such as toluene provide a good estimate of the particle size since the brushes are expected to be in their fully-stretched conformation. From a linear extrapolation of  $\Gamma$  (obtained from the fit) versus the scattering wave vector  $q^2$ , the diffusion coefficient was determined and used directly in the Stokes-Einstein equation (Equation 3.2) to yield a hydrodynamic radius of 58.0 ( $\pm 0.1$ ) nm for SiO<sub>2</sub>-dPS33k and 36.4 ( $\pm 0.1$ ) for SiO<sub>2</sub>-PS20k.



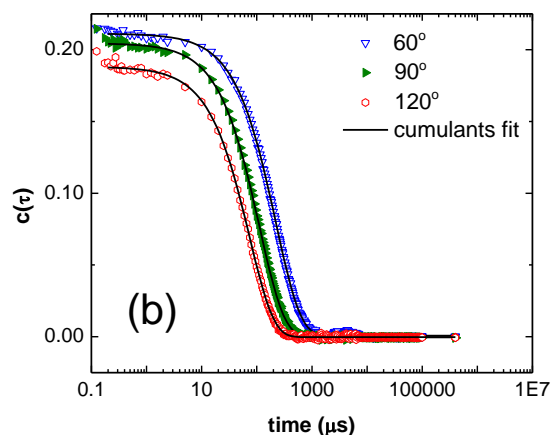


Figure 4.4 Correlation plots at various angles for the (a) SiO<sub>2</sub>-dPS33k and (b) SiO<sub>2</sub>-PS20k nanoparticles in toluene. The solid black line is the cumulants fit.

A summary of the hybrid nanoparticles characterized using the above techniques is presented in Table 4.1 below.

Table 4.1 Characteristics of hybrid nanoparticles under study.

Hybrid nanoparticle	Molecular weight (g/mol)	PDI	Grafting density (chain/nm <sup>2</sup> )	Hydrodynamic radius (nm)
SiO <sub>2</sub> -dPS33k	33,000	1.27	0.7	58.0 ± 0.1
SiO <sub>2</sub> -PS20k	20,000	1.30	0.6	36.4 ± 0.1

The structural profile and size of the hybrid nanoparticles in the bulk (solvent-free) were also analyzed using SAXS. It is known that concentrated particles exhibit liquid-like ordering characterized by a peak in the pair correlation function. In the scattered intensity, this translates into a peak denoting Fourier transform of the real space distribution of the material. Higher order peaks then

become visible when the particles pack closer together, ultimately having a semi-crystalline order. The first peak in the scattering intensity profile in Figure 4.5a, denoted as  $q_1^*$ , is thus a direct measure of the inter-particle (core-to-core) distance,  $d$ , of the SiO<sub>2</sub> nanoparticles according to the relation,

$$d = \frac{2\pi}{q^*} . \quad \text{Equation 4.2}$$

Both first- and second-order intensity peaks are observed, implying a highly-ordered structure of the hybrid nanoparticles<sup>41</sup> confirmed by  $q_1^* : q_2^* :: 1 : \sqrt{3}$ . In the case of no matrix or solvent, the inter-particle distance can then be used to estimate the height of the brush using the known diameter of bare silica (12.0 nm), the brush height is approximately 10.3 nm. The information extracted from the scattering profiles of both hybrid nanoparticles is presented in Table 4.2.

Table 4.2 Characteristics of hybrid nanoparticles from SAXS measurements.

Hybrid nanoparticle	$q_1^*$	$q_2^*$	Inter-particle distance, $d$ (nm)	Brush height (nm)
SiO <sub>2</sub> -dPS33k	0.019	0.033	33.0	10.5
SiO <sub>2</sub> -PS20k	0.022	0.039	28.6	8.3

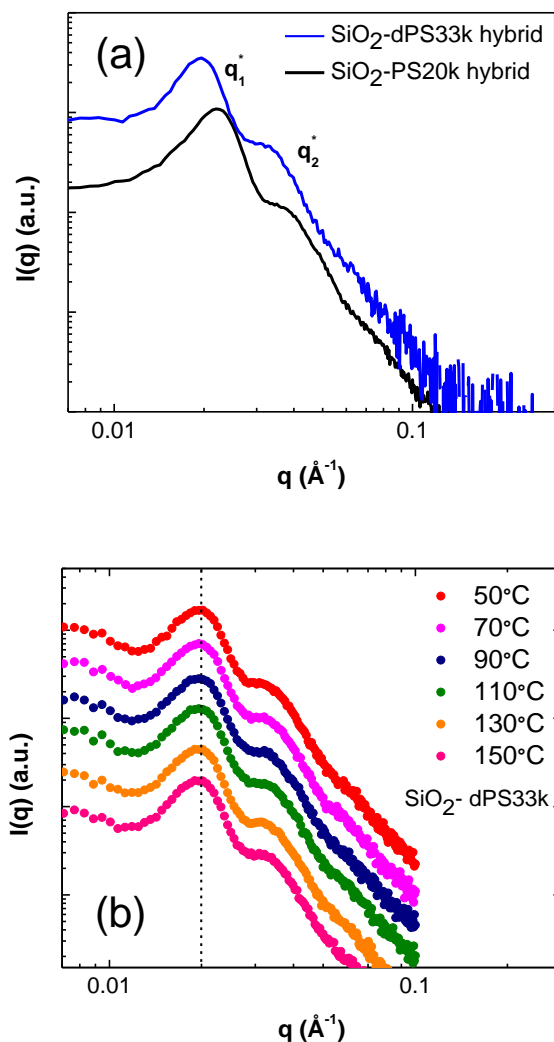


Figure 4.5 SAXS scattering intensity profile of the pure hybrid nanoparticles (no matrix or solvent) at (a) room temperature and (b) scattering intensity profile of SiO<sub>2</sub>-dPS33k at higher temperatures.

Any changes in the local arrangement of the SiO<sub>2</sub> core, which is directly related to changes in the height of the brush, can be assessed in SAXS due to the large scattering contrast between SiO<sub>2</sub> ( $1.89 \times 10^{-6} \text{ \AA}^{-2}$ ) and dPS ( $9.60 \times 10^{-6} \text{ \AA}^{-2}$ ). The same is true for a PS brush ( $9.61 \times 10^{-6} \text{ \AA}^{-2}$ ). Figure 4.5b presents the resulting scattering profiles for an annealed sample of the SiO<sub>2</sub>-dPS33k hybrid

nanoparticles measured at higher temperatures. There was no observable change in the structure factor peak position and hence, in the brush height, for the pure hybrid system. This discounts any brush relaxation effects in the analysis of the SiO<sub>2</sub>-dPS33k/PVME composites as will be discussed later.

The highly-grafted SiO<sub>2</sub>-dPS33k nanoparticles were dispersed in a PVME matrix of 46,000 g/mol (PVME46k) and 226,000 g/mol (PVME226k) molecular weight. The composites were then analyzed in SAXS at room temperature to evaluate the dispersion of the nanoparticle within these high molecular weight matrices. In Figure 4.6a, there is an obvious change in the structure factor peak position going from the case of a hybrid nanoparticle in the absence of PVME to the case where the nanoparticles are surrounded by a PVME matrix. More importantly, the most significant increase in inter-particle distance is observed in the presence of a much higher molecular weight PVME of 226,000 g/mol. In figure 4.6b, the largest separation of particles is achieved also when SiO<sub>2</sub>-PS20k is in the presence of a high molecular weight PVME matrix.

This is a clear indication that the favorable enthalpic interactions between dPS and PVME play a large role in facilitating the dispersion of SiO<sub>2</sub> nanoparticles even in the presence of a high molecular weight matrix. As temperature is increased, the scattering intensity peak gradually shifts towards higher  $q$ , implying a decrease in inter-particle distance as the particles pack closer together (Figure 4.7).

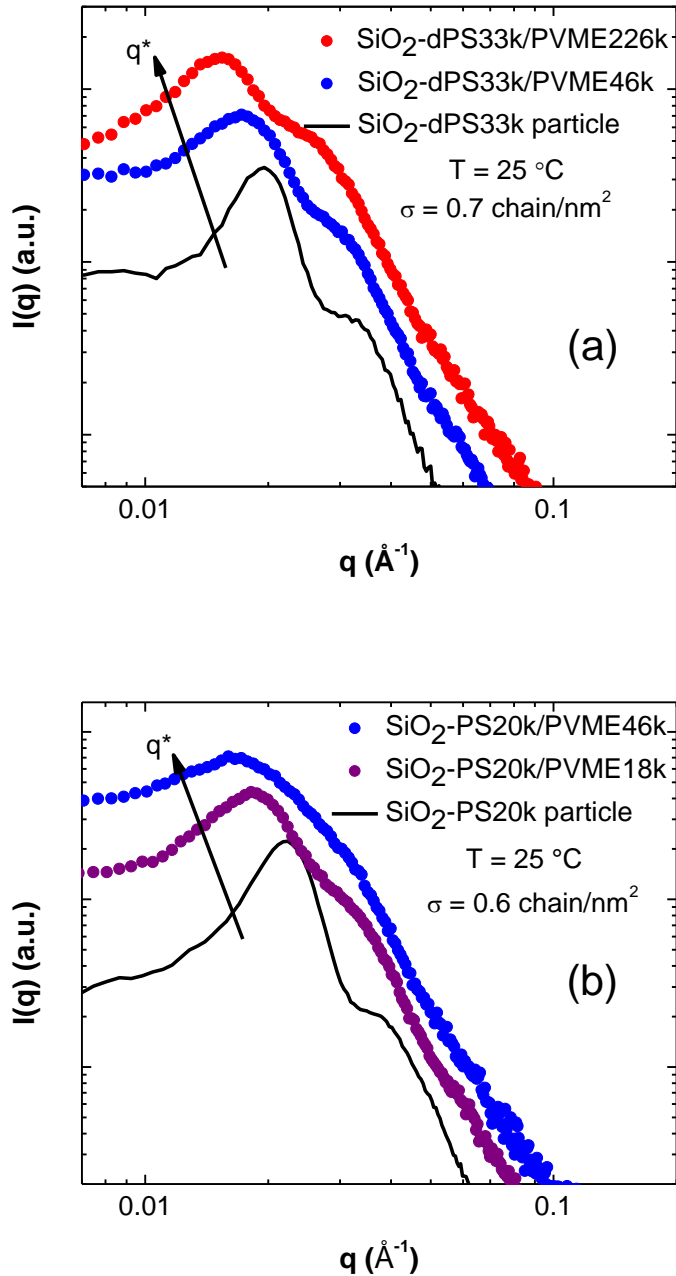


Figure 4.6 SAXS scattering intensity profiles of (a)  $\text{SiO}_2$ -dPS33k/PVME226k and  $\text{SiO}_2$ -dPS33k/PVME46k composites and (b)  $\text{SiO}_2$ -PS20k/PVME46k and  $\text{SiO}_2$ -PS20k/PVME18k composites.

Since the concentration of particles is constant, this is a strong indication that the PVME matrix chains are segregating from the particles and hence,

dewetting the grafted dPS brushes. It is also worth noting that at the highest temperature, the peak coincides with that of the pure hybrid nanoparticle in its melt state as shown in the case of SiO<sub>2</sub>-dPS33k/PVME226k (Figure 4.7a), suggesting a complete dewetting and aggregation of the nanoparticles.

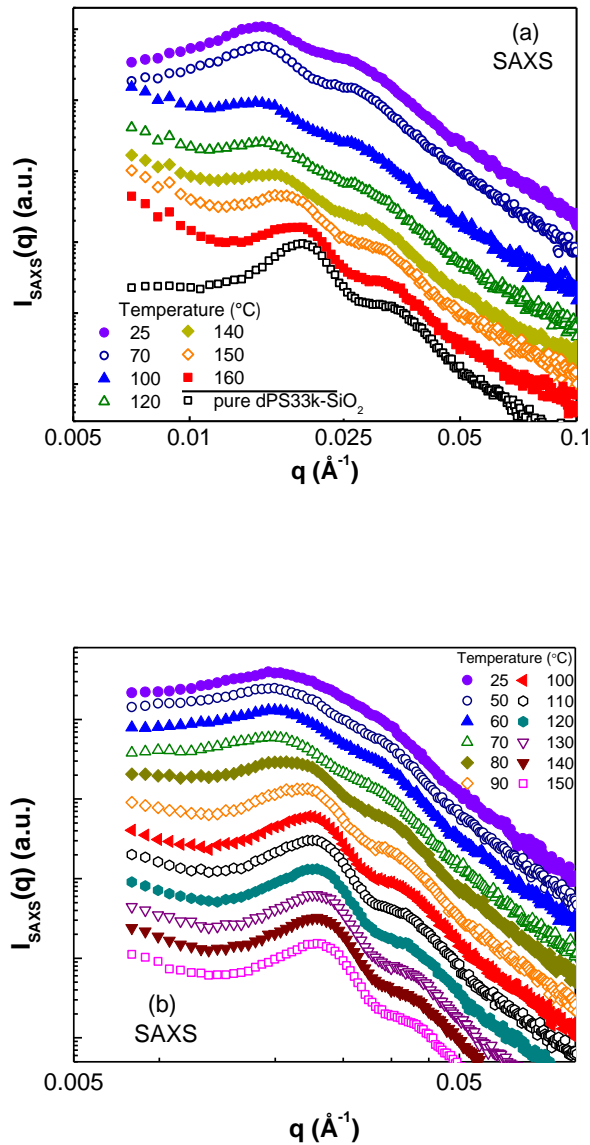


Figure 4.7 Temperature dependence of SAXS scattering intensity data for (a) SiO<sub>2</sub>-dPS33k/PVME226k blend, and for (b) SiO<sub>2</sub>-PS20k/PVME226k blend.

A closer inspection of the low  $q$  data in Figure 4.7 reveals an upturn in intensity as a function of temperature. In this low  $q$  regime, SAXS measurements are most sensitive to large scale inhomogeneities from the  $\text{SiO}_2$  component, consistent with the observed transition to an aggregated state at high temperatures. SANS, on the other hand, is sensitive to all three components of the blend. Particularly, due to the large neutron contrast between dPS ( $6.46 \times 10^{-6} \text{ \AA}^{-2}$ ) and PVME ( $3.53 \times 10^{-7} \text{ \AA}^{-2}$ ), it becomes a powerful tool in probing large scale concentration fluctuations that arise from the grafted polymer-matrix polymer phase separation. Thus, from this point forward, we focus on the  $\text{SiO}_2$ -dPS33k/PVME226k system in order to fully take advantage of the SANS analysis that can be carried out through the large contrast between the brush and the matrix.

The large scale concentration fluctuations are indeed captured in the low  $q$  behavior of the coherent SANS intensity data shown in Figure 4.8, consistent with a LCST behavior where increasing concentrations are observed with increasing temperature.

The scattering at low  $q$  for binary blends is described well by the Ornstein-Zernike equation

$$I_{\text{SANS, Coh}}(q) = \frac{I(0)}{1 + \xi^2 q^2}, \quad \text{Equation 4.3}$$

where  $\xi$  is the correlation length. The scattering intensity in the forward direction or at zero angle,  $I(0)$ , is estimated through the extrapolation of  $1/I_{\text{SANS, Coh}}(q)$  vs.  $q^2$

to  $q=0$  (Figure 4.9b); while  $\xi$  is calculated from the square root of the ratio of the resulting slope to intercept.

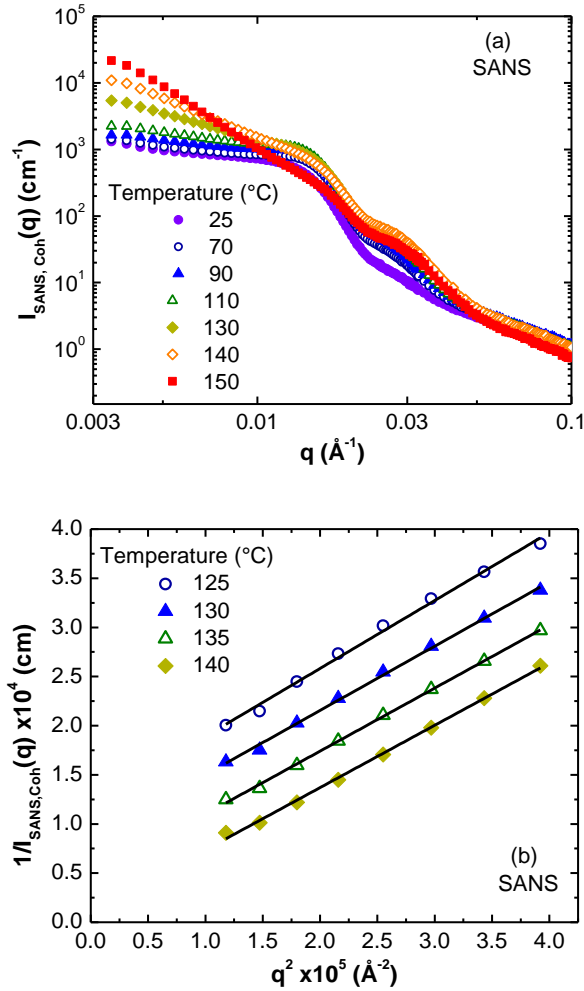


Figure 4.8 (a) Temperature dependence of the coherent SANS intensity data of the dPS33k/PVME226k blend and (b) Ornstein-Zernike plot of selected high temperature SANS data to determine  $I(0)$  and  $\xi$ .

Both  $I(0)$  and  $\xi$  are parameters that describe the concentration fluctuations in the system especially as it approaches the two-phase region. In fact, as the spinodal condition is approached,  $I(0)^{-1}$  and  $\xi^{-2}$  should vary linearly with  $T^{-1}$

(Figure 4.9a) and allow an extrapolation to  $l(0)^{-1} = 0$  to identify the spinodal temperature,  $T_s$ <sup>78</sup>. The spinodal condition is found to occur at  $\sim 143 \pm 2$  °C. This behavior in  $l(0)$  and  $\xi$  also bears notable similarity to that observed for both polymer blends and star-PS/PVME mixtures<sup>79,80</sup>. A remarkable result is that this calculated  $T_s$  is well above the observed onset of the wetting-dewetting transition (90 °C) as depicted in Figure 4.9b.

At this point, key findings about the SiO<sub>2</sub>-dPS33k/PVME226k system under study are worth noting: first, the wetting-dewetting transition is a gradual, second-order transition that occurs at  $\sim 90$  °C, distinct from the first-order dispersion-aggregation transition normally observed for homopolymers of dPS/PVME; second, this wetting-dewetting transition occurs well below the observed phase separation temperature and dewetting continues to occur above the spinodal temperature in the aggregated state.

Through a collaborative effort with Martin and Jayaraman, coarse-grained molecular dynamics (CGMD) simulations were performed on dissimilar graft-matrix systems to highlight this gradual wetting/dewetting transition. The graft and matrix Kuhn segment (“effective monomer”) concentration profiles in Figure 4.10a show that there is a gradual decrease in overlap between the graft and the matrix monomer concentration profiles. In Figure 4.10b, the wet monomer fraction was calculated as a function of temperature for two grafted nanoparticle volume fractions ( $\varphi_G = 0.13$  and  $\varphi_G = 0.20$ ). As expected, the absolute value of the wet monomer fraction increases with increasing  $\varphi_G$  across the entire temperature range. On the other hand, when measurements of the normalized

wet monomer fraction (normalized by the surface area of the aggregates) are calculated, the data collapses onto a single curve regardless of the grafted polymer composition (Figure 4.10b inset). Remarkably, in both accounts, there is no observation of discontinuity in the wetting fraction and only a continuous transition.

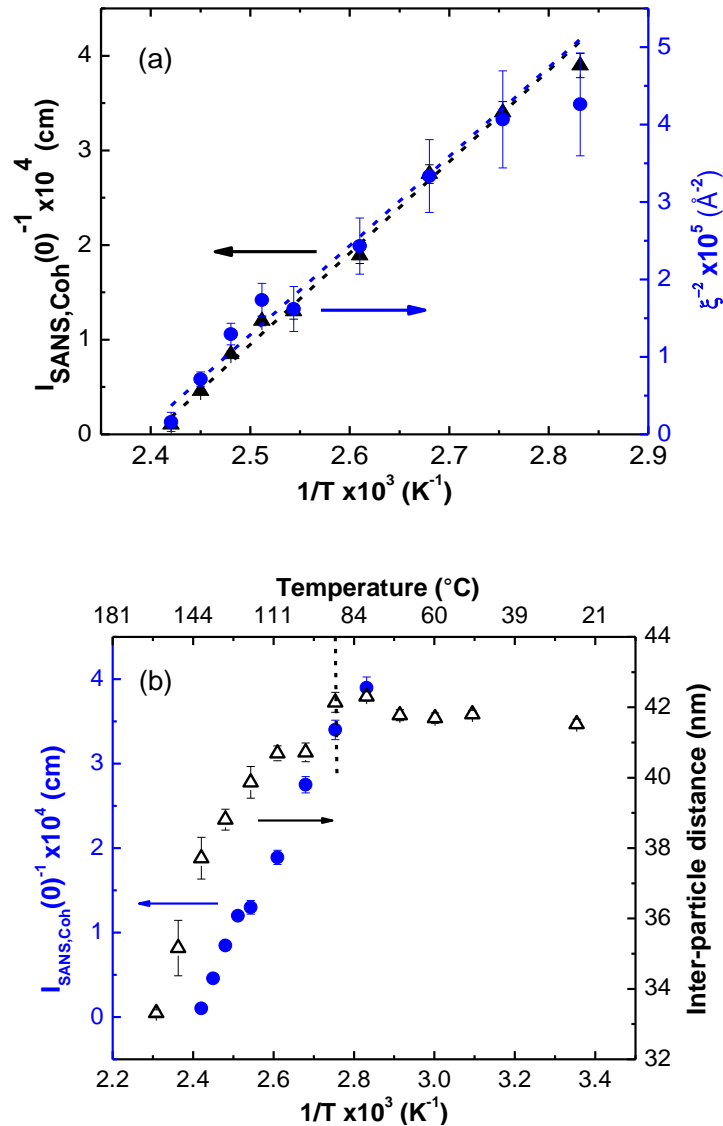


Figure 4.9 (a) Zero-angle scattering and correlation length as a function of temperature and (b) temperature dependence of the zero-angle scattering and inter-particle distance.

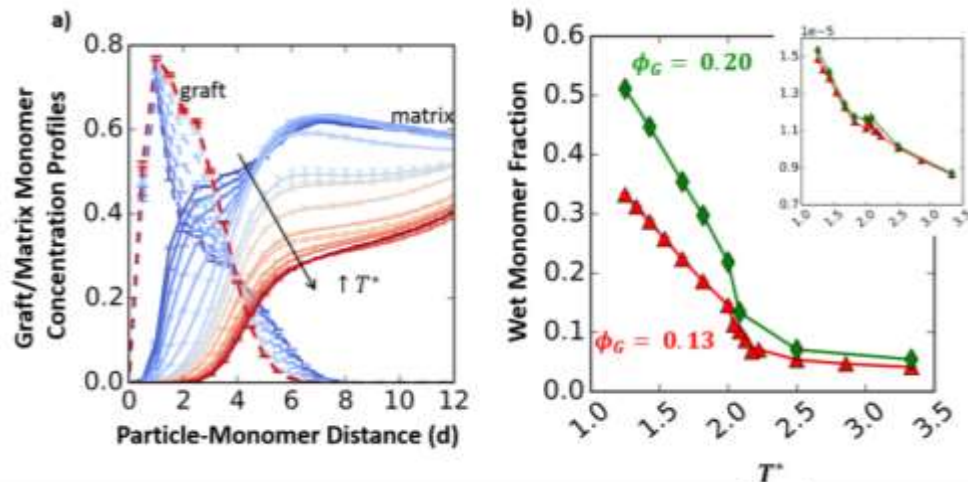


Figure 4.10 (a) Graft monomer (dashed lines) and matrix monomer (solid lines) concentration versus distance from the particle surface and b) wet monomer fraction versus reduced temperature,  $T^*$ .

The differences in the behavior of a grafted and free polymer chain that give rise to the above experimental observations are confirmed through CGMD simulations on a negative  $\chi$  graft-matrix polymer pair. The main premise using this technique is that enthalpic and entropic contributions to the change in free energy going from a mixed (dispersed) to demixed (aggregated) state defined as

$$\Delta A_{\text{mixed} \rightarrow \text{demixed}} = \Delta U - T\Delta S, \quad \text{Equation 4.4}$$

account for differences in the behavior of grafted and free blends.  $\Delta U$  can also be interpreted as the change in the number of contacts between the brush and matrix monomers going from the dispersed to aggregated states. Due to the brushes being densely tethered on a surface, some of the monomers in the grafted chain are shielded from contacts with matrix monomers in the dispersed case in contrast to the number of contacts made by monomers in the free chain.

In the aggregated state, the number of contacts is further reduced and minimally different in the grafted and free case. Thus,  $\Delta U$  going from a dispersed to aggregated state is smaller for the tethered brush. The total entropy change, on the other hand, is affected by both the conformational entropy gain of matrix chains,  $\Delta S_{\text{conf}}$ , and mixing entropy loss,  $\Delta S_{\text{mix}}$ .  $\Delta S_{\text{conf}}$  going from the dispersed to aggregated case is expected to be larger for the grafted blend than free blend case due to the fact that matrix chains penetrating a densely grafted layer during dispersion will have fewer configurations than outside this layer during aggregation. In the free blend, this change in configurations is expected to be minimal.  $\Delta S_{\text{mix}}$  going from the dispersed to aggregated state is smaller for the grafted blend case since the brushes being tethered reduces the available volume for grafted and matrix polymer mixing. Hence, the much larger energetic and entropic driving forces to stay mixed in the free blend situation cause a sharper and higher dispersed-to-aggregated transition temperature than the grafted blend.

## 4.5 Conclusions

In this chapter, we looked into the phase behavior of a polymer-grafted  $\text{SiO}_2$  nanoparticle in a chemically dissimilar matrix. Particularly, the wetting-dewetting and dispersion-aggregation transitions were identified in the case of deuterated polystyrene-grafted silica nanoparticles in a poly(vinyl methyl ether) matrix—a system which is known to exhibit favorable enthalpic interactions ( $\chi < 0$ ) at low temperatures and phase separation ( $\chi > 0$ ) at high temperatures.

Using AGET ATRP, deuterated and hydrogenated polystyrene brushes of high grafting density were grown on the surface of SiO<sub>2</sub>. The hydrodynamic size and highly-ordered structure of the hybrid nanoparticles were confirmed by scattering measurements. Through a combination of x-ray and neutron scattering techniques, the dispersion of SiO<sub>2</sub>-dPS33k in a PVME226k matrix (much higher molecular weight relative to the brush) was observed. Moreover, the wetting-dewetting transition of this system was found to be a gradual and continuous process that occurs at a temperature much lower than the observed spinodal decomposition temperature (~90°C and ~143 °C, respectively). These results are in remarkable contrast to the known behavior of grafted nanoparticles in a chemically similar matrix (athermal case) where first, dispersion is normally achieved in the presence of a lower molecular weight matrix relative to the brush; and second, the wetting-dewetting and dispersion-aggregation transitions are similar or analogous events.

# Chapter 5      Brush Conformations in Nanocomposites of Polymer-Grafted Nanoparticles in a Chemically Distinct Polymer Matrix

## 5.1 Introduction

Over the last few decades, the inclusion of nanoparticles in polymer matrices has been systematically utilized to impart dramatic improvements in the functional properties of the resultant nanocomposite<sup>2,81</sup>. The outlook for precise engineering of these materials, however, demands a controlled dispersion of the nanoparticles within the polymer host<sup>21,73</sup>. To address this challenge, several strategies have been proposed for improving nanoparticle-matrix compatibility, mainly through surface functionalization of nanoparticles with polymer chains to overcome van der Waals and polymer-facilitated inter-particle interactions that are generally responsible for nanoparticle aggregation<sup>40,65,82</sup>.

Within this framework of polymer nanocomposites, significant amount of work from theoretical, simulations and experimental perspectives has been devoted to studying the interplay of surface curvature (or particle size)<sup>83</sup>, grafting density ( $\sigma$ )<sup>39</sup> and grafted chain/matrix chain ratio ( $\alpha$ )<sup>39,76</sup> in the dispersion/aggregation (wetting/dewetting) of polymer-grafted nanoparticles in a chemically similar polymer matrix. Trombly and Ganesan showed that as nanoparticles become more curved for a given  $\sigma$  and  $\alpha$ , the cost of stretching grafted chains accompanied by the penetration of free chains is reduced,

enhancing the tendency for brush wetting<sup>84</sup>. Later, Maillard et al. elucidated various structures that can be generated by tuning  $\sigma$  and  $\alpha$ , at a fixed particle diameter, for a system consisting of polystyrene (PS) grafted silica ( $\text{SiO}_2$ ) nanoparticles dispersed in a PS matrix. They concluded that in the high  $\sigma$  and  $\alpha$  limit, the nanoparticles are well dispersed in the PS matrix. However, for the same  $\sigma$ , the system begins to exhibit entropic demixing effects, or “autophobic dewetting”, when the matrix chains are much larger than the brush<sup>85</sup>. A similar behavior was reported by Goel et al. for a system of poly(*n*-butyl acrylate) (PBA)-grafted silica nanoparticles in a PBA matrix where particle aggregation was observed when the free chains were at least 3 times larger than the tethered brush<sup>41</sup>. In other words, large free chains relative to the brush are entropically expelled from the grafted corona, effectively dewetting the brush and causing the particles to aggregate. On the other hand, short enough free chains are able to penetrate and wet the brush, favoring dispersion in the matrix<sup>75</sup>.

These studies suggest that for an athermal system consisting of chemically identical brush and matrix chains and where the Flory-Huggins parameter  $\chi \approx 0$ , wetting/dewetting and dispersion/aggregation are practically analogous events primarily driven by entropic forces—the gain in mixing entropy favors the wetting of the brush and causes the system to be thermodynamically miscible; while the loss in conformational entropy from matrix penetration leads to dewetting. Achieving dispersion, in this case, necessitates the use of low molecular weight solvents or matrix chains, and therefore small filler loadings since these free chains are unable to screen long-range interactions between the

grafted brushes<sup>42,58</sup>. Previous theoretical<sup>50,59</sup> and experimental<sup>86</sup> studies have shown, however, that brush wetting and stabilization of grafted colloids can be achieved for systems of *chemically dissimilar* brush and matrix compositions. This is also true even for matrix molecular weights much larger than the grafts or for entropically unfavorable conditions. Hence, while extensive research on athermal nanocomposites has tremendously contributed to establishing “ground rules” for dispersion metrics and composites design, there is a growing realization of the limitations posed by athermal blends in designing advanced hybrid materials which motivates our work on blend systems of chemically dissimilar compositions. This can potentially encompass a larger scope of component choices (particle, brush, matrix) in grafted-nanoparticle polymer composites that offer a myriad of possibilities for material design and functionality.

In this chapter, we look into a graft polymer-matrix polymer system that undergoes a brush wetting/dewetting transition as a result of favorable interactions at low temperature ( $\chi < 0$ ) and phase separation at high temperatures ( $\chi > 0$ ). Specifically, we focus on deuterated polystyrene-grafted  $\text{SiO}_2$  nanoparticles ( $\text{SiO}_2$ -dPS) of high grafting density mixed with a chemically distinct poly(vinyl methyl ether) (PVME) matrix. As we look at the wetting-dewetting transition in this  $\text{SiO}_2$ -dPS/PVME system, we close in on the accompanying transformations in polymer brush conformation. We find that these highly-grafted nanoparticles can be treated as having two regimes as described by Ohno et al.<sup>54</sup> and Dukes et al.<sup>55</sup>: an inner region of stretched chains in the concentrated

polymer brush (CPB) regime and an outer region of more relaxed conformations in the semidilute polymer brush (SDPB) regime. We take a step forward from the work done by Hore et al.<sup>87</sup> and use complementary small angle x-ray scattering (SAXS) and small angle neutron scattering (SANS) in probing these changes in brush conformation as it goes from a “wet” to “dewetted” state.

## 5.2 Methodology

### 5.2.1 Synthesis of SiO<sub>2</sub>-dPS nanoparticles by surface-initiated AGET ATRP

Deuterated PS brushes were grown from the surface of SiO<sub>2</sub> following the same synthesis scheme as in Chapter 4.2.1. These were characterized in a similar fashion.

### 5.2.2 Preparation of SiO<sub>2</sub>-dPS/PVME nanocomposites

SiO<sub>2</sub>-dPS/PVME nanocomposites were prepared as outlined in Chapter 4.2.3. These were analyzed in a similar fashion.

## 5.3. Results and discussion

Given the strong coupling between the conformations of the polymer chains, the wetting properties of the polymer brush and the dispersion of nanoparticle in composites, a full assessment of the local particle distribution is necessary for the interpretation and analysis of brush conformations. This is particularly important in high-loading nanocomposites such as the current composite. In this work, we utilize SAXS measurements, supported by TEM, to quantify the dispersion behavior of the composite in response to increases in

temperature. The measurements were performed starting from room temperature up to  $T = 150\text{ }^{\circ}\text{C}$ , which exceeds the glass transition temperature of the brush polymer ( $T_g \approx 90\text{ }^{\circ}\text{C}$ ). Due to the very low x-ray contrast between dPS and PVME ( $9.60 \times 10^{-6}\text{ \AA}^{-2}$  and  $9.66 \times 10^{-6}\text{ \AA}^{-2}$ , respectively), the SAXS scattering signal mainly comes from the silica cores, which provides an ideal approach to studying the positional order of the nanoparticles without structural artifacts from the polymer brush or brush-matrix interactions. An example of the SAXS scattering data, at  $25\text{ }^{\circ}\text{C}$ , is shown in Figure 5.1a. Generally, the measured scattering intensity is expressed as

$$I(q) = c \cdot P(q)S(q) + BG, \quad \text{Equation 5.1}$$

where  $c$  is a scaling factor,  $BG$  is the background intensity,  $P(q)$  is the single-particle form factor defined by the particle shape and  $S(q)$  is the structure factor describing the spatial arrangement of the particles. The form factor of the bare silica nanoparticles,  $P_{\text{silica}}(q)$ , was independently obtained from SAXS measurements on a dilute suspension (i.e.  $S(q) = 1$ ) of the bare particles in methyl isobutyl ketone and is shown as a solid black line in Figure 5.1a. The form factor calculated is given by

$$P(q) = \frac{\text{scale}}{V} \left[ \frac{3V(\Delta\rho)(\sin(qr) - qr\cos(qr))}{(qr)^3} \right]^2 + BG, \quad \text{Equation 5.2}$$

where  $\text{scale}$  is the volume fraction,  $V$  is the volume of the scatterer,  $r$  is the radius of the sphere,  $\Delta\rho$  is the scattering contrast and  $bg$  is the background. Fits of

$P_{\text{silica}}(q)$  to a sphere model yields a log-normal size distribution with a mean particle radius of 6.1 nm and a polydispersity ratio of 0.297.

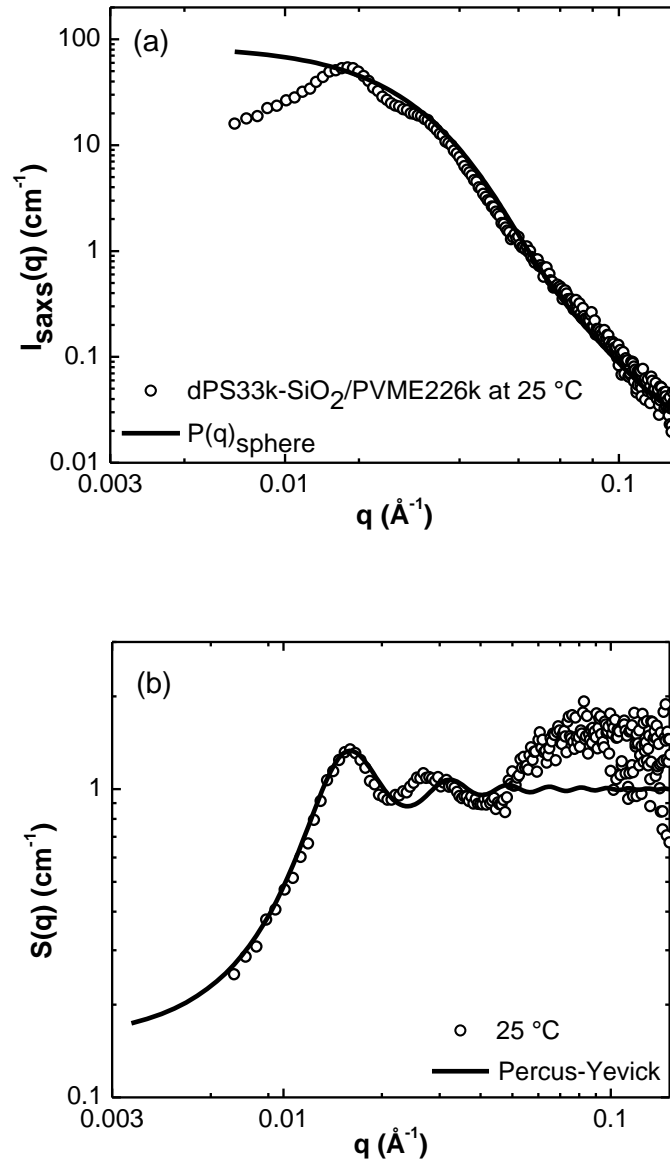


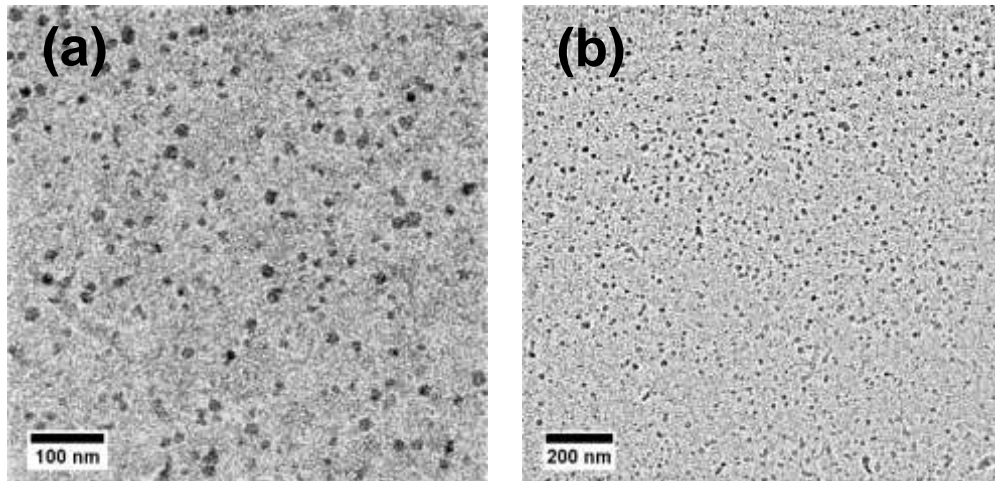
Figure 5.1 (a) SAXS profile of a SiO<sub>2</sub>-dPS33k/PVME226k blend at 25 °C. (b) Corresponding structure factor  $S(q)$ .

Given a low silica volume fraction of 0.01 in the blend, we can scale the bare-particle form factor,  $P_{\text{silica}}(q)$ , to the high  $q$  intensity of the SAXS signal on the composites as shown in Figure 5.1a and extract the structure factor,  $S(q)$ , in the composite using the following expression

$$S(q) = \frac{I_{\text{comp}}^{\text{SAXS}}(q)}{P_{\text{silica}}(q)}, \quad \text{Equation 5.3}$$

where  $I_{\text{comp}}^{\text{SAXS}}(q)$  is the intensity of the SAXS signal from the composite. An example of the obtained structure is shown in Figure 5.1b for the SAXS data set in Figure 5.1a. The fit of the  $S(q)$  pattern at 25 °C to a Percus-Yevick model (Figure 5.1b) shows reasonable agreement with the data and provide estimates for the effective radius of the particles. We attribute the deviation at high  $q$  to the polydispersity of the silica core. Also, we note that this model calculates the inter-particle structure factor for spherical particles interacting through hard spheres and excluded volume interactions<sup>88</sup>. In the case of a  $\text{SiO}_2$ -dPS33k/PVME226k blend with a  $\chi < 0$  at low temperatures, this argument holds and as such, the model is able to capture the  $S(q)$  features, especially at low  $q$ , fairly well. However, as  $\chi$  becomes more positive (at higher temperatures) and excluded volume interactions become negligible, the system starts to deviate from the model, especially at low  $q$  and must be treated carefully. Hence, while this fit can be generally informative, their quantitative use in this work is strictly limited to the processing of the SANS data in order to obtain the SANS form factors, as described later.

The wave-vector,  $q$ , of the primary scattering peak in  $S(q)$  provides an estimate of the mean inter-particle distance,  $d$ , between the centers of the silica nanoparticles according to the relation  $q = 2\pi/d$ . In the absence of the PVME matrix, the inter-particle distance is about 33.0 nm, which translates to a brush height of 10.5 nm given a silica diameter of 12.0 nm. In the presence of PVME and at room temperature, the inter-particle distance significantly increases to 41.5 nm, denoting a highly-swollen and wet brush. This is in good agreement with observations made by TEM imaging at high and low magnification showing well-dispersed, individual particles in the matrix (Figures 5.2a and 5.2b). Further, the average inter-particle distance calculated from binarized versions of these real-space images (Figure 5.3c,  $d_{TEM} = 41.0$  nm) is very closely matched with our SAXS measurements.



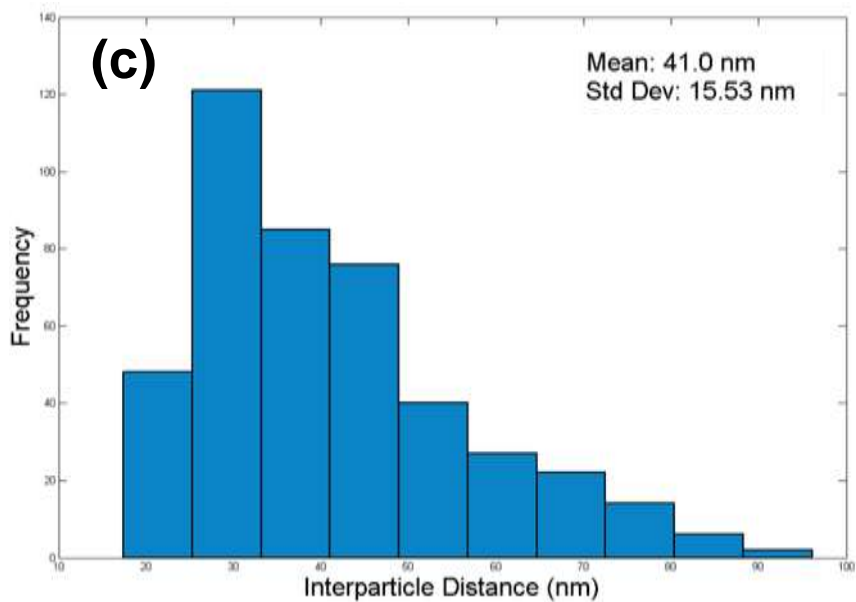


Figure 5.2 (a) high and (b) low magnification TEM images of SiO<sub>2</sub>-dPS33k/PVME226k at 25 °C; and (c) distribution of the center to center inter-particle distance (nm).

We then track the changes in  $d$  for all the temperatures considered in this work to show the gradual wetting/dewetting transition, the onset of which is marked by the dashed line in Figure 5.3. Initially, at low temperatures, the PVME completely wets the brush, in which case the particles are farthest apart. We then observe that with increasing temperatures, the inter-particle distance gradually decreases as the matrix chains are expelled from the grafted layer. This onset of dewetting denotes concentration fluctuations in the system as  $\chi$  becomes increasingly less negative and entropic interactions begin to favor segregation<sup>47,80</sup>. The concentration fluctuations are also evident in the low  $q$  SAXS intensity plot where an upturn in intensity becomes apparent as temperature is increased (Figure 4.7a).

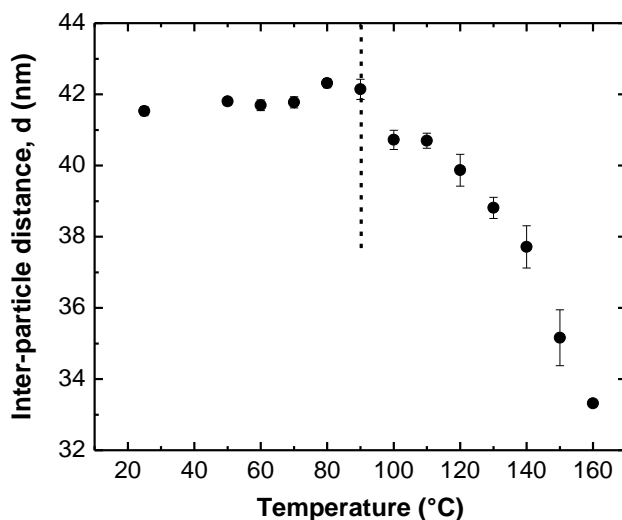


Figure 5.3 Change in SAXS inter-particle distance with temperature. The dashed line marks the onset of dewetting.

The SANS technique is most sensitive to these large scale inhomogeneities in blends and is especially useful in the case of deuterium-labeled brushes that provide excellent contrast in neutron scattering. It is therefore an excellent means of investigating the wetting behavior and thermodynamic interactions between the brush and the matrix, which in turn affect the conformation of the polymer chains. These large scale concentration fluctuations are captured in the low  $q$  coherent SANS data as presented in (Figure 4.8a).

The SANS signal at low temperatures shows a plateau at low  $q$ , indicative of finite-sized and individually-dispersed nanoparticles in the matrix. As the temperature is increased, an upturn in intensity begins to manifest, denoting particle aggregation and hence, phase separation in the system. For a binary

mixture, the scattering intensity in the forward direction ( $q=0$ ) is related to the second derivative of the Gibbs free energy density with respect to composition and is expressed as

$$S^{-1}(q=0) = \frac{1}{k_B T} \frac{\partial^2 G}{\partial \phi_1^2} = \frac{1}{n_1 \phi_1 v_1} + \frac{1}{n_2 \phi_2 v_2} - 2 \frac{\chi_{12}(T)}{v_0}, \quad \text{Equation 5.4}$$

where  $k_B$  is the Boltzmann constant,  $n_1$ ,  $\phi_1$ ,  $v_1$  are the degree of polymerization, volume fraction and specific molar volume of component 1, respectively, and  $n_2$ ,  $\phi_2$ ,  $v_2$  are those of component 2. The thermodynamics of phase separation are thus extracted from the Flory-Huggins parameter,  $\chi_{12}$ . Furthermore, the large scale concentration fluctuations take the form of inter-particle contributions that are described by the Ornstein-Zernike equation (Equation 4.3). We find that both  $1/I_{\text{SANS}}(q)$  and  $\xi$  diverge as the spinodal temperature is approached, consistent with the phase separation behavior of polymer blends and star-shaped PS/PVME mixtures (Figure 4.9a).

In the analysis of the brush behavior during the wetting-dewetting transition, we first consider the SANS form factor,  $P_{\text{SANS}}(q)$ , and eliminate contributions from inter-particle interactions by dividing the total coherent SANS intensity,  $I_{\text{SANS, Coh}}(q)$  by the obtained Percus-Yevick fits in Figure 5.1b according to the relation

$$P_{\text{SANS}}(q) = \frac{I_{\text{SANS, Coh}}(q)}{S_{\text{Percus-Yevick}}(q)}. \quad \text{Equation 5.5}$$

The resulting  $P_{\text{SANS}}(q)$  curves for select temperatures are shown in Figure 5.4.

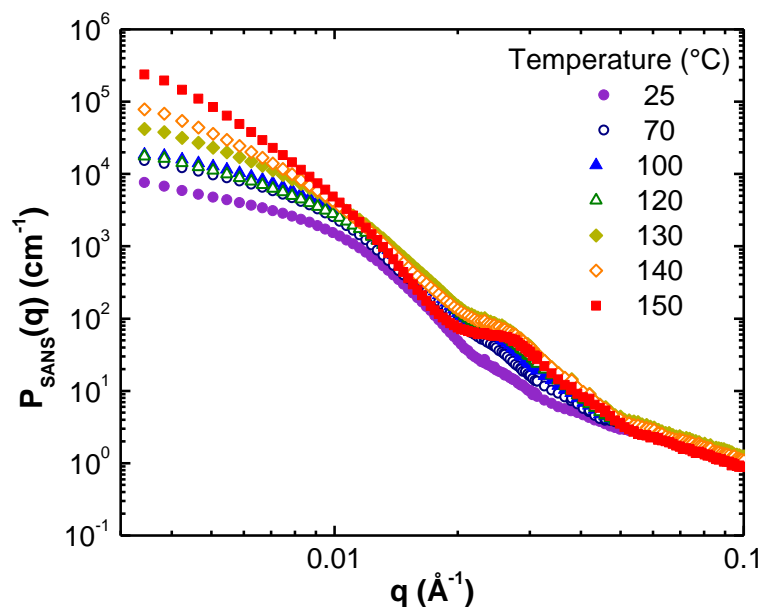


Figure 5.4 SANS form factor  $P(q)$  after division of the coherent SANS  $I(q)$  by the Percus-Yevick model.

The current analysis is based on a scheme in which the highly-grafted nanoparticles are described by a fixed core radius,  $r_{\text{core}}$ , of 60 Å, an inner region of highly-stretched chains and an outer region of flexible chains in contact with the PVME matrix. Based on back-of-the-envelope calculations of the thickness of the CPB domain, we expect the CPB domain to have major contribution to the measured form factor at intermediate  $q$  values. In this scenario, the brush, along with the silica core, are adequately described by an Onion Exponential Shell model<sup>89</sup> that takes into account radial variations in the brush SLD and provides information on the brush wetting. On the other hand, the relaxed conformations of the brush segments in the SDPB layer and their significant contrast with the matrix segments are expected to influence the high  $q$  region of  $P_{\text{SANS}}(q)$ . This behavior is akin to polymer blends, which are typically described by a Polymer

Excluded Volume model<sup>90</sup>. Examples of fits to the models are shown in Figure 5.5 for the composite at 25, 90 and 140 °C. Both models nicely capture the shape and features of the SANS form factor with the exception of very low  $q$ . We must point out that the current models do not accurately capture features in the low  $q$  regime that account for thermodynamic fluctuations in the system. However, they are sufficient to use in extracting pertinent information on the brush behavior in the mid- and high- $q$  range, which result from such concentration fluctuations. In the analysis of the  $P_{\text{SANS}}(q)$  using the onion exponential shell model, the inner shell of highly-stretched chains is assumed to have an SLD  $\text{Shell}_{\text{in}}$  that is predominantly of the dPS brush ( $6.46 \times 10^{-6} \text{ \AA}^{-2}$ ); while the outer layer has an SLD  $\text{shell}_{\text{out}}$  intermediate of dPS and PVME as a result of “wetting” and is allowed to be a fit parameter. Using the polymer excluded volume model, on the other hand, we extract the brush radius of gyration,  $R_g$ , and Porod exponent,  $m$ , which is inversely related to the excluded volume parameter,  $\nu$ . The best fit parameters for both models are summarized in Tables 5.1 and 5.2.

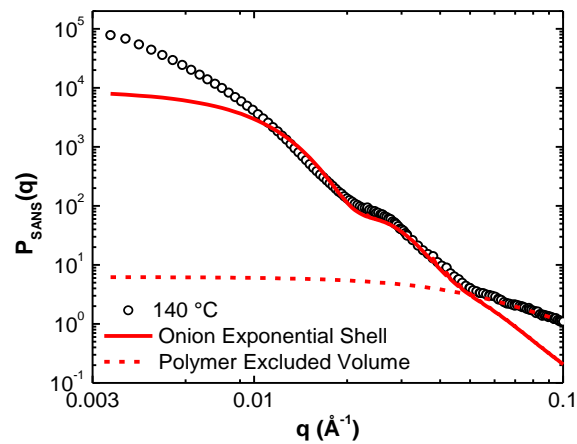
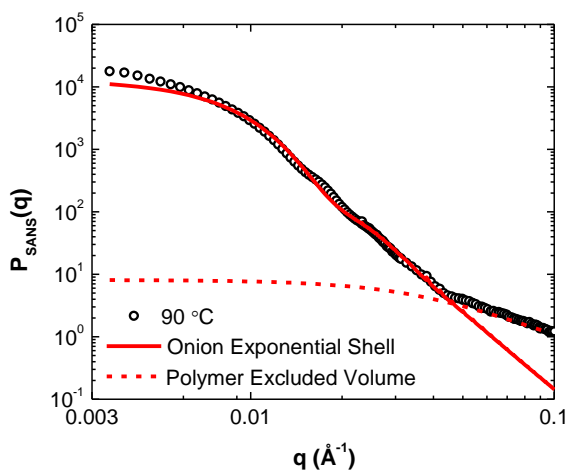
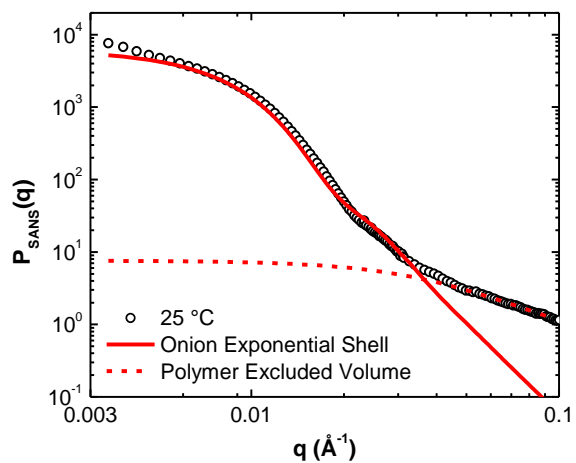


Figure 5.5 SANS  $P(q)$  fit to the onion exponential shell and polymer excluded volume models at representative temperatures (a) 25 °C, (b) 90 °C, (c) 140 °C.

Table 5.1 Best fit parameters using the onion exponential shell model.

Temp (°C)	Shell Thickness (Å)	error (Å)	Shell SLD (out, $\times 10^{-6} \text{ \AA}^{-2}$ )	error ( $\times 10^{-8} \text{ \AA}^{-2}$ )
25	139.25	0.13	4.93	6.71
50	138.32	0.16	4.94	1.74
60	138.69	0.03	4.94	1.73
70	138.48	0.29	4.98	1.78
80	138.29	0.10	5.11	0.18
90	137.00	0.10	5.38	0.59
100	135.81	0.21	5.52	0.17
110	135.08	0.09	5.86	0.66
120	133.87	0.15	5.94	1.65
125	132.41	0.08	6.05	0.41
130	131.86	0.19	6.03	2.18
135	130.86	0.15	6.13	0.66
140	128.90	0.17	6.32	2.80
150	129.13	0.21	6.32	2.24

Table 5.2 Best fit parameters using the polymer excluded volume model.

Temp (°C)	Porod exponent, m	error	Excluded volume parameter, $\nu$ (1/m)	error	Radius of gyration, $R_g$ (Å)	error
25	1.68	0.01	0.60	0.00	41.50	0.62
50	1.70	0.00	0.59	0.00	41.87	0.33
60	1.70	0.00	0.59	0.00	42.00	0.05
70	1.72	0.00	0.58	0.00	42.00	0.04
80	1.72	0.02	0.58	0.01	42.00	0.12
90	1.77	0.01	0.57	0.00	41.53	0.06
100	1.85	0.01	0.54	0.00	41.00	0.11
110	1.95	0.00	0.51	0.00	40.00	0.03
120	2.12	0.04	0.47	0.01	38.00	0.08
125	2.05	0.02	0.49	0.00	34.00	0.11
130	2.03	0.00	0.49	0.00	32.00	0.05
135	2.00	0.01	0.50	0.00	33.00	0.14
140	2.08	0.01	0.48	0.00	32.46	0.07
150	2.10	0.01	0.48	0.00	33.60	0.07

A careful treatment of the data reveals a clear-cut picture of the brush conformations occurring across the entire temperature range under study as the brush transitions from a “wet” to “dewetted” state. In Figure 5.6a, the shell thickness considered to be the surface-to-surface distance from the core is at its maximum (139 Å) at room temperature where the particles are expected to be in the “wet” state and are thus, well-dispersed in the matrix. This is found to decrease gradually with temperature and is consistent with the change in inter-particle distance from SAXS measurements (Figure 5.3). The shell thicknesses obtained across the entire temperature range are well within the upper and lower bounds measured from DLS and SAXS experiments, respectively. We attribute this change in shell thickness to the steady expulsion of the matrix chains which begins to take place at ~90 °C. The resulting outer shell SLD at low temperatures has values intermediate of the matrix chain SLD ( $3.53 \times 10^{-7} \text{ \AA}^{-2}$ ) and dPS ( $6.47 \times 10^{-6} \text{ \AA}^{-2}$ ) as expected during matrix penetration. At room temperature, for instance, the computed SLD of the outer shell from the fit is  $4.93 \times 10^{-6} \text{ \AA}^{-2}$ . As the matrix chains dewet the brush, the outer shell SLD transitions to an SLD for a dense brush of pure dPS collapsing onto the surface above 120 °C, signaling the onset of aggregation. The SLD at 150 °C when the brushes are fully collapsed in the aggregated state is  $6.32 \times 10^{-6} \text{ \AA}^{-2}$ .

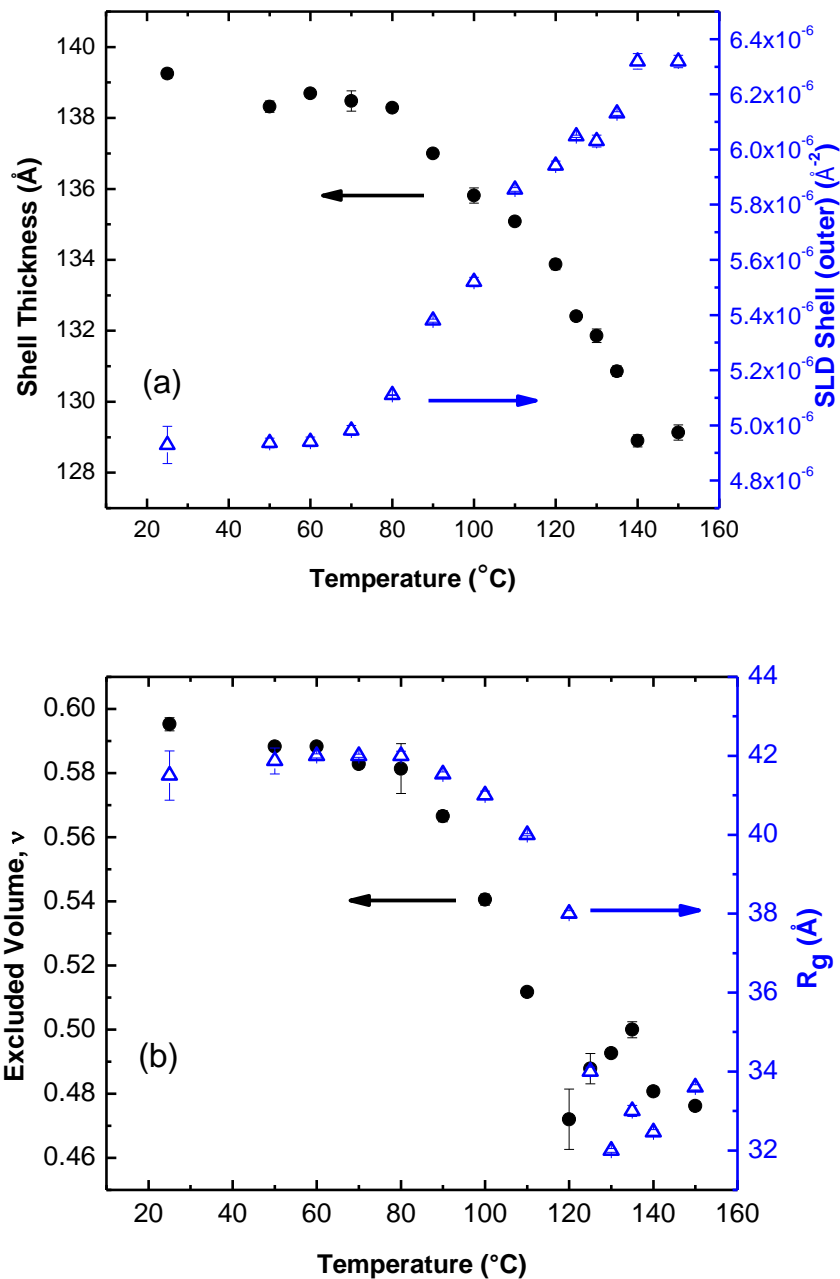


Figure 5.6 Resulting trends from the (a) onion exponential shell and (b) polymer excluded volume model fits.

The changes in brush conformation occurring during this transition are also represented by the calculated  $\nu$  and  $R_g$ , of the grafted polymer chain (Figure 5.6b). At low temperatures where wetting is expected to occur, the grafted

brushes are found to have an excluded volume parameter  $\nu \approx 0.6$  characteristic of a swollen chain<sup>54,91,92</sup>. The measured  $R_g$ , in such case, is at a maximum ( $\approx 42$  Å) since brush-matrix contacts are optimal. With increasing temperature, however, the grafted chains begin to adopt a more ideal, Gaussian-like conformation, with  $\nu$  gradually decreasing to  $\approx 0.5$  and  $R_g$  reducing to  $\approx 38$  Å. The matrix chains become akin to a theta solvent, inducing more intra-chain contacts between the brushes. As the system is driven towards an entropically more favorable demixed state at higher temperatures, excluded volume effects become negligible and a further decrease in  $R_g$  observed.

## 5.4 Conclusions

Through a detailed treatment of both SAXS and SANS measurements, we have shown that there is a gradual wetting/dewetting transition that occurs for a highly-grafted nanoparticle in a chemically distinct and high molecular weight matrix. The favorable enthalpic interactions between the brush and the matrix facilitate nanoparticle dispersion at low temperatures; while unfavorable entropic interactions at high temperatures drive phase separation. More importantly, we elucidate the brush conformational evolution occurring as a result of this wetting/dewetting transition through an intensive analysis of the SANS form factor. A combination of the onion exponential shell and polymer excluded volume models allowed the direct estimation of the changes in the brush thickness and brush SLD which are linked to this wetting/dewetting transition. These conformational changes are also reflected in the gradual transition from a

swollen chain having an excluded volume parameter  $\nu \approx 0.6$  and  $R_g$  of  $\approx 42 \text{ \AA}$  at low temperatures, to a Gaussian-like behavior with  $\nu \approx 0.5$  and  $R_g$  of  $\approx 38 \text{ \AA}$  at higher temperatures.

# Chapter 6 Coil-to-Globule Transition of Polymer-Grafted Nanoparticles in a Theta Solvent

## 6.1 Introduction

The phase transition of polymers in solution gives rise to different chain conformations that depend on both the nature of the polymer and quality of the solvent.<sup>93</sup> These changes can be triggered by varying the temperature, giving rise to so-called ‘thermoreponsive polymers’ which play a crucial role in a wide range of applications such as drug delivery, tissue engineering and coatings<sup>94,95</sup>, among others. The temperature-dependent behavior of polymers in a theta solvent is driven by favorable and unfavorable thermodynamic interactions within the system according to the mean field theory of Flory and Huggins.<sup>96,97</sup> Such behavior was first observed and described as a coil-to-globule transition by Swislow et al.<sup>98</sup> for a single polystyrene chain in cyclohexane at very low concentrations. Above the theta temperature ( $T_{\theta} \approx 35$  °C), chain-solvent interactions predominate, causing the chains to be more extended. At  $T_{\theta}$ , chain-chain and chain-solvent interactions cancel out, allowing the chains to behave more ideally. Below  $T_{\theta}$ , intrachain interactions are stronger, leading to chain collapse and aggregation. The evolution of a polymer chain for such system exhibiting an upper critical solution temperature (UCST) behavior has been studied over a wide temperature range through photon correlation spectroscopy by measuring the hydrodynamic radius and indirectly, the radius of gyration.<sup>93,98</sup>

Later, these studies were extended to the case of grafted brushes akin to star polymers<sup>99</sup> where thermodynamic behavior dictates the stability of colloidal systems as shown from experiments<sup>100–103</sup> and simulations.<sup>104–107</sup> Kaiser and Schmidt<sup>108</sup> identified a volume transition behavior of polystyrene-coated iron oxide nanoparticles that is distinct from a phase transition behavior. Dynamic light scattering (DLS) measurements allowed the observation of a coil-to-globule transition around the theta temperature irrespective of brush molecular weight and concentration, accounting for volume changes within the brush. On the other hand, the critical temperature,  $T_c$ , at which the phase separation behavior occurred, increased with increasing molar masses and concentrations. The internal radial structure that contributes to volume change and phase behavior in the case of crosslinked poly(*N*-isopropylacrylamide) bound to a polystyrene core was investigated by Seelenmeyer and co-workers<sup>109</sup> using small angle x-ray scattering (SAXS), small angle neutron scattering (SANS) and DLS. These techniques allowed a comparative study of the changing network thickness and provided a quantitative analysis of the swelling and collapsing of a core-shell system.<sup>110</sup>

In this work, we investigate the conformational transition of polystyrene-grafted silica nanoparticles in a cyclohexane solvent under dilute conditions. Through hydrodynamic radius measurements, we first identify a gradual transition in the vicinity of  $T_\theta$  that is distinct from the phase separation temperature,  $T_c$ . We then complement these dynamic measurements by looking more closely into the static properties of the brush, particularly its structural

behavior. Through SANS, we directly probe changes in single chain dimensions such as brush thickness, scattering length density (SLD) and radius of gyration,  $R_g$ , over a wide temperature range.

## 6.2 Methodology

### 6.2.1 Synthesis of polystyrene-grafted silica nanoparticles by AGET ATRP

In a round bottom flask, 20 mL of styrene was combined with 47.36 mg of Cu(II)Br and 173.36 mg of dNBpy. In another flask, 500 mg of initiator-grafted SiO<sub>2</sub> nanoparticles (synthesized as described in Chapter 3.1.1) and 61.76  $\mu$ L of Sn(EH)<sub>2</sub> were dissolved in 80 mL of toluene. Both flasks were purged with N<sub>2</sub> for at least 30 minutes and combined using a cannula. The solution mixture was placed in an oil bath at 90 °C and the reaction was allowed to proceed for 18-41 hr.

After polymerization, the reaction mixture was exposed to air and diluted with THF. It was then passed through a column of neutral aluminum oxide twice to ensure the removal of catalyst. The excess THF and toluene were removed by rotavap and the remaining viscous liquid was added dropwise to a large excess of cold MeOH to yield white solid precipitates. The polymer-grafted nanoparticles were recovered by centrifugation and washed twice more by redissolving in THF and precipitating in MeOH.

### 6.2.2 Preparation of polystyrene-grafted silica nanoparticle suspensions for DLS

A dilute solution of polystyrene-grafted SiO<sub>2</sub> nanoparticles in cyclohexane was prepared by dissolving 5.1 mg of the solid in 17 mL of cyclohexane (0.3

mg/mL  $\approx$  0.029 v%). The solution was allowed to stir at 50 °C overnight to ensure complete dissolution, sonicated at the same temperature for 10 min and filtered through a 0.2  $\mu$ m filter. Prior to measurements, the sample was allowed to equilibrate at 50 °C for  $\sim$ 30 min.

### 6.2.3 Preparation of polystyrene-grafted silica nanoparticle suspensions for SANS

A 0.25 v% concentration of the polymer-grafted SiO<sub>2</sub> nanoparticles in deuterated cyclohexane (d-cyclohexane) was prepared by dissolving 2.09 mg of the solid in 1.09 g of d-cyclohexane. An equivalent concentration of the polymer-grafted nanoparticles in deuterated toluene (d-toluene) was made by dissolving 1.90 mg of the solid in 0.93 g of d-toluene. The samples were stirred at 50 °C for at least 24 hr to ensure complete dissolution. The samples were loaded and secured in demountable banjo sample cells available at NCNR. The sample cells were then placed in a sample holder with a temperature-controlled fluid circulation system.

## 6.3 Results and discussion

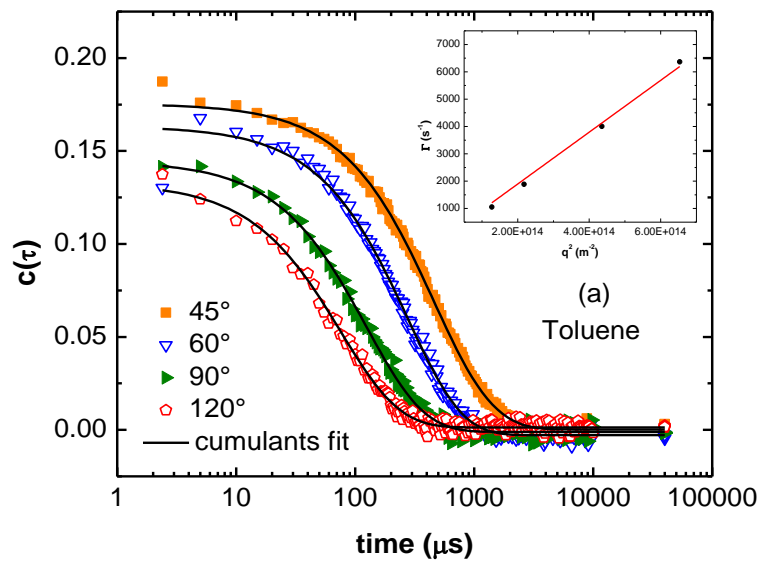
Size exclusion chromatography measurements on the cleaved polymer brush gave an estimate of the polymer molecular weight and polydispersity index (PDI). In addition, thermo-gravimetric analysis of the hybrid nanoparticles allowed the determination of the residual weight loss due to the polymer brush and to the grafted initiator used to calculate for the polymer grafting density (Equation 3.1). SAXS measurements on annealed hybrid nanoparticles gave the inter-particle

distance,  $d$ , in the bulk (no solvent), and consequently allowed the calculation of the brush height given by  $h = (d-d_0)/2$  where  $d_0$  is the diameter of the core (12 nm). A summary of the characteristics of the hybrid nanoparticles included in this work is presented in Table 6.1.

Table 6.1 Characteristics of the synthesized hybrid nanoparticles.

Sample	Molecular weight (g/mol)	PDI	Polymer grafting density (chain/nm <sup>2</sup> )	Brush height, $h$ (nm)
SiO <sub>2</sub> -PS67k	67,000	1.3	0.2	8.7
SiO <sub>2</sub> -PS43k	43,000	1.2	0.2	5.4

The stability of the suspensions was first verified through DLS measurements. An example of the correlation plots for the SiO<sub>2</sub>-PS67k sample is shown in Figure 6.1.



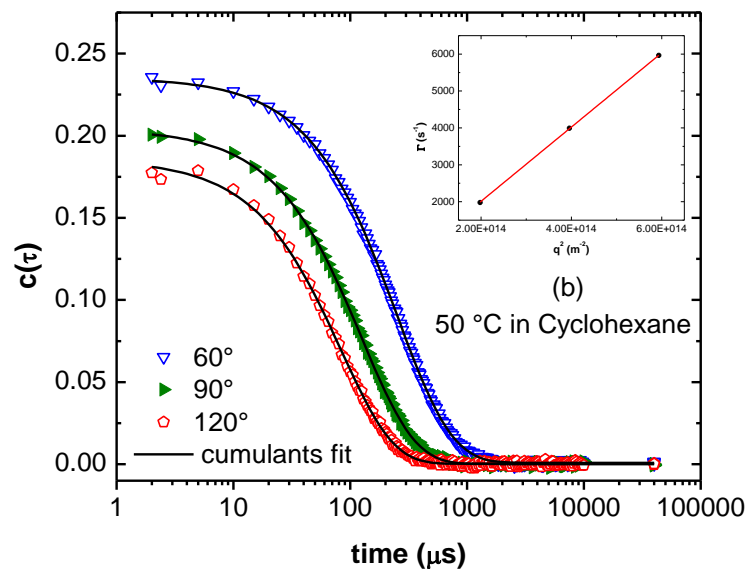


Figure 6.1 Correlation plots for SiO<sub>2</sub>-PS67k in (a) toluene and (b) cyclohexane at 50 °C; the solid black line denotes the cumulants fit.

The resulting data show a single exponential decay profile for the grafted particles in toluene and in cyclohexane at 50 °C, characteristic of monodisperse particles in solution. We note that under these conditions, the PS-grafted nanoparticles are expected to be well-dispersed in solution since toluene is a good athermal solvent for PS, while cyclohexane is a good solvent above the  $\theta$ -temperature ( $\sim 35$  °C). In Figure 6.2, we also present the autocorrelation function of the intensity of the scattered light,  $g^{(2)}(\tau)$ , at a scattering angle of 90° and at select temperatures to show no significant change in the diffusivity and number of scatterers below a critical temperature. This will be further elaborated on in the following discussion.

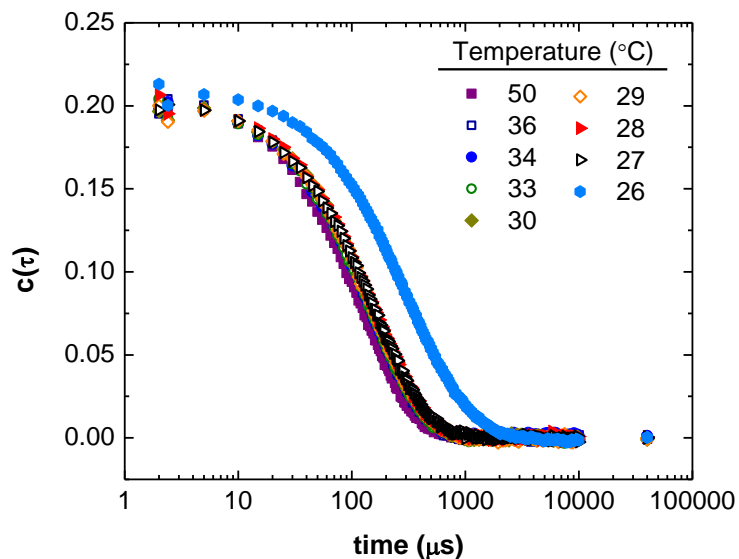


Figure 6.2 Correlation plot at a scattering angle of 90° at select temperatures.

The decay rate described by the correlation function is given by  $\Gamma = D_{\text{coeff}}q^2$ , which can be directly obtained from a cumulants fit. Here,  $D_{\text{coeff}}$  is the diffusion coefficient and  $q$  is the magnitude of the scattering wavevector. A linear extrapolation of the resulting  $\Gamma$  vs.  $q^2$  plot gives the  $D_{\text{coeff}}$  which can be applied in the Stokes-Einstein relation (Equation 6.1) to obtain the hydrodynamic radius,  $R_h$ . Table 6.2 provides a summary of the obtained results from the fits to the DLS measurements.

$$R_h = \frac{k_B T}{6\pi\eta D_{\text{coeff}}} . \quad \text{Equation 6.1}$$

Table 6.2 Hydrodynamic radius of SiO<sub>2</sub>-PS67k in good solvents.

Solvent	$\eta$ (Pa·s)	$R_h$ (nm)
Toluene (at 25 °C)	$5.54 \times 10^{-4}$	$42.4 \pm 0.2$
Cyclohexane (at 50 °C)	$6.07 \times 10^{-4}$	$38.8 \pm 0.2$

As cyclohexane is a known  $\theta$  solvent for PS, its ability to solvate the grafted PS brush changes with temperature. At the  $\theta$ -temperature,  $\chi = 1/2$  and polymer-polymer self-interactions (poor solvent) exactly cancel out excluded volume expansion effects (good solvent), characteristic of brushes behaving ideally. As temperature is lowered further, the solvent quality decreases which leads to brush collapse and possible aggregation. Through temperature-controlled DLS measurements, we examine this transition for a dilute  $\theta$ -solution (0.029 v%) of hybrid nanoparticles, well below the overlap concentration ( $\varphi_{\theta}^*$ ) for a  $\theta$ -solvent given by  $\varphi_{\theta}^* \approx N^{-1/2}$ , where  $N$  is the degree of polymerization. In the case of SiO<sub>2</sub>-PS67k,  $\varphi_{\theta}^* \approx 3.9$  v%. The temperature dependence of the resulting apparent  $R_h$  calculated from a scattering angle of 90° is presented in Figure 6.3.

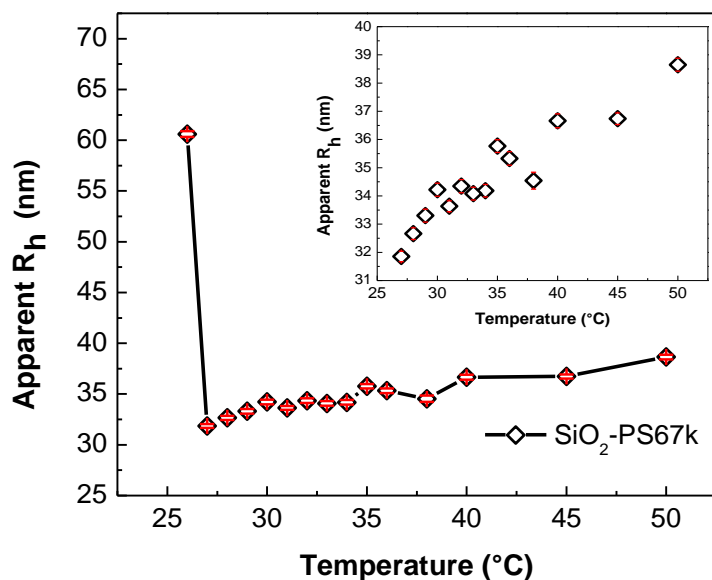


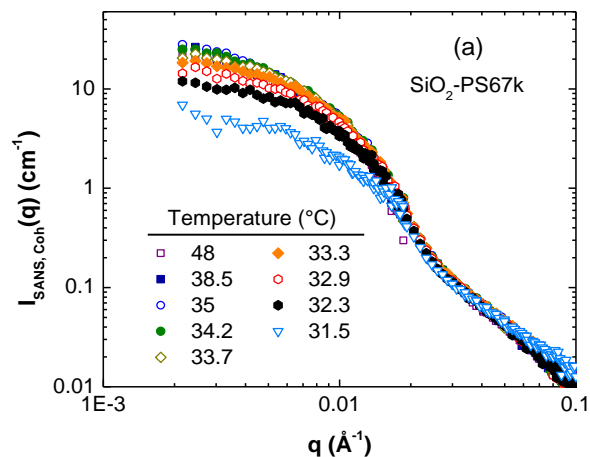
Figure 6.3 Temperature dependence of the hydrodynamic radius of SiO<sub>2</sub>-PS67k hybrid nanoparticles in cyclohexane. The inset shows an expanded view of the transition prior to aggregation at 26 °C.

The extended coil configuration of the end-tethered nanoparticles is observed at the highest temperature where cyclohexane is a good solvent for PS. This results in effective repulsive forces among the grafted chains which contribute to nanoparticle stabilization.<sup>111</sup> For SiO<sub>2</sub>-PS67k, the apparent hydrodynamic radius at 50 °C is ~39 nm. As temperature is lowered, this gradually decreases which implies a transition to the globule state at 27 °C with a radius of ~32 nm. At a critical temperature, T<sub>c</sub>, of 26 °C, the phase separation temperature is reached, signified by a sudden and substantial increase in the size of scatterers due to aggregation. This also translates to slower moving particles reflected by a shift in the g<sup>(2)</sup>(τ) plot (Figure 6.2). Hence, while the evolution from a swollen to collapsed brush appears to be a gradual transition, the phase change from a dispersed to aggregated state is more sharp and discrete. These observations are consistent with an earlier report on the dimensional change of a high molecular weight linear polystyrene occurring near the theta temperature<sup>112</sup>. Further, Swislow et al.<sup>98</sup> reported a similar temperature dependence of R<sub>h</sub> for all the concentrations considered and showed a rather continuous coil-to-globule transition at ~32 °C. More recently, Kaiser and Schmidt<sup>108</sup> reported two different transitions for PS core-shell particles in a cyclohexane solvent, namely, a volume transition of the particle shell near the θ-temperature and particle aggregation-induced phase separation below T<sub>c</sub>.

We complement these dynamic measurements with an investigation of the static properties of the particle, particularly the structural conformation of the grafted brush as it crosses over the θ-temperature and approaches T<sub>c</sub>. We

employ the SANS technique and take advantage of obtaining good contrast from using a deuterated solvent. Because the wavelength used in this technique is a good match to the size of even low molecular polymers, it becomes sensitive to changes in single chain dimensions such as the brush thickness and radius of gyration,  $R_g$ .<sup>113</sup>

The coherent SANS scattering intensity of two systems (at 0.025 v%) at select temperatures is presented in Figure 6.4a and Figure 6.4b. Any large scale concentration fluctuations due to particle aggregation would readily be apparent in the low  $q$  scattering behavior. It can be observed, however, that the intensity profile throughout the probed temperature window remains that of a homogenous dispersion of spherical nanoparticles with no obvious low- $q$  power-law dependence. Moreover, in the high- $q$  regime, the intensities superimpose nicely without any significant change in the signal. This clearly indicates two things: first, the volume of scatterers is not changing with temperature and second, the changes in the intensity signal at low  $q$  is a result of the deuterated solvent activity as it interacts with the brush.



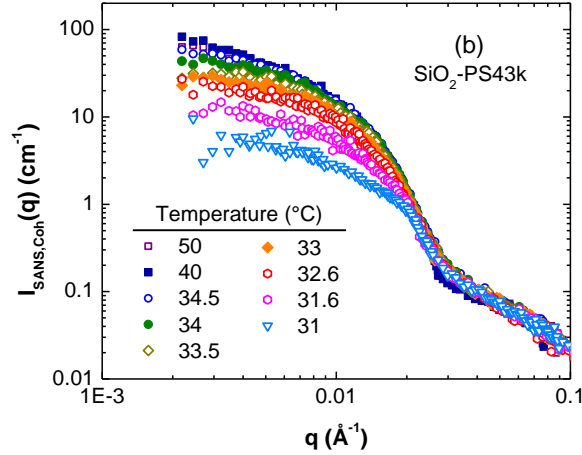


Figure 6.4 Temperature dependence of the SANS scattering intensity for (a) SiO<sub>2</sub>-PS67k and (b) SiO<sub>2</sub>-PS43k nanoparticles in d-cyclohexane.

Scattering techniques such as SANS readily allow the extraction of structural information from such core-shell type of systems mainly due to the difference in scattering length densities of the brush and the surrounding solvent which, in this case, are  $1.41 \times 10^{-6} \text{ \AA}^{-2}$  and  $6.67 \times 10^{-6} \text{ \AA}^{-2}$ , respectively. We therefore employ a core-shell model<sup>114,115</sup> in the  $I_{\text{SANS, Coh}}(q)$  analysis to directly measure and observe the change in shell thickness as the solvent quality changes. This model is described by the form,

$$P(q) = \frac{\text{scale}}{V_s} \left[ 3V_c(\rho_c - \rho_s) \frac{[\sin(qr_c) - qr_c \cos(qr_c)]}{(qr_c)^3} + 3V_s(\rho_s - \rho_{\text{solv}}) \frac{[\sin(qr_s) - qr_s \cos(qr_s)]}{(qr_s)^3} \right] + \text{bkg} \quad \text{Equation 6.2}$$

where *scale* is a scale factor,  $V_s$  is the volume of the outer shell,  $V_c$  is the volume of the core,  $r_s$  is the radius of the shell,  $r_c$  is the radius of the core,  $\rho_c$  is the scattering length density of the core,  $\rho_s$  is the scattering length density of the

shell,  $\rho_{solv}$  is the scattering length density of the solvent, and  $bkg$  is the background.

Several previous reports dealing with neutron scattering from core-shell colloidal systems found that the high  $q$  behavior is largely dominated by static intensity from fluctuations of the polymer shell network<sup>109,110,116</sup>. This deviation from a core-shell model is captured by a Lorentzian function,  $I_{fluc}(0)/1+(q\xi)^2$ , which we also adopt in our analysis. We note that as shown in Figure 6.5, a core shell model alone fails to describe  $I_{SANS}(q)$  especially at high  $q$ . Fits to a closely-related structure of a fuzzy sphere<sup>117</sup> do not show good agreement with the data either (Figure 6.6).

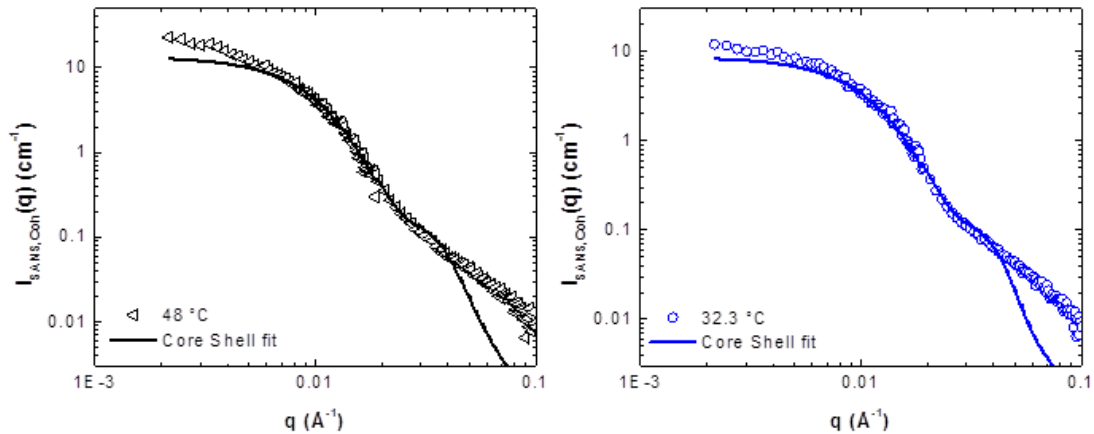


Figure 6.5 Fits to a core shell model at select temperatures.

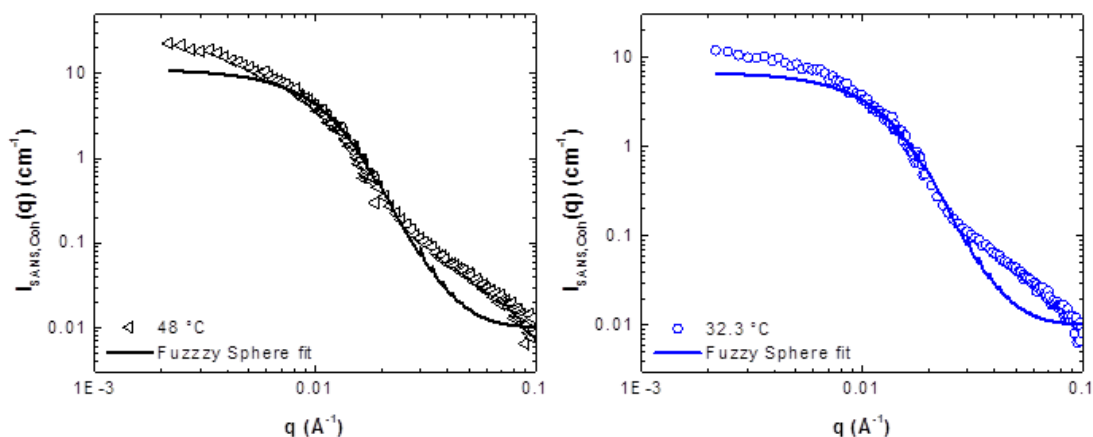


Figure 6.6 Fits to a fuzzy sphere model at select temperatures.

On the other hand, Figure 6.7 shows that a core shell Lorentz model can be reasonably applied to the SANS data for hybrid nanoparticles in the good solvent case. We observe no change in the scattering profile at high and low temperatures for particles dispersed in toluene.

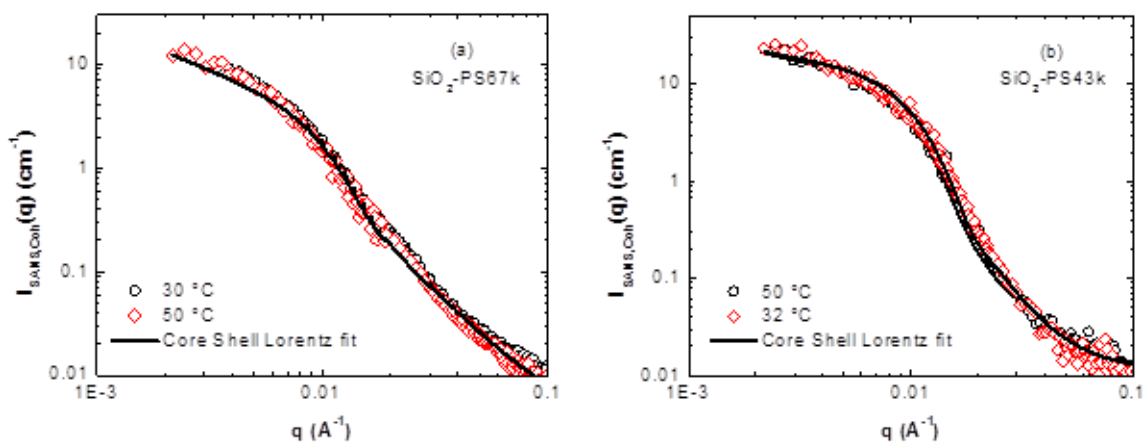


Figure 6.7 Fits to a core-shell Lorentz model for (a) SiO<sub>2</sub>-PS67k and (b) SiO<sub>2</sub>-PS43k in toluene.

We then apply this model to the cyclohexane system resulting in the following fits to the  $I_{\text{SANS,coh}}(q)$  above and below the  $\theta$ -temperature (Figure 6.8). The shell thickness and shell SLD are allowed to be fit parameters, while the core radius is kept constant at 60 Å.

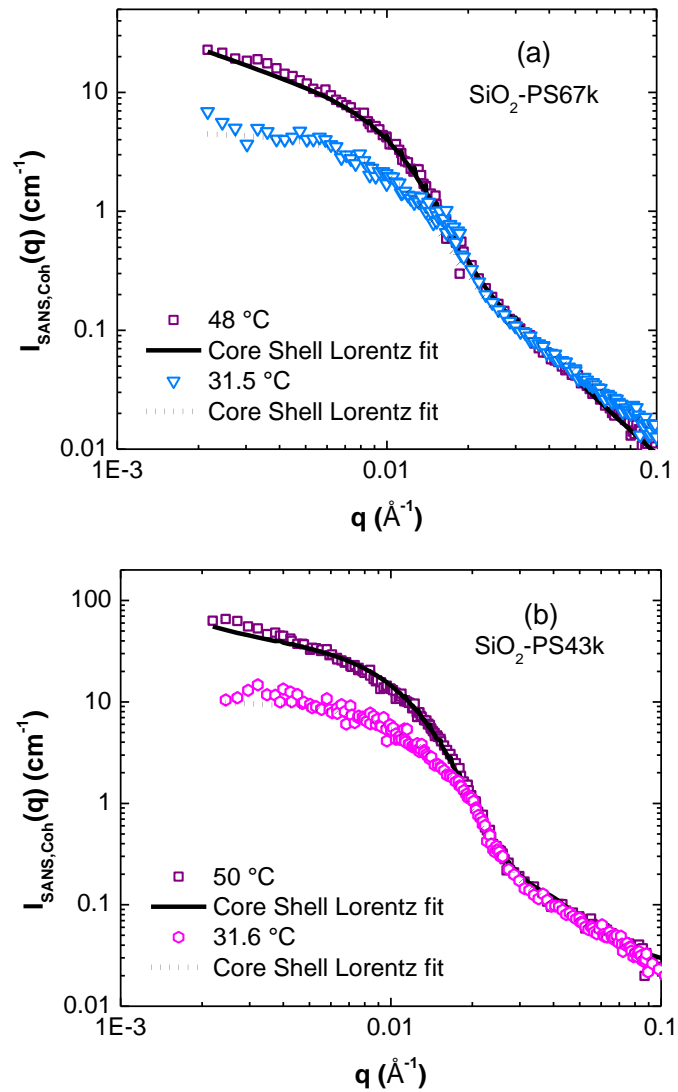


Figure 6.8 Fits to a core-shell Lorentz model for (a)  $\text{SiO}_2$ -PS67k and (b)  $\text{SiO}_2$ -PS43k in cyclohexane.

The best fit parameters obtained at select temperatures depict a distinct trend consistent with a coil-to-globule transition (Figure 6.9a). Fits at other select temperatures are also shown in Figures 6.10 and 6.11. At high temperatures and above the  $\theta$ -temperature, chain-solvent as well as repulsive intrachain interactions dominate. Aside from excluded volume effects which depict a self-avoiding random walk of the polymer chains,<sup>118</sup> the solvent molecules easily surround and swell the brush, causing them to stretch<sup>108</sup>. It is therefore also expected that the shell SLD between 36 °C-50°C ( $\sim 5.5 \times 10^{-6} \text{ \AA}^{-2}$ ) (Figure 6.9b) would have a larger contribution from the deuterated solvent (SLD of d-cyclohexane =  $6.67 \times 10^{-6} \text{ \AA}^{-2}$ ). As the  $\theta$ -temperature is approached, the brush thickness gradually decreases as the polymer chains assume a more ideal behavior. In this case, there is a corresponding decrease in shell SLD that accounts for a decrease in the volume of solvent molecules within the corona. Finally, below the  $\theta$ -temperature, interactions between segments of a polymer chain dominate, causing it to collapse into a globule state. This is signaled by a noticeable decrease in shell thickness below 35 °C that coincides with a reduction in SLD ( $\sim 4.0 \times 10^{-6} \text{ \AA}^{-2}$ ) which approaches values close to that of pure PS ( $1.41 \times 10^{-6} \text{ \AA}^{-2}$ ) as the solvent molecules are expelled from the shell. At the same time, the complete collapse and aggregation of nanoparticles are prevented by the steric repulsion of the chain segments.<sup>119</sup>

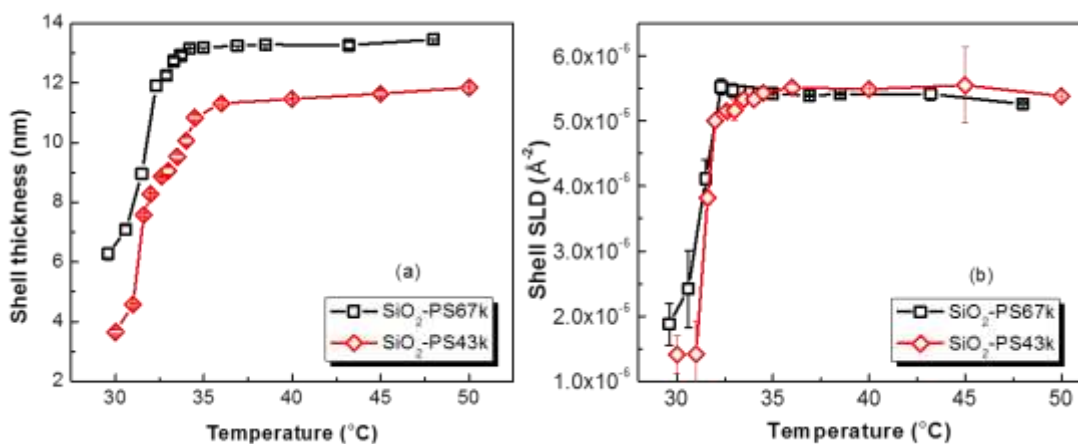


Figure 6.9 (a) Change in shell thickness with temperature and (b) corresponding change in SLD.

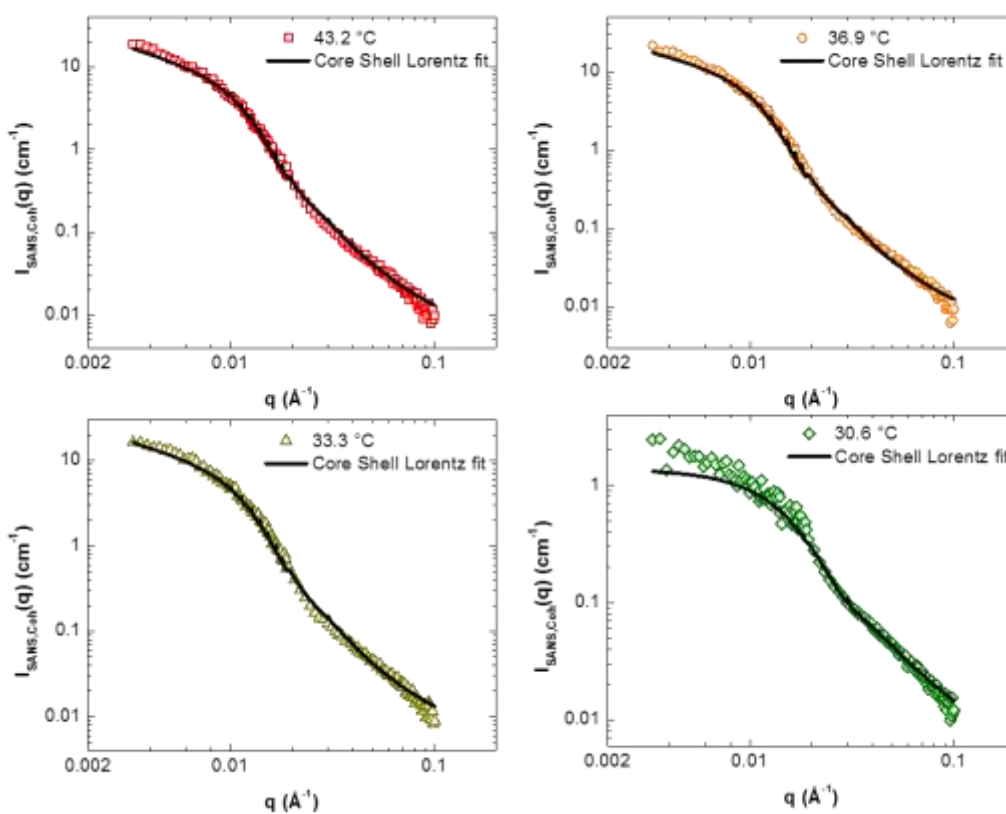


Figure 6.10 Fits to a core-shell Lorentz model for SiO<sub>2</sub>-PS67k at select temperatures.

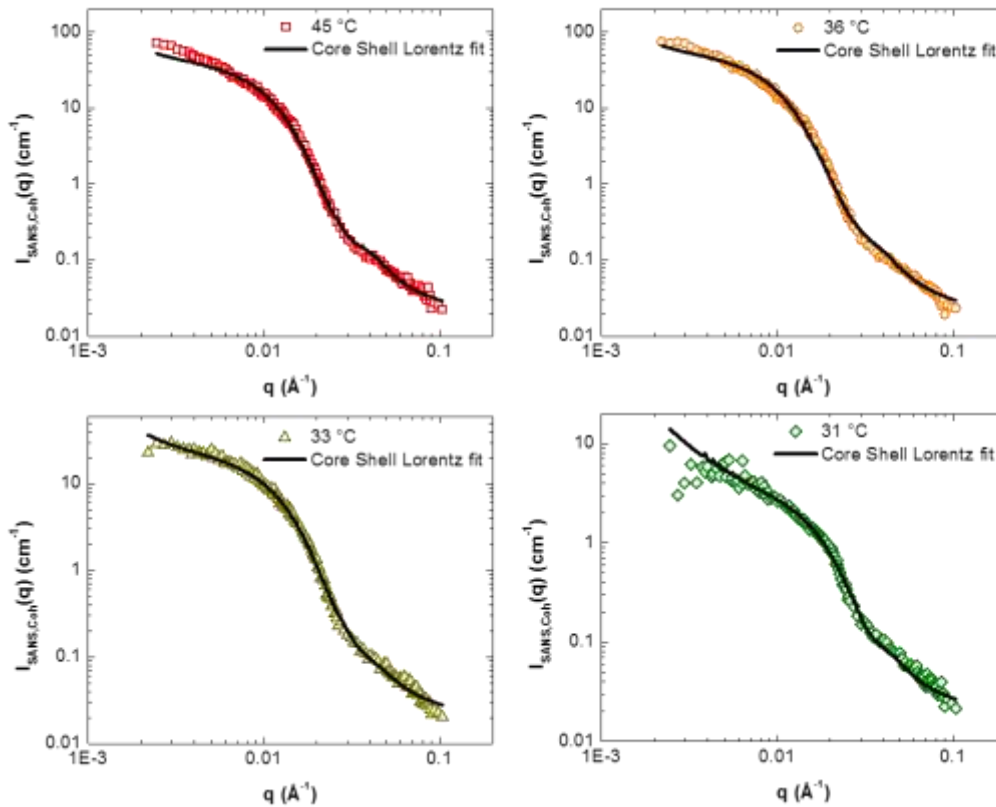


Figure 6.11 Fits to a core-shell Lorentz model for SiO<sub>2</sub>-PS43k at select temperatures.

We note that the shell thickness from DLS,  $d_{DLS}$ , which can simply be calculated from  $R_h$  as  $d_{DLS} = R_h - R_0$ , where  $R_0$  is the radius of the core (6 nm), exhibits the same temperature dependence as the shell thickness from SANS fits. However, SANS is more sensitive to concentration fluctuations and volume fraction changes in the scattering material; while  $R_h$  is easily influenced by both solvent and shape effects. Hence, the thickness obtained from DLS is expected to be considerably larger than that derived from SANS.<sup>109</sup>

The Lorentzian form of the low-angle scattering intensity from SANS is given by the Ornstein-Zernike equation (Equation 6.3),

$$I_{\text{SANS, Coh}}(q) = \frac{I(0)}{1 + \xi^2 q^2} . \quad \text{Equation 6.3}$$

Figure 6.12 presents the resulting Zimm plots for SiO<sub>2</sub>-PS67k and SiO<sub>2</sub>-PS43k, both showing distinct behaviors above and below T<sub>θ</sub>. On the top row, we observe a very minimal change in 1/I<sub>SANS,Coh</sub>(q) in the case where the systems are at high temperatures (Figures 6.12a and 6.12b), suggesting optimal interactions between the solvent and individually dispersed nanoparticles. On the other hand, as temperature is lowered below T<sub>θ</sub>, significant changes in intensity start to manifest (Figure 6.12c and 6.12d). Particularly, I<sub>SANS,Coh</sub>(q) decreases with decreasing temperature (hence, 1/I<sub>SANS,Coh</sub>(q) increases) for both systems as the volume of solvent molecules within the brush is diminished and as intrachain interactions take over. The scattering at zero angle, 1/I(Q=0), is plotted as a function of temperature to show more clearly these two regions of temperature-dependent scattering intensity below T<sub>θ</sub> (Figure 6.13a) and a nearly monotonic behavior above T<sub>θ</sub> (Figure 6.13b).

Since the scattering at very low q is largely dominated by scattering from spherical particles, the intensity can be expressed as<sup>120</sup>

$$I_{\text{SANS}}(Q) = \left(\frac{N}{V}\right) \Delta\rho^2 V_P^2 F^2(QR) , \quad \text{Equation 6.4}$$

where  $\left(\frac{N}{V}\right)$  is the spheres number,  $\Delta\rho^2$  is the contrast factor,  $V_P$  is the sphere volume and  $F(QR)$  is the single-sphere form factor amplitude. We can then

consider the volume of the sphere to have the largest contribution to the change in intensity.

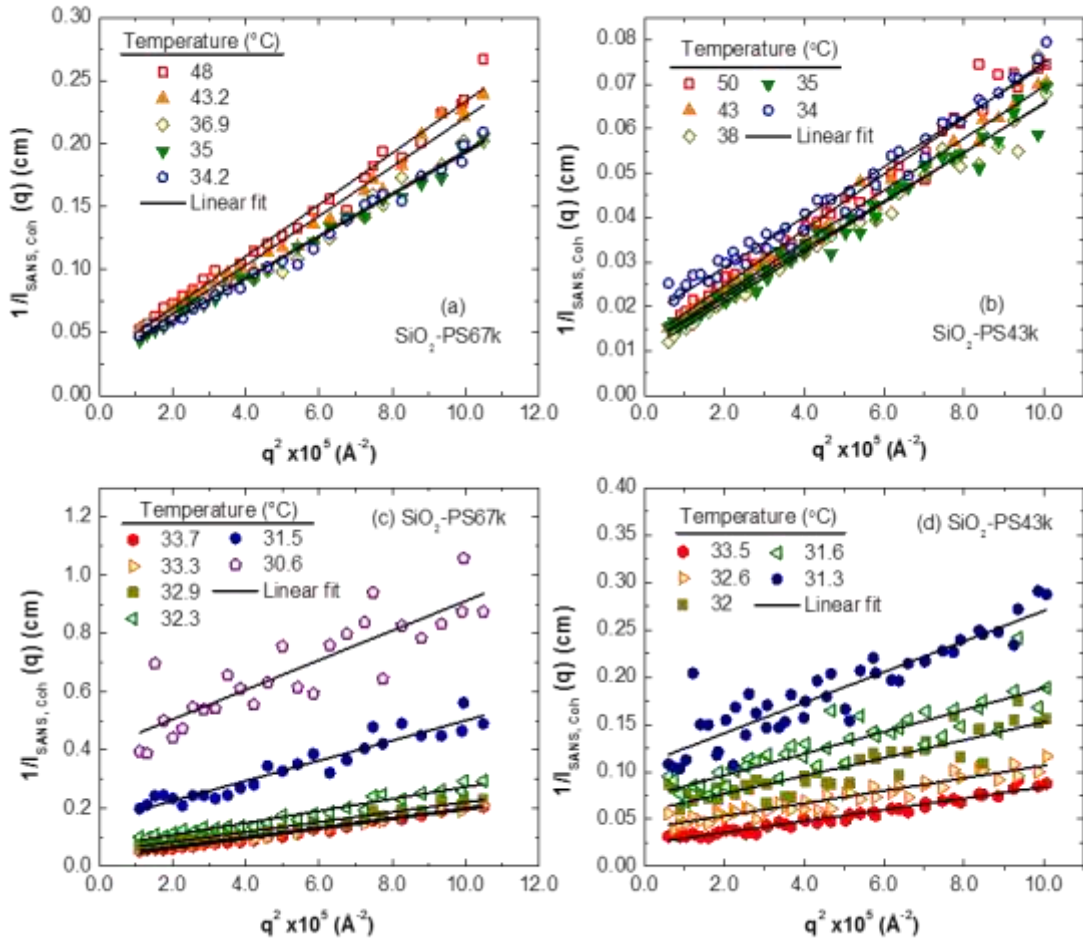


Figure 6.12  $1/I_{\text{SANS,coh}}(q)$  vs.  $q^2$  at high temperatures (top row) and low temperatures (bottom row) for SiO<sub>2</sub>-PS67k and SiO<sub>2</sub>-PS43k.

At high temperatures and above the  $\theta$ -temperature, there is no significant change in intensity as particles remain individually dispersed in the solvent. As the system transitions from a good solvent at high temperatures to a bad solvent at low temperatures, however, the sphere volume (considered to be

the entire system of core and polymer brush) decreases, consistent with changes in the brush thickness. This change in sphere volume is also accompanied by the escape of solvent molecules from the polymer chains. As such,  $I_{\text{SANS}}(Q)$  decreases with decreasing temperatures, consistent with the observed trends in Figure 6.12 and Figure 6.13.

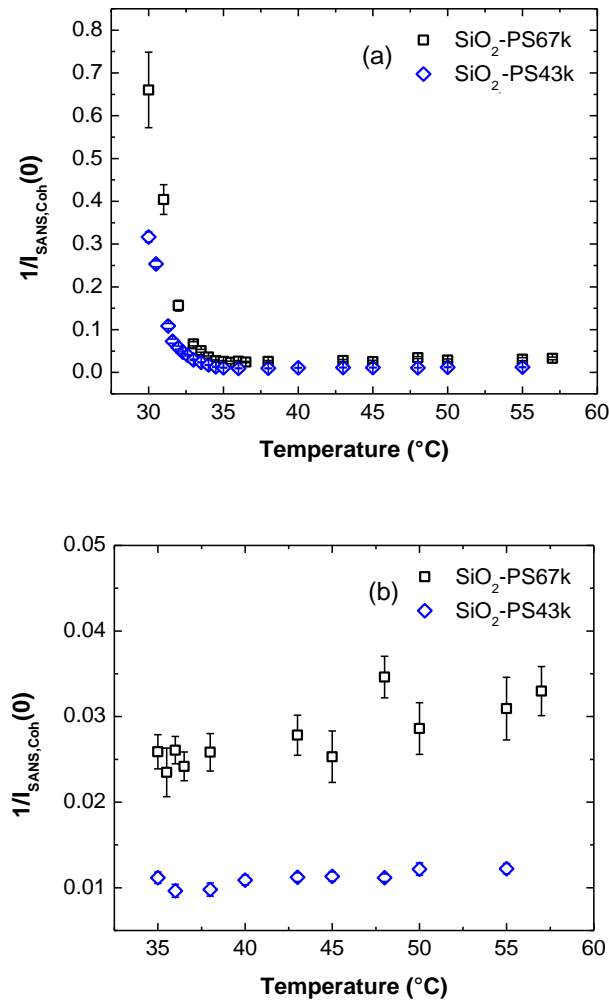


Figure 6.13  $1/I_{\text{SANS,coh}}(0)$  as a function of temperature (a) across the entire temperature range and (b) above the  $\theta$ -temperature.

We also estimate the radius of gyration,  $R_g$ , or the effective size of the scattering particle from the SANS scattering intensity in the low- $q$  Guinier region. The Zimm plots in Figure 6.12 allow the determination of the correlation length,  $\xi$ , which at low  $q$  is related to  $R_g$  according to the relation,  $\xi = R_g/\sqrt{3}$ . Note that  $\xi$  is simply the square root of the ratio of the slope to the intercept of the aforementioned plots. The resulting values for  $R_g$  across the entire temperature range are shown in Figure 6.14.

Not surprisingly, the temperature dependence of  $R_g$  reveals the same trend in structural conformation. Polymer brushes are swollen at high temperatures due to favorable polymer-solvent interactions until the  $\theta$ -temperature is reached. Below this, the brush starts to collapse and the nanoparticles adopt a globule-like conformation. For instance, at 31.5 °C for SiO<sub>2</sub>-PS67k, the ratio of  $R_g/R_h$  is 0.75 ( $\pm$  0.04) which closely agrees with the ratio for a solid isotropic sphere given by  $(3/5)^{0.5} \approx 0.77$ , suggesting that the nanoparticles have contracted to a compact form.<sup>93</sup>

It is also worth noting that the radii obtained from hydrodynamic measurements at high temperatures are smaller than those derived from SANS. This is mainly due to the fact that the correlation function from DLS is a result of scattering from the internal motion of the polymer chains and will thus give lower values of the apparent  $R_h$ .<sup>93</sup> From the critical temperature identified from DLS measurements (26 °C), it can be reasonably assumed that below the temperature considered for SANS experiments, a discontinuity in the measured  $R_g$  will occur as a result of particle aggregation and hence, phase separation.

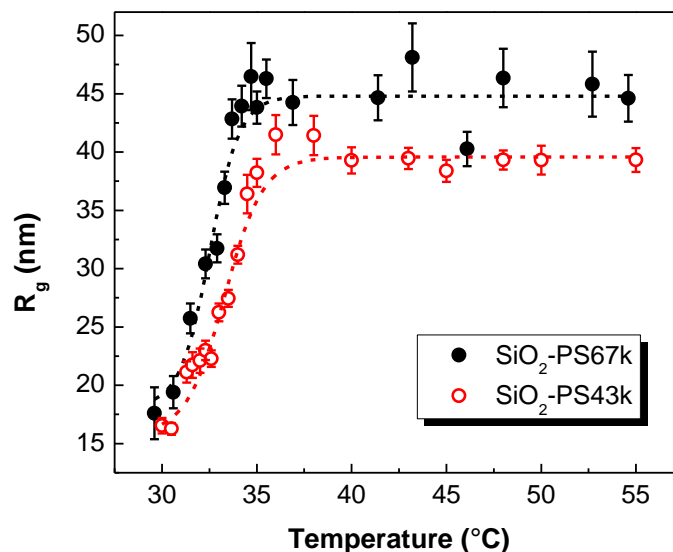


Figure 6.14 Change in  $R_g$  with temperature (dashed lines serve as guide to the eye).

## 6.4 Conclusions

Polymer chains in solution adopt various conformations that strongly depend on solvent quality. In this work, we directly probe these structural changes for a dilute solution of polystyrene-grafted  $\text{SiO}_2$  nanoparticles in a cyclohexane theta solvent. Light and neutron scattering techniques revealed a gradual coil-to-globule transition as the polymer brush evolves from being highly swollen at high temperatures to being collapsed below the theta temperature. This transition was evidenced by changes in  $R_h$  from DLS measurements, as well as changes in the single chain dimensions namely, brush thickness and SLD, from a core-shell model. At a critical temperature of 26 °C, particle aggregation signaled by a discrete and abrupt increase in  $R_h$  signified a discrete phase separation transition.

## Chapter 7 Summary and Future Work

### 7.1 Summary

Fully utilizing the remarkable effects of incorporating nanoparticles in a polymer matrix primarily requires their controlled distribution in the material. Over the last few decades or so, the ability to manipulate and design the architecture as well as the resulting properties of macromolecules has been exploited in an effort to address this issue. Specifically, nanoparticles of various shapes and sizes are grafted with polymer chains in order to improve their compatibility with the matrix material. While this technique has certainly proved successful in many accounts, continued research efforts focus on providing a fundamental understanding of the interactions that govern polymer blending as well as the dispersion of nanoparticles in solution.

Polystyrene-grafted silica nanoparticles (SiO<sub>2</sub>-PS) were synthesized using the AGET ATRP technique. This allowed control over the polymer molecular weight with low polydispersities and high grafting densities well within the “brush regime”. Composites of SiO<sub>2</sub>-PS in poly(vinyl methyl ether) (PVME) at the critical compositions (20/80) were prepared by a simple solution mixing procedure. This system is particularly interesting because of its known LCST behavior. At low temperatures, when  $\chi < 0$ , the system is in a single phase region and the components are completely miscible. At high temperatures, on the other hand,  $\chi > 0$  and the components phase separate.

Through a combination of SAXS and SANS techniques, we showed that SiO<sub>2</sub>-PS nanoparticles have favorable entropic and enthalpic interactions with a high molecular weight PVME matrix at low temperatures. Such interactions result in the matrix chains “wetting” the grafted brush and dispersing the nanoparticles. A good dispersion of the nanoparticles was evidenced by a significant increase in the inter-particle distance in SAXS relative to the pure hybrid nanoparticle (no matrix) and confirmed through TEM imaging. In SANS, a plateau at low  $q$  was observed, characteristic of spherical core-shell nanoparticles. These results are contrary to what is usually observed for athermal systems where dispersion can only be achieved if the molecular weight of the tethered brush is comparable or larger than that of the matrix chain.

Moreover, we unraveled the gradual wetting-dewetting transition that takes place as temperature is increased or as interactions become unfavorable. In SAXS, the inter-particle distance decreases in a continuous fashion with temperature which strongly suggests that matrix chains are also gradually dewetting the brush. The increase in low  $q$  intensity in both SAXS and SANS indicated increasing contributions from large scale concentration fluctuations, characteristic of phase separation. Another significant finding in this part of our work is that this wetting-dewetting transition occurs below and distinctly from the dispersion-aggregation transition. Again, this is contrary to the behavior of athermal systems where wetting-dewetting and dispersion-aggregation events are considered analogous. The spinodal temperature for our system was estimated to be at 143 °C.

We also took advantage of the large contrast between the deuterated brush and matrix to close in on the conformations assumed by the grafted chains as it undergoes a wetting-dewetting transition. We divided the  $I_{\text{SANS,CoH}}(q)$  by the  $S_{\text{SAXS}}(q)$  fit to a Percus-Yevick model to obtain the form factor  $P(q)$ . The resulting  $P_{\text{SANS}}(q)$  at each temperature was fit to an onion exponential shell model which describes radial variations in the outer shell SLD and provides information on brush thickness. On the other hand, the relaxed conformations of the brush segments in contact with PVME and their contrast with the matrix segments influence the high  $q$  region of  $P_{\text{SANS}}(q)$  and are adequately described by a polymer excluded volume model. The best fit parameters confirmed a gradual decrease in the brush thickness accompanied by an increase in the outer shell SLD as temperature is increased or as the system transitions from a “wet” to “dewetted” state. Furthermore, the excluded volume parameter decreased from  $\nu = 0.6$  at low temperatures, characteristic of polymers in a good solvent, to  $\nu = 0.5$  for polymers in a theta solvent. Not surprisingly, the obtained  $R_g$  values also decreased with temperature.

The last part of this work investigated the phase transition of  $\text{SiO}_2$ -PS nanoparticles in a cyclohexane theta solvent. In contrast to the blend system,  $\text{SiO}_2$ -PS in cyclohexane exhibits a UCST behavior. At high temperatures above the  $\theta$ -temperature (34 °C), the hybrid nanoparticles are completely soluble in the solvent. At low temperatures, they phase separate. Through DLS and SANS, we probed a coil-to-globule transition adopted by the grafted chains as the solvent quality changes. Measurements of the hydrodynamic size revealed a continuous

decrease from 50 °C to 27 °C, implying that the chains are initially in a highly-swollen state and gradually transition to a globule-like configuration. At a critical temperature of 26 °C, a sharp and discrete increase in  $R_h$  signaled the aggregation of the nanoparticles. These observations were consistent with the results from  $I_{\text{SANS, Coh}}(q)$  fits to a core shell Lorentz model which looks at single chain conformations in solution. The brush thickness and  $R_g$  were found to be optimal at high temperatures when polymer-solvent interactions are most favorable. Below the  $\theta$ -temperature, both began to gradually decrease as the chains collapse and adopt a globule conformation.

## 7.2 Future work

Understanding the phase behavior of polymer grafted nanoparticles in a polymer matrix and in solution is an ongoing research effort. Although possible mechanisms for the wetting-dewetting and dispersion-aggregation transitions have been proposed, important questions about the molecular origin of composite properties remain unanswered which can drive future investigations. For instance, it would be interesting to look at the slow local particle dynamics of the grafted core through x-ray photon correlation spectroscopy (XPCS) measurements. Similarly as in SAXS, the dominant x-ray contrast is between the silica core and the polymer, and so it is only sensitive to the dynamics of the particles. By probing wave-vector regimes that encompass the known form factor of silica, the characteristic time it takes for the particle to diffuse such length scales can be determined. In other words, by looking at the time dependence of

the scattered intensity at a certain wavevector, it is possible to quantify the dynamics of systems in or out of equilibrium. As an example, Akcora et al.<sup>121</sup> performed XPCS measurements on PS-grafted silica nanoparticles in a PS matrix and found that a system consisting of percolating sheets of particles exhibit more “gel-like” or solid-like mechanical behavior at lower particle loadings relative to that with individually dispersed particles. It is of interest to see if such behavior would be observed for a system consisting of dissimilar graft-matrix chemistries, and would certainly add relevance to the current work.

In this regard, it is also equally appropriate to study the motion and coherent dynamics of the grafted chains, possibly through neutron spin echo (NSE) measurements. The NSE technique measures the time decay of the structures that define the structure factor  $S(q)$  and has proven relevant in elucidating, for instance, polymer confinement in polymer nanocomposites.<sup>122</sup> In the case of a grafted deuterated polymer brush, as in our system, NSE can selectively measure its dynamics over large length scales and long time scales whether in dilute solutions or in melts. Obtaining such information at different temperatures where the interaction of the brush with the surrounding solvent or polymer matrix chain changes would be critical to appreciating a rather complex polymer system.

We have also limited this work to spherical silica nanoparticles of fixed size decorated with polystyrene chains and blend systems at the critical composition. It would be a step forward to examine  $\text{SiO}_2$ -PS/PVME blends at other compositions to define a phase diagram for such chemically dissimilar

grafted systems; and also explore other types of inorganic materials that impart unique properties (for instance, magnetic nanoparticles). The techniques utilized in this work and the results acquired from them show the potential for far-reaching types of brush-matrix systems that can further advance the field of materials engineering.

## References

- (1) Payne, A. R. *J. Appl. Polym. Sci.* 1962, 6 (19), 57–63.
- (2) Balazs, A. C.; Emrick, T.; Russell, T. P. *Science* 2006, 314 (5802), 1107–1110.
- (3) Crespy, D.; Bozonnet, M.; Meier, M. *Angew. Chem. Int. Ed. Engl.* 2008, 47 (18), 3322–3328.
- (4) Hule, R. A.; Pochan, D. J. *MRS Bull.* 2007, 32 (April), 354–358.
- (5) Danilchenko, S. N. *J. Biol. Phys. Chem.* 2009, 9 (3), 119–126.
- (6) Sariciftci, N. S.; Smilowitz, L.; Heeger, A. J.; Wudl, F. *Science* 1992, 258, 1474–1476.
- (7) Huynh, W. U.; Dittmer, J. J.; Alivisatos, A. P. *Science* 2002, 295, 2425–2427.
- (8) Holder, E.; Tessler, N.; Rogach, A. L. *J. Mater. Chem.* 2008, 18 (10), 1064.
- (9) Soutis, C. *Mater. Sci. Eng. A* 2005, 412, 171–176.
- (10) Heffernan, P. J.; Erki, M. A. *J. Compos. Constr.* 2004, 8 (2), 132–140.
- (11) Hore, M. J. A.; Composto, R. J. *Macromolecules* 2012, 45 (15), 6078–6086.
- (12) Hore, M. J. A.; Composto, R. J. *Macromolecules* 2014, 47, 875–887.
- (13) Kim, H.; Abdala, A. a.; Macosko, C. W. *Macromolecules* 2010, 43 (16), 6515–6530.
- (14) Pandey, Y. N.; Papakonstantopoulos, G. J.; Doxastakis, M. *Macromolecules* 2013, 46 (13), 5097–5106.
- (15) Mackay, M. E.; Tuteja, A.; Duxbury, P. M.; Hawker, C. J.; Van Horn, B.; Guan, Z.; Chen, G.; Krishnan, R. S. *Science* 2006, 311 (5768), 1740–1743.
- (16) *Dekker Encyclopedia of Nanoscience and Nanotechnology*; 2007.
- (17) Tambasco, M.; Lipson, J. E. G.; Higgins, J. S. *Macromolecules* 2006, 39 (14), 4860–4868.

- (18) Roy, D.; Brooks, W. L.; Sumerlin, B. S. *Chem Soc Rev* 2013, 42, 7214–7243.
- (19) Zhang, L.; Chan, J. M.; Gu, F. X.; Rhee, J.; Wang, A. Z.; Radovic-Moreno, A. F.; Alexis, F.; Langer, R.; Farokhzad, O. C. *ACS Nano* 2008, 2 (8), 1696–1702.
- (20) Ditto, A. J.; Reho, J. J.; Shah, K. N.; Smolen, J. A.; Holda, J. H.; Ramirez, R. J.; Yun, Y. H. *Mol. Pharm.* 2013, 10, 1836–1844.
- (21) Krishnamoorti, R. *MRS Bull.* 2007, 32 (04), 341–347.
- (22) Fernandes, N. J.; Akbarzadeh, J.; Peterlik, H.; Giannelis, E. P. *ACS Nano* 2013, 7 (2), 1265–1271.
- (23) Ranjan, R.; Brittain, W. J. *Macromolecules* 2007, 40 (17), 6217–6223.
- (24) Li, J.; Wang, L.; Benicewicz, B. C. *Langmuir* 2013, 29 (37), 11547–11553.
- (25) Pyun, J.; Matyjaszewski, K. *Chem. Mater.* 2001, 13 (10), 3436–3448.
- (26) Hiemenz, P. C.; Lodge, T. P. *Polymer Chemistry, Second Edition*; Taylor & Francis, 2007; pp 142–143.
- (27) Chiefari, J.; Chong, Y. K. B.; Ercole, F.; Krstina, J.; Jeffery, J.; Le, T. P. T.; Mayadunne, R. T. A.; Meijs, G. F.; Moad, C. L.; Moad, G.; Rizzardo, E.; Thang, S. H. *Macromolecules* 1998, 31 (16), 5559–5562.
- (28) Chong, B. Y. K.; Le, T. P. T.; Moad, G.; Rizzardo, E.; Thang, S. H. *Macromolecules* 1999, 32 (6), 2071–2074.
- (29) Baum, M.; Brittain, W. J. *Macromolecules* 2002, 35 (3), 610–615.
- (30) Liu, C.-H.; Pan, C.-Y. *Polymer (Guildf)*. 2007, 48 (13), 3679–3685.
- (31) Matyjaszewski, K.; Patten, T. E.; Xia, J. *J. Am. Chem. Soc.* 1997, 119 (4), 674–680.
- (32) Fischer, H. *J. Am. Chem. Soc.* 1986, 108 (14), 3925–3927.
- (33) Tang, W.; Kwak, Y.; Braunecker, W.; Tsarevsky, N. V; Coote, M. L.; Matyjaszewski, K. *J. Am. Chem. Soc.* 2008, 130 (32), 10702–10713.
- (34) Huang, J.; Tang, C.; Lee, H.; Kowalewski, T.; Matyjaszewski, K. *Macromol. Chem. Phys.* 2007, 208 (21), 2312–2320.

- (35) Kang, C.; Crockett, R. M.; Spencer, N. D. *Macromolecules* 2014, *47* (1), 269–275.
- (36) Ohno, K.; Koh, K.; Tsujii, Y.; Fukuda, T. *Macromolecules* 2002, *35* (24), 8989–8993.
- (37) Von Werne, T.; Patten, T. E. *J. Am. Chem. Soc.* 1999, *121* (32), 7409–7410.
- (38) Von Werne, T.; Patten, T. E. *J. Am. Chem. Soc.* 2001, *123* (31), 7497–7505.
- (39) Akcora, P.; Liu, H.; Kumar, S. K.; Moll, J.; Li, Y.; Benicewicz, B. C.; Schadler, L. S.; Acehan, D.; Panagiotopoulos, A. Z.; Pryamitsyn, V.; Ganesan, V.; Ilavsky, J.; Thiyagarajan, P.; Colby, R. H.; Douglas, J. F. *Nat. Mater.* 2009, *8* (4), 354–359.
- (40) Kumar, S. K.; Jouault, N.; Benicewicz, B.; Neely, T. *Macromolecules* 2013, *46* (9), 3199–3214.
- (41) Goel, V.; Pietrasik, J.; Dong, H.; Sharma, J.; Matyjaszewski, K.; Krishnamoorti, R. *Macromolecules* 2011, *44* (20), 8129–8135.
- (42) Jayaraman, A.; Schweizer, K. S. *Macromolecules* 2009, *42* (21), 8423–8434.
- (43) Ganesan, V.; Jayaraman, A. *Soft Matter* 2014, *10* (1), 13–38.
- (44) Maillard, D.; Kumar, S. K.; Fragneaud, B.; Kysar, J. W.; Rungta, A.; Benicewicz, B. C.; Deng, H.; Brinson, L. C.; Douglas, J. F. *Nano Lett.* 2012, *12* (8), 3909–3914.
- (45) Alexander, S. *J. Phys.* 1977, *38* (8), 983–987.
- (46) De Gennes, P. G. *Macromolecules* 1980, *13* (5), 1069–1075.
- (47) De Gennes, P. G. *J. Chem. Phys.* 1980, *72* (9), 4756–4763.
- (48) Rubinstein, M.; Colby, R. H. *Polymer Physics*; 2003; p xi, 440 p.
- (49) Zhulina, E. B.; Borisov, O. V.; Brombacher, L. *Macromolecules* 1991, *24* (16), 4679–4690.
- (50) Borukhov, I.; Leibler, L. *Macromolecules* 2002, *35* (13), 5171–5182.

- (51) Aubouy, M.; Fredrickson, G. H.; Pincus, P.; Raphael, E. *Macromolecules* 1995, 28 (8), 2979–2981.
- (52) Daoud, M.; Cotton, J. P. *J. Phys.* 1982, 43 (3), 531–538.
- (53) Zimm, B. H.; Stockmayer, W. H. *J. Chem. Phys.* 1949, 17 (12), 1301–1314.
- (54) Ohno, K.; Morinaga, T.; Takeno, S.; Tsujii, Y.; Fukuda, T. *Macromolecules* 2007, 40 (25), 9143–9150.
- (55) Dukes, D.; Li, Y.; Lewis, S.; Benicewicz, B.; Schadler, L.; Kumar, S. K. *Macromolecules* 2010, 43 (3), 1564–1570.
- (56) Wijmans, C. M.; Zhulina, E. B. *Macromolecules* 1993, 26 (26), 7214–7224.
- (57) Savin, D. a.; Pyun, J.; Patterson, G. D.; Kowalewski, T.; Matyjaszewski, K. *J. Polym. Sci. Part B Polym. Phys.* 2002, 40 (23), 2667–2676.
- (58) Brown, H. R.; Char, K.; Deline, V. R. *Macromolecules* 1990, 23 (13), 3383–3385.
- (59) Borukhov, I.; Leibler, L. *Phys. Rev. E* 2000, 62 (1), 41–44.
- (60) Han, C. C.; Bauer, B. J.; Clark, J. C.; Muroga, Y.; Matsushita, Y.; Okada, M.; Tran-cong, Q.; Chang, T.; Sanchez, I. C. *Polymer (Guildf)*. 1988, 29 (11), 2002–2014.
- (61) Xia, T.; Huang, Y.; Jiang, X.; Lv, Y.; Yang, Q.; Li, G. *Macromolecules* 2013, 46 (20), 8323–8333.
- (62) Schwahn, D.; Mortensen, K.; Springer, T.; Yee-Madeira, H.; Thomas, R. *J. Chem. Phys.* 1987, 87 (10), 6078–6087.
- (63) Balsara, N. P.; Fetters, L. J.; Hadjichristidis, N.; Lohse, D. J.; Han, C. C.; Graessley, W. W.; Krishnamoorti, R. *Macromolecules* 1992, 25 (23), 6137–6147.
- (64) Ponnappati, R.; Karazincir, O.; Dao, E.; Ng, R.; Mohanty, K. K.; Krishnamoorti, R. *Ind. Eng. Chem. Res.* 2011, 50, 13030–13036.
- (65) Pyun, J.; Jia, S.; Kowalewski, T.; Patterson, G. D.; Matyjaszewski, K. *Macromolecules* 2003, 36 (14), 5094–5104.
- (66) Jakubowski, W.; Matyjaszewski, K. *Macromolecules* 2005, 38 (10), 4139–4146.

- (67) Pasetto, P.; Blas, H.; Audouin, F.; Boissière, C.; Sanchez, C.; Save, M.; Charleux, B. *Macromolecules* 2009, *42* (16), 5983–5995.
- (68) Natarajan, B.; Lachman, N.; Lam, T.; Jacobs, D.; Long, C.; Zhao, M.; Wardle, B. L.; Sharma, R.; Liddle, J. A. *ACS Nano* 2015, *9* (6), 6050–6058.
- (69) Ryan, A. J. *Nat. Mater.* 2002, *1* (1), 8–10.
- (70) Kietzke, T.; Neher, D.; Landfester, K.; Montenegro, R.; Güntner, R.; Scherf, U. *Nat. Mater.* 2003, *2* (6), 408–412.
- (71) Koerner, H.; Kelley, J.; George, J.; Drummy, L.; Mirau, P.; Bell, N. S.; Hsu, J. W. P.; Vaia, R. a. *Macromolecules* 2009, *42* (22), 8933–8942.
- (72) Chevigny, C.; Jouault, N.; Dalmas, F.; Boué, F.; Jestin, J. *J. Polym. Sci. Part B Polym. Phys.* 2011, *49* (11), 781–791.
- (73) Green, P. F. *Soft Matter* 2011, *7* (18), 7914–7926.
- (74) Corbierre, M. K.; Cameron, N. S.; Sutton, M.; Laaziri, K.; Lennox, R. B. *Langmuir* 2005, *21* (13), 6063–6072.
- (75) Chevigny, C.; Jestin, J.; Gignes, D.; Schweins, R.; Di-Cola, E.; Dalmas, F.; Bertin, D.; Boué, F. *Macromolecules* 2010, *43* (11), 4833–4837.
- (76) Chevigny, C.; Dalmas, F.; Di Cola, E.; Gignes, D.; Bertin, D.; Boué, F.; Jestin, J. *Macromolecules* 2011, *44* (1), 122–133.
- (77) Frisken, B. J. *Appl. Opt.* 2001, *40* (24), 4087–4091.
- (78) Bauer, B. J.; Briber, R. M.; Han, C. C. *Macromolecules* 1989, *22* (2), 940–948.
- (79) Faust, A. B.; Sremcich, P. S.; Gilmer, J. W.; Mays, J. W. *Macromolecules* 1989, *22* (3), 1250–1254.
- (80) Russell, T. P.; Fetters, L. J.; Clark, J. C.; Bauer, B. J.; Han, C. C. *Macromolecules* 1990, *23* (2), 654–659.
- (81) Merkel, T. C.; Freeman, B. D.; Spontak, R. J.; He, Z.; Pinnau, I.; Meakin, P.; Hill, A. J. *Science* 2002, *296* (5567), 519–522.
- (82) Fernandes, N. J.; Akbarzadeh, J.; Peterlik, H.; Giannelis, E. P. *ACS Nano* 2013, *7* (2), 1265–1271.

- (83) Vogiatzis, G. G.; Theodorou, D. N. *Macromolecules* 2013, 46 (11), 4670–4683.
- (84) Trombly, D. M.; Ganesan, V. *J. Chem. Phys.* 2010, 133 (15), 154904.
- (85) Maillard, D.; Kumar, S. K.; Rungta, A.; Benicewicz, B. C.; Prud'homme, R. E. *Nano Lett.* 2011, 11 (11), 4569–4573.
- (86) Ojha, S.; Dang, A.; Hui, C. M.; Mahoney, C.; Matyjaszewski, K.; Bockstaller, M. R. *Langmuir* 2013, 29 (28), 8989–8996.
- (87) Hore, M. J. a.; Ford, J.; Ohno, K.; Composto, R. J.; Hammouda, B. *Macromolecules* 2013, 46 (23), 9341–9348.
- (88) Percus, J. K.; Yevick, G. J. *Phys. Rev.* 1958, 110 (1), 1–13.
- (89) Feigin, L. A.; Svergun, D. I. *Structure Analysis by Small-Angle X-Ray and Neutron Scattering*; Taylor, G. W., Ed.; Springer US: Boston, MA, 1987; Vol. 12, pp 654–660.
- (90) Hammouda, B. *Adv. Polym. Sci.* 1993, 106, 87–133.
- (91) Bale, H. D.; Schmidt, P. W. *Phys. Rev. Lett.* 1984, 53 (6), 596–599.
- (92) Teixeira, J. *J. Appl. Crystallogr.* 1988, 21 (6), 781–785.
- (93) Sun, S.-T.; Nishio, I.; Swislow, G.; Tanaka, T. *J. Chem. Phys.* 1980, 73 (12), 5971–5975.
- (94) Stuart, M. A. C.; Huck, W. T. S.; Genzer, J.; Müller, M.; Ober, C.; Stamm, M.; Sukhorukov, G. B.; Szleifer, I.; Tsukruk, V. V.; Urban, M.; Winnik, F.; Zauscher, S.; Luzinov, I.; Minko, S. *Nat. Mater.* 2010, 9 (2), 101–113.
- (95) Ward, M. a.; Georgiou, T. K. *Polymers (Basel)*. 2011, 3 (4), 1215–1242.
- (96) Huggins, M. L. *J. Am. Chem. Soc.* 1942, 64 (7), 1712–1719.
- (97) Flory, P. J. *J. Chem. Phys.* 1945, 13 (11), 453.
- (98) Swislow, G.; Sun, S.-T.; Nishio, I.; Tanaka, T. *Phys. Rev. Lett.* 1980, 44 (12), 796–798.
- (99) Adam, M.; Fetters, L. J.; Graessley, W. W.; Witten, T. A. *Macromolecules* 1991, 24 (9), 2434–2440.

- (100) Jansen, J. .; de Kruif, C. .; Vrij, A. *J. Colloid Interface Sci.* 1986, 114 (2), 471–480.
- (101) Levicky, R.; Koneripalli, N.; Tirrell, M.; Satija, S. K. *Macromolecules* 1998, 31 (11), 3731–3734.
- (102) Roke, S.; Buitenhuis, J.; Miltenburg, J. C. Van; Bonn, M.; Blaaderen, A. *Van. J. Phys. Condens. Matter* 2005, 17 (45), S3469–S3479.
- (103) Bauer, B. J.; Fetters, L. J.; Graessley, W. W.; Hadjichristidis, N.; Quack, G. F. *Macromolecules* 1989, 22 (5), 2337–2347.
- (104) Egorov, S. A.; Binder, K.; Physik, I.; Gutenberg, J.; Mainz, U.; Weg, S.; Mainz, D.-. *J. Chem. Phys.* 2012, 094901 (137), 1–9.
- (105) Lo Verso, F.; Yelash, L.; Egorov, S. a.; Binder, K. *Soft Matter* 2012, 8 (15), 4185.
- (106) Ganazzoli, F.; Fontelos, M. A.; Allegra, G. *Polymer (Guildf)*. 1991, 32 (1), 170–180.
- (107) Grest, G. S. *Macromolecules* 1994, 27 (13), 3493–3500.
- (108) Kaiser, A.; Schmidt, A. M. *J. Phys. Chem. B* 2008, 112 (7), 1894–1898.
- (109) Seelenmeyer, S.; Deike, I.; Rosenfeldt, S.; Norhausen, C.; Dingenouts, N.; Ballauff, M.; Narayanan, T.; Lindner, P. *J. Chem. Phys.* 2001, 114 (23), 10471–10478.
- (110) Zackrisson, M.; Stradner, A.; Schurtenberger, P.; Bergenholtz, J. *Langmuir* 2005, 21 (23), 10835–10845.
- (111) Benhamou, M.; Himmi, M.; Benzouine, F. *J. Chem. Phys.* 2003, 118 (10), 4759.
- (112) Slagowski, E.; Tsai, B.; McIntyre, D. *Macromolecules* 1976, 9 (4), 687–688.
- (113) Nierlich, M.; Cotton, J. P.; Farnoux, B. *J. Chem. Phys.* 1978, 69 (4), 1379–1383.
- (114) Guinier, A.; Fournet, G. *J. Polym. Sci.* 1955, 1, 268.
- (115) Kline, S. R. *J. Appl. Crystallogr.* 2006, 39 (6), 895–900.
- (116) Dingenouts, N.; Norhausen, C.; Ballauff, M. *Macromolecules* 1998, 31 (25), 8912–8917.

- (117) Stieger, M.; Pedersen, J. S.; Lindner, P.; Richtering, W. *Langmuir* 2004, 20 (17), 7283–7292.
- (118) Alessandrini, J. L.; Carignano, M. A. *Macromolecules* 1992, 25 (3), 1157–1163.
- (119) Williams, C.; Brochard, F.; Frisch, H. L. *Annu. Rev. Phys. Chem.* 1981, 32 (1), 433–451.
- (120) Hammouda, B. *PROBING NANOSCALE STRUCTURES–THE SANS TOOLBOX*; 2010; p 224.
- (121) Akcora, P.; Kumar, S. K.; Moll, J.; Lewis, S.; Schadler, L. S.; Li, Y.; Benicewicz, B. C.; Sandy, A.; Narayanan, S.; Ilavsky, J.; Thiyagarajan, P.; Colby, R. H.; Douglas, J. F. *Macromolecules* 2010, 43 (2), 1003–1010.
- (122) Schneider, G. J.; Nusser, K.; Willner, L.; Falus, P.; Richter, D. *Macromolecules* 2011, 44 (15), 5857–5860.